/
Article / Book Information

( )	60GHz
Title(English)	Study of 60 GHz Millimeter Wave Radio Propagation for Future Heterogeneous Wireless Networks
( )	
Author(English)	Karma Wangchuk
( )	: ( ), : , : 10491 , :2017 3 26 , : , : , , , ,
Citation(English)	Degree:Doctor (Engineering), Conferring organization: Tokyo Institute of Technology, Report number: 10491 , Conferred date:2017/3/26, Degree Type:Course doctor, Examiner:,,,,
( )	
Type(English)	Doctoral Thesis

Study of 60 GHz Millimeter Wave Radio Propagation Channel for Future Heterogeneous Wireless Networks

by

Karma Wangchuk

Submitted to the Department of International Development Engineering
in partial fulfillment of the requirements for the degree of

Doctor of Engineering

at the

TOKYO INSTITUTE OF TECHNOLOGY

March 2017

Author . . . .
Department of International Development Engineering
Feburary 24, 2017

Thesis Supervisor . . . .
Jun-ichi TAKADA
Professor

Study of 60 GHz Millimeter Wave Radio Propagation Channel for Future Heterogeneous Wireless Networks

by

Karma Wangchuk

Submitted to the Department of International Development Engineering
on Feburary 24, 2017, in partial fulfillment of the
requirements for the degree of
Doctor of Engineering

Abstract

To use millimeter wave bands in future heterogeneous wireless networks, understanding the directional properties of the propagation channel in different environment and polarization is very important. This thesis presents result and discussions from analysis of wide-band full polarimetric double directional channel measurement at the millimeter wave band in a typical urban pico-cell environment, both indoor and outdoor. To gain further insights into the properties of the channel, the scattering objects and the propagation mechanisms that give rise to the multipath clusters are identified and analyzed. In terms of the propagation mechanisms, specular reflection is found to be dominate under line-of-sight conditions in the outdoor environment. However in indoor environment and under non line-of-sight conditions scattering and diffraction, respectively, are found to be equally significant. The angular dispersion in urban outdoor pico-cell environment is found to be higher on the mobile station side compared to dispersion on the base station side, but it does not show any dependence on polarization. The scattering intensities are however found to be sensitive to polarization. The vertical polarization clusters are generally stronger than other clusters. The results and discussion provided in this thesis will be useful for designing millimeter wave systems, antennas and algorithms.

Thesis Supervisor: Jun-ichi TAKADA
Title: Professor

Acknowledgments

In working towards this dissertation I have felt the full gamut of human emotions, but mostly it has been one of joy and fulfillment. Over the last several years, I have grown both academically and individually. This I owe to the numerous individuals who have helped me on this journey. The few words below would not suffice to describe the gratitude I feel.

Above all, I have to thank my adviser Professor Jun-ichi Takada, for the farsighted guidance and unwavering support. In particular, I appreciate him for giving me the space and time for my own ideas to grow. I also have to thank Associate Professor Minseok Kim, at Niigata University, for his advice and for hosting me during the several measurement campaigns carried out as part of this dissertation. A special mention has to go to Mr. Kento Umeki and Mr. Tatsuki Iwate, of Kim laboratory, for helping out during the measurements; day and night. I also owe a lot of gratitude to Assistant Professor Kentaro Saito, and Dr. Azril Haniz for all the valuable discussions and encouragements. In no small measure I would like to express my appreciation to all the members of the Takada Laboratory for being a friend, a mentor, and a source of inspiration.

This journey would not have been possible without the Monbukagakkusho (MEXT) scholarship received from the Japanese government and for that I am indebted to the generosity of the Japanese people.

And finally, to my parents and my sisters, for giving me the strength and never letting me forget my roots, I thank you.

Contents

List of Figures

List of Tables

1 Introduction

1.1 Background

Data consumption and demand for higher data rate has exploded in recent years. It is fulled by the success of smart mobile devices and availability of digital contents on the internet. This cycle of demanding higher data rates to consume the more bandwidth intensive contents (especially multimedia contents such as HD and 4K videos) and creation of these contents because of the high speed data capacity of the network and user devices, has driven the growth of the mobile industry in the past decade. Data traffic still continues to grow exponentially, 60% in 2015, with video accounting for $40-50\%$ of the total traffic [5]. Due to the popularity of video sharing on social media and live streaming services, this traffic is forested to grow by 55% annually though 2021. However not all devices that will connect to the network will impose the same demands as above. However not all devices that will connect to the network will impose the same demands as above. Instead, for instance internet of things (IoT) devices and medical devices would have a completely different set of requirements, such as very low latency and very low energy consumption. This poses a very interesting challenge and is being actively researched with the end goal of moving towards 5G [6].

To meet the demands for higher data rate, there is a general consensus among the researchers that the next generation of cellular and wireless system will have to employ significantly large signal bandwidth, which are available abundantly in the millimeter wave region. The spectrum congestion in the microwave bands have made escalation of the carrier frequencies beyond the current sub 6 GHz frequencies in-

evitable [7] [8]. The ITU-R selected candidate frequency bands in between 24.25 GHz and 86 GHz, more commonly known as the millimeter wave bands have recently gained considerable attention. In particular the 28 GHz, 38 GHz, the 60 GHz unlicensed band (59-66 GHz), and the 73 GHz (71-76 GHz E-band) frequencies have been studied as a possible candidate carrier frequencies for 5G. The unlicensed 60 GHz band however has also been extensively studied for use in indoor environment leading towards the IEEE 802.15.3c 60 GHz Wireless Personal Area Network (WPAN) standard (published in 2009), and the WirelessHD and Wireless Gigabit Alliance (WiGig) IEEE 802.11ad multi-gigabit per second Wireless Local Area Network(WLAN) standard (announced in 2009). In the past the millimeter wave spectrum was mainly used for satellite communications, military applications, long-range point-to-point communications and Local Multipoint Distribution Services (LDMS)[9][10].

Till recently, the millimeter wave band was thought to be not suitable, especially in outdoor environment, due to large atmospheric attenuation[11], large attenuation due to common building materials [12][13] and also the challenges in designing antenna and the integrated circuits [11]. These issues are being vigorously addressed by the research community in recent years and deployment of millimeter wave in heterogeneous network configuration (with many millimeter wave pico cells within an overlaying macro cell operating at the traditional microwave frequency) is viewed as a key enabler for the fifth generation of mobile networks, 5G [14][15]. In this thesis we focus mainly on the unlicensed 60 GHz millimeter wave band due to its potential use in both the indoor (WLAN) and outdoor (mobile) wireless networks.

1.2   Related works and Research motivation

There are a large amount of existing millimeter wave radio propagation works focusing mainly on the unlicensed 60 GHz band and in indoor environment. These works were carried out as contributions to or were motivated by the IEEE 802.15.3c and the IEEE 802.11ad standards. Only recently has the research community and the industry earnestly started to investigate the millimeter wave bands for mobile wireless

networks and for outdoor environment. This section provides a brief survey of the measurement based millimeter wave propagation studies in both the outdoor and indoor environment. More emphasis is placed on the outdoor case since there are only limited number of works. From the survey the gaps in the existing works are identified and the motivation of the work carried out towards this thesis is outlined.

1.2.1 Existing works in outdoor environment

The major recent contributions to millimeter wave propagation studies in urban outdoor environment, covering 28 GHz, 30 GHz, 60 GHz and the 73 GHz bands are from the Rappaport *et al.* An overview of the groups work appears in [16], [17] and [18].

The 28 GHz measurement carried out in New York city is reported in [19][20][21][22]. For measurement a sliding cor-relator sounder with 400 megachip-per-second with maximum output power of 30 dBm is used. The measurement is not fully double directional. On the transmitter (Tx) side the channel is measured at three antenna angular positions $(-5°, 0°, +5°)$. On the receiver (Rx) side the channel is measure for full azimuth scan at three different elevation angles. Polarization is not considered. A large number of line of sight (LOS) and non line of sight (NLOS) locations, in total 75 locations over a distance of 500 m, are considered. A path loss exponent (PLE) of 5.73, a maximum LOS excess delay of 753.5 ns and NLOS excess delay of 1388.4 ns is reported. Mean root mean square (RMS) delays spread of 17.4 ns when using narrow-beam antennas, and mean RMS delay spreads of 15.6 ns when using wider beam antenna is reported for the same set of measurement in [17].

In [23][18], a 28 GHz measurement campaign in Korean is reported. The channel is measured at 250 MHz bandwidth with 24.5 dBi (10° HPBW) antennas for 11 Rx locations and 1 Tx locations at distances of over 200 m. The calculated path loss exponent (PLE) is 3.53 under NLOS condition. An average angle of departure (AoD) and angle of arrival (AoA) RMS spread of 5.12° and 25.16°are reported. The RMS delay spread of <100ns is observed. This measurement is fully double directional but polarization is not considered.

The 28 GHz measurements at the Alborg university is presented in [24]. The

measurements carried out for contributing toward the METIS channel model [25]. In this measurement the Tx antenna height is varied between 15 m to 25 m. The Tx antenna is a 10 dBi 55° HPBW antenna and the Rx antenna is a bi-conical antenna with 18° HPBW in elevation. Dynamic measurements is carried out by placing the Rx in a van and driving between distances of 50.7 m to 876.7 m. This measurement is geared towards studying the dynamic nature of the channel and not the directional or polarimetric properties. By changing the antenna height from 15 m to 25 m a path loss exponent change from 2.5 to 1.9 is reported.

In [26][27][28] the measurements conducted at 38 GHz, with a 400 Mcps chanel sounder, at the university of Texas is reported. Measurements are made with two identical Ka-band vertically polarized horn antennas with 7° HPBW and 25dBi gain. Results for access link measurements at distances ranging from 61 m to 265 m are reported. An average RMS delay spread of 12.2 ns and maximum RMS delay spread of 117 ns is reported or NLOS and. Virtually no RMS delay spread for all LOS links were observed. A PLE of 4.57 when considering all the links and of 3.71 when considering only the best links under NLOS condition is reported. It is also noted that the LOS PLE is identical to the free space. Here also double directional and polarimetric measurements are not carried out.

In [29] the scattering from rough surfaces, a cement block which is a common construction material, at 28 GHz and 38 GHz are measured. It is shown that scattering depends strongly on polarization, incident angle and the surface geometry. The horizontal polarization are seen to be more sensitive to surface roughness.

In [30] the measurements at 73 GHz of the E-Band for outdoor mobile and backhaul links are carried out at New York University, for distances between 30 m to 200 m. A total of 74 Rx-Tx combinations were measured using 27dBi 7° HPBW antennas. Directional measurements on the Rx side for the Tx angular locations that resulted in strongest received power at RX were measured. No polarization is considered. From these measurement, under LOS condition a PLE of 2.57 and under NLOS an overall PLE of 5.96 is reported. The maximum excess delay (for paths below 20 dB of the first arrival path) is determined to be 91.3 ns, and the RMS delay spread of 20.3 ns is

seen under NLOS condition.

E-band propagation measurements at 73.5 GHz [31] in an urban street canyon environment were also carried out at downtown Helsinki with 24dBi 15° HPBW on the Tx side and a parabolic 43 dBi 0.8° HPBW antenna on the Rx side. The channels were measured at distances of 130 m , 400 m and 800 m. At each Rx locations, after locating the direction of the maximum receive power level , the Rx antennas were scanned in 1° steps in both elevation and azimuth. This indicates a directional measurement only on the Rx side. For the three different distances azimuth angular spread of up-to 1.45° and elevation spread values of up-to 2.5° are reported. Similar measurement at 80-86 GHz with 5 GHz channel sounding bandwidth is reported by the same group in [32]. Measurements were carried out in a street canyon environment, also in downtown Helsinki, at distances of 685and 1100 m. Analysis of the delay dispersion showed mean RMS delay spread of 0.10 ns at 685 m and 0.125 ns at 1100 m.

Some of the outdoor measurement based works available in 60 GHz bands are from 1980's to 1990's, such as in [33][34][35][36]. In [33] measurements carried out at 59 GHz in 7 different streets of downtown Oslo, under LOS condition, are reported. The Tx was connected to an antenna with 90° HPBW in azimuth and 20° HPBW in elevation. On the Rx side a bi-conical antenna with 20° HPBW in elevation was used. With a system bandwidth of 200 MHz it is determined that the mean delay spread in most situation is less than 20 ns and for 90% delay window the spread is less than 50 ns. Similar results are obtained in [34]. In [35] propagation measurements at 55 GHz between fixed Tx and mobile Rx in urban environment for 66 MHz bandwidth and for distances of up to 400 m is described. The path loss along the directly illuminated street has a path loss exponent of 3.6 and approximately a path loss exponent of 10 while behind the base station. The coherence bandwidth is found to vary in the range 20-150 MHz. The small scale fading envelope measured in urban micro-cell is found to vary similarly to 900 MHz with average location variability of 3.2dB and loss deviation of 4.7 dB.

In [36] measurements on point-to-point transmission at street level were performed in downtown Denver at 57.6 GHz. A Tx antenna with 10° HPBW and a receive

antenna with 28.8° HPBW were used. The setup was used to measure the reflection or scattering from various different surfaces. Continuous wave signal probes were used to measure signal loss on paths obstructed by buildings, with several common materials. It showed attenuation in excess of 100 dB. Dependence of the millimeter wave propagation on the antenna polarization was also examined and no dependence for grazing angles as small as 8 degrees were found.

More recent measurement based studies in urban environment at the 60 GHz bands are found in [28][26][37]. These studies are based on the same measurement data set. In these studies the 60 GHz band is measured for Peer-to-Peer scenario (P2P) (for 18.5 m distance) or for vehicular scenario (for 4.12 m,and 23 m distances). In both the scenarios the directional measurement is only on the Rx side, however for the vehicular scenario the Rx is positioned inside a car. For the P2P measurement and LOS condition, a PLE of 2.23 was determined. For all the NLOS paths a PLE of 4.19 was obtained with the NLOS paths excess gain in the range of -15 to -40 dB. For P2P the LOS delay spread was very small (<0.9ns) and the NLOS delay spread varied greatly with mean of 7.39 ns to maximum of 36.6 ns. For the vehicular scenario under LOS condition a PLE of 2.66 and for NLOS condition a PLE of 7.17 (due to shielding of the car) is reported. The delay spread values determined for vehicular scenario were 0.9 ns for LOS and up to 12.3 ns for NLOS case. No polarization dependence study or polarimetric measurements were conducted.

A cellular millimeter wave access link measurements at 60 GHz are carried out in a busy urban street canyon environment in [38]. Further analysis, augmented with ray tracing results, for the measurement campaign appears in [39]. Vertically polarized omnidirectional antennas (in azimuth) are used on both the Tx and the Rx. There is no directional measurement in this study. By moving the Rx 50 m on either side of the Tx, at 0.5ms dynamic channel impulse responses are recorded. The whole measurement is in LOS condition. Analyzing the measured data, a PLE of 2.13 which is slightly higher than the free space is determined. A delay spread equal to 63.47 ns is determined, and it is also shown that this spread values are predicted using a ray tracing simulation in [39]. Here also polarization and directional properties are not

addressed.

Table 1.1: Summary of double directional measurement and polarization considerations in milimeter wave outdoor literature

Ref.	Freq. (GHz)	Environment	Scenario (link)	Double dir.	Polarization
[8 − 9]	28	Dense urban	Access, Backhaul	Rx side	NA
[10, 15]	28	Dense urban	Access , Backhaul	Yes	NA
[16]	28	Street canyon	Access	NA	NA
[17 − 19]	38	Dense urban	Access , P2P	Rx side	V-V
[21]	73	Dense urban	Access , Backhaul	Rx side	NA
[22, 23]	73.5, 83	Street canyon	Access , P2P	Rx side	NA
[24 − 26]	60	Urban street	P2P	NA	NA
[27]	57.6	Urban street	p2p	NA	Full
[17, 19, 28]	60	Dense urban	P2P, Vehicular	Rx side	NA
[29 − 30]	60	Street canyon	Access	NA	V-V

Table 1.1 gives the summary of the surveyed works. We see that in most of the measurement campaigns the directional measurement is only on one side (usually the Rx side) or no directional measurements are carried out. Also almost non of the measurements treat polarization even though it is shown in [29] that the millimeter wave propagation is strongly influenced by polarization. What is clear is that most of the measurements are aimed at determining the large scale parameters such as the path loss, path loss exponent and the overall RMS delay spreads. The focus of most of the works is statistical modeling of large scale channel parameters by carrying out large number of measurements. Statistical models are of immediate interest to the industry. However if we want to understand the physical mechanisms and to analyze the phenomenons in detail, full polarimetric double directional measurements and subsequent analysis is necessary. Even the statistical models is incomplete and therefore less accurate without the full polarimetric double directional information. Therefore full polarimetric double directional measurement and study are important to fill this gap in the outdoor millimeter wave propagation study.

1.2.2 Existing works in indoor environment

In case of the indoor environment, the 60 GHz band has been considered for application in WPAN (IEEE 802.15.3c), WirelessHD, and WiGig IEEE 802.11.ad WLAN for a long time and therefore a huge volume of work exists. On the contrary indoor measurement for other millimeter wave bands are being considered only recently and therefore only a few materials are available.

To list down and review all the works on measurement based study of 60 GHz indoor propagation channel is not practical and also counter productive, due to the sheer volume of works. For works before 2008 a very good survey appears in [40]. Although some part of the paper is focused towards statistical modeling of the indoor millimeter wave channel, a bulk of the paper is dedicated to reviewing results reported in the literature. In terms of the measurement environment, various indoor environment such as conference room, corridor, office, hall way, laboratory, residential rooms are considered for measurement. One of the limitations of comparing the various measurement is the influence of the antenna used to carry out the measurement. In most cases, among the works reviewed in [40], the path-loss or the delay spread values are dependent on the antenna used since the antenna is not de-embedded from the measurement. For various HPBW antennas used on the Tx side(ranging from narrow 9.1° to omnidirectional) and the Rx side(7° to omnidirectional), the path loss exponent values are listed in Table I of [40]. The PLE ranges from 0.56 (for office environment under LOS condition and for 72° HPBW Rx antenna and 60° HPBW Tx antenna) to PLE of 3.74 (for an office environment under NLOS condition measured with Tx and Rx antennas each of 30° HPBW antenna). In the paper the author notes that the RMS delay spread reported in literature are highly dependent on the HPBW of the antenna used and can be even reduces to as low as 1 ns when using pencil beam antennas. The delay spread values are also noted to be dependent upon the room size with delay spreads of 15 ns for small sized offices ($8\,m^2$ and $12\,m^2$) (reference [41]) and between 15 ns to 45 ns for larger office rooms ($85\,m^2$ to $105\,m^2$ (reference [42] [43]). Under the WPAN channel model, which is an extended S-V

model, extended as per [44] and [45] only the angle of arrival (AoA) is considered. Therefore the bulk of the measurements reviewed in [40] are only directional on the MS side. In [45], the cluster parameters for a residential environment and under-LOS conditions are reported at 49.2° , 119° , 46.2° , and 107° for a Tx HPBW of 360° ,60° ,30° , and 15° , respectively, and Rx HPBW of 15° . Under LOS conditions and for office environment, values are 102° and 66.4° for a HPBW of 30° at both ends and 60° at both ends, respectively. For the office environment with NLOS, 60.2° and 22.2° is found for Tx-HPBW of 360° and 30° , respectively, in combination with an Rx of 15° HPBW. These are in fact very large compared to the intra-cluster parameters we have measured, however these are not measured parameters, rather these are the modeled parameters assuming the spread to be a Laplacian distribution. Here also only the azimuth angles are considered. Polarizations are not discussed.

From here on we will only look at few of the major contributions after 2008. Maltsev *et al.* in [46] employed an OFDM channel sounder at 60 GHz with bandwidth of approximately 800 MHz and steerable horn antenna with 18 dBi 20° HPBW. Measurements were conducted in a conference room and an office with cubicles. In the conference room the Tx and Rx antennas were located at the same height. For office environment measurement, the Tx and Rx elevation angles are fixed and the azimuth angles of the two antennas were scanned and the channel measured. From the measurement it is concluded that the 60 GHz propagation channel is quasi-optical in nature and the main power contributions were from the Line Of Sight (LOS) and reflected signal paths of the first and second orders. The highly directional nature of the channel is confirmed. Inter-cluster arrival azimuth spread and elevation spreads for conference room is determined to be 9° to 10°. The first order and second order reflection clusters are determined to have an excess gain of -10 dB and -16 dB respectively. This work together with [47] and [48] form the core contributions of the WiGig IEEE 802.11ad WLAN channel model.

Haneda *et al.* has conducted a lot of measurement campaigns at the 60 GHz and 70 GHz bands in indoor shopping malls, railway stations, and office environments using a vector network analyzer (VNA) based channel sounder. The sound system

has over 5 GHz of bandwidth [49][50][51]. Directional measurements are carried out only on the Tx side and only on the azimuth plane, with a 20 dBi directional horn antenna. On the Rx side a bi-conical omnidirectional antenna is used. For a shopping mall a mean delay spread of 5.2 ns under LOS and 16.6 ns under NLOS condition is reported [52]. Similarly the average LOS AoA side azimuth spread was 12° and and for obstructed LOS (OLOS) it was 40.7°. The AoD average azimuth spread was 15.5° and 41.9° for LOS and OLOS respectively.

The work in [53] provides details of the wide-band millimeter wave propagation measurement carried out in an indoor office environment at 28 GHz and 73 Ghz by a 400 MHz channel sounding system. A total of 48 Tx-Rx location combinations were measured. In both the frequencies the Tx antennas were placed at 2.5 m above the floor and the Rx antennas were located at 1.5 m. A partial polarimetric measurement using V-V and V-H polarizations were carried out. The channel was not measured for H-H and H-V polarizations. Identical pyramidal horn antennas were employed in each frequencies. For 28 GHz a 15dBi 30° HPBW antenna and for 60 GHz a 20 dBi 15° HPBW antenna were used. Directional measurements at either the Tx side or the Rx side are conducted, but full double directional measurement are not carried out. Similar to other outdoor works from the group the path loss model and the path loss exponents were determined for individual frequency and a multi-frequency. The modeling is done separately for the two polarizations considered. Using either the directional measurement or using the synthesized omnidirectional measurements the path loss exponents are again separately obtained. A combined polarization omnidirectional PLE of 2.1 for LOS environment and 3.4 for NLOS environment is found. For 28 GHz and LOS condition mean RMS delay spread from 4.1 ns to 17.3ns for VV, and 7.3 ns to 17.2 ns for VH is reported. For NLOS at 28 GHz mean RMS delay spread of 13.4 ns to 17.7 ns for V-V and 13.2 ns to 18.0 ns for V-H is reported. similarly for 73 GHz and LOS condition mean RMS delay spread of 3.6 ns to 12.8 ns for V-V and 7.0 ns to 11.4 ns for V-H is reported. For NLOS at 73 GHz mean RMS delay spread of 11.3 ns to 12.3 ns for V-V and 8.4 ns to 12.5 ns for V-H is reported. The works reviewed above are just few of the major contributions. Therefore this

is just a representative sample covering those millimeter wave bands where measurements have been reported. From the summary in Table 1.2, similar to the case of

Table 1.2: Summary of double directional measurement and polarization considerations in millimeter wave indoor literature

Ref.	Freq. (GHz)	Environment	Scenario(link)	Double dir.	Polarization
[31 − 36]	28, 73	Office, Residential, Conference hall, laboratory, corridor	Access	Rx side	V-V, V-H
[37 − 39]	60	Conference hall, Office	Access	Yes	No
[40 − 43]	60	Shopping mall, Station, Office	Access	No	No
[44]	60	Office	Access	Rx side	V-V

outdoor measurement campaigns, in indoor case also most of the existing work are focused towards statistically modeling the channels. This means measuring a large number of points and then trying to fit some statistical description to the measurement. Even then, without the double directional and polarimetric measurement the constructed model is incomplete. If we want to analyze and understand more about the underlying mechanisms and phenomenons, the double directional and full polarimetric measurements are indispensable. Understanding that there are these gaps in the existing works, we carry out the double directional full polarimetric measurement campaigns and analyzed the measurements in our work. The results presented in the thesis should help fill the gap.

1.3 Objective and Contributions

The main objective of this study is to investigate the the millimeter wave propagation channel characteristics at the 60 GHz band, under the probable usage scenarios in fu-

ture heterogeneous network [54], in typical outdoor and indoor pico-cell environment. In order to address the lack of studies concentrating on directional and polarization characteristics, this study will focus on the fully polarimetric double directional channel.

To that end, we carry out a fully polarimetric double directional channel measurement using the millimeter wave channel sounder developed [3]. The measurement scenarios are carefully chosen to be similar to the probable usage scenarios in future heterogeneous networks. From the 3-D double directional measurement for a fixed base station (BS) and different mobile station (MS) locations, the dispersion characteristics (delay and angular) of the channel and of the detected clusters (intra-cluster) under LOS and OLOS conditions are determined. The physical scattering objects and the major propagation mechanisms giving rise to the multipath clusters are studied. The main contributions and the novelty of this work are:

- Full polarimetric, double-directional millimeter wave channel measurement in indoor and outdoor urban pico-cell environment and analysis

- Analysis of the propagation mechanisms giving rise to the multi-path clusters in millimeter wave channel

- Analysis of the delay and angular dispersion (both on the MS and BS side) of millimeter wave channel.

- Influence of polarization on the channel characteristics

To the best of our knowledge similar double directional measurement and subsequent analysis presented in this study, especially in the outdoor environment, has not been previously reported in literature.

1.4   Limitations of the Thesis

One of the reasons there are very few measurement based study in the millimeter wave band is the amount of time and resources required to carry out the measurement. The measurement time increases in the order of magnitude when measuring

12

```
┌─────────────────────────────────┐
│      Chapter 1: Introduction      │
└─────────────────────────────────┘
                 │
                 ▼
┌─────────────────────────────────────────────┐
│  Chapter 2: Millimeter Wave Propagation Channel │
└─────────────────────────────────────────────┘
                 │
                 ▼
┌─────────────────────────────────────────────┐
│    Chapter 3: Millimeter Wave Channel Sounding   │
└─────────────────────────────────────────────┘
         │                          │
         ▼                          ▼
┌──────────────────────┐  ┌──────────────────────┐
│ Chapter 4: Mm-wave    │  │ Chapter 5: Mm-wave    │
│ Propagation in        │  │ Propagation in        │
│ Outdoor pico-cell     │  │ Indoor Environment    │
│ environment           │  │                       │
└──────────────────────┘  └──────────────────────┘
         │                          │
         └──────────┬───────────────┘
                    ▼
┌─────────────────────────────────────────────┐
│      Chapter 6: Summary and Conclusion        │
└─────────────────────────────────────────────┘
```
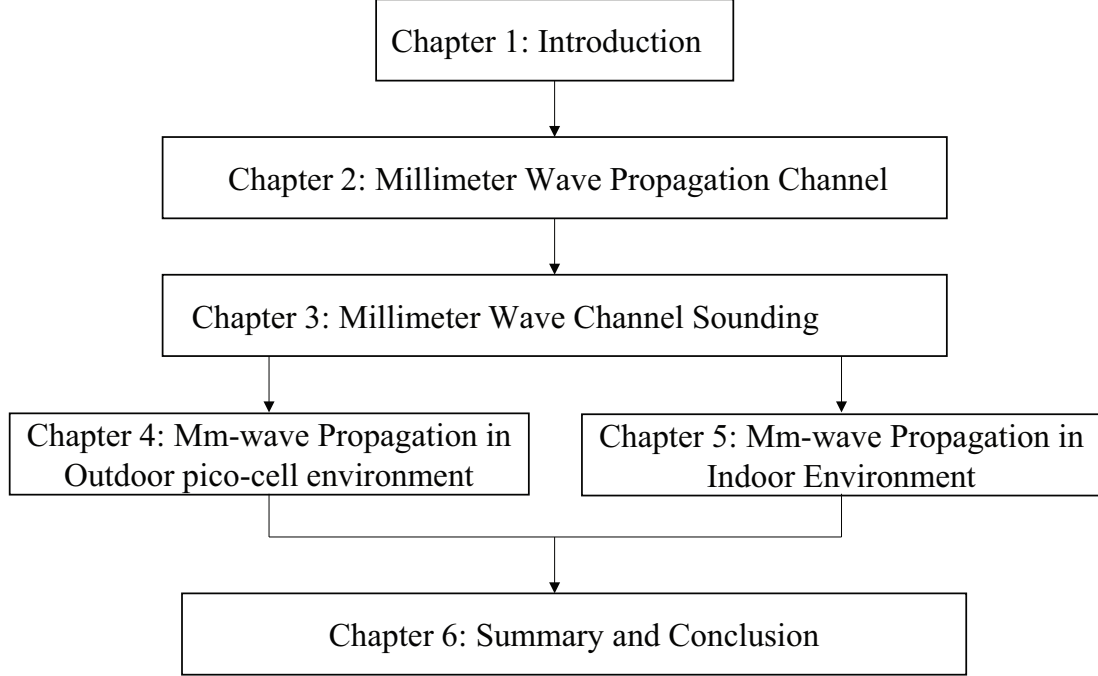
Figure 1-1: Structure of thesis

the double directional channel. It becomes especially challenging when doing measurement in the urban outdoor environment. As a result of this, even in this study the number of measurement is limited and the results are therefore generalized from these measurements.

1.5 Outline of the Thesis

The overall structure of the this is is shown in Figure 1-1. This chapter introduced the background and motivation for the study. The remainder of this thesis is organized as below.

Chapter 2 briefly describes how the millimeter wave is intended to be deployed in future heterogeneous network and the corresponding usage scenarios. The different propagation mechanisms that are relevant to the millimeter wave propagation is discussed. In the later part of the chapter, to fully describe the wideband millimeter wave channel, the double directional channel is introduced. Based on the double directional channel the various condensed channel parameters that can be used to

characterized the the channel are also introduced.

Chapter 3 presents the developed software defined radio based millimeter wave 60 GHz channel sounding system. An overview of the signal design and hardware implementation is provided. In the second part of the chapter the synthesis of the double directional channel from the directional measurements is formulated. Recognizing that the channels are highly directional in nature, clustering of the multipath components and intra-cluster parameters are introduced.

In Chapter 4, the measurement campaign in an outdoor urban pico-cell environment and analysis is presented. The different delay and angular power spectrum functions, synthesized from the measurement, is discussed. From these functions the overall delay and angular dispersion parameters under different polarization configurations are discussed. The clustering of multipath components and the intra cluster delay and angular dispersion parameters are discussed. This chapter also features measurement based ray tracing (MBRT) approach used to identify the major propagation mechanisms by comparing with ray tracing simulation. The cluster characteristics under different polarization for both LOS and O-LOS conditions are determined.

Chapter 5 introduces the indoor measurement campaign. The delay and the angular dispersion characteristics are presented. Similar to the case of the outdoor environment the major propagation mechanisms giving rise to the clusters and the cluster characteristics are under different polarization are determined.

Finally, in Chapter 6, the summary and future direction is presented.

2 Millimeter Wave Propagation Channel

2.1 Introduction

In this chapter we introduce some of the physical mechanisms that govern the propagation of electromagnetic (EM) waves, relevant to millimeter waves propagation. The concept of double directional channel is then discussed for completely describing the wide-band millimeter wave propagation channel. The condensed parameters, that can be derived based on the delay spectrum and angular spectrum functions obtained from the double directional channel impulse response, is introduced to characterize the channel.

Taking into account the limitations posed due to these physical mechanisms we discuss how the millimeter wave band can be deployed for use in cellular and wireless network; we briefly discuss the heterogeneous network and the probable usage scenarios.

2.2 Propagation Mechanisms

Like all EM waves, propagation in millimeter wave bands are subject to basic propagation mechanisms depending on the environment. In absence of any scattering objects in the direction of the propagation, the waves propagate in free space and communication is established under line of sight (LOS) conditions. However in practice, the millimeter wave would be propagating in outdoor or indoor environment filled with conducting and dielectric scatterers. Depending on the type of the scattering object (in some literature this is also called an interacting object and denoted as
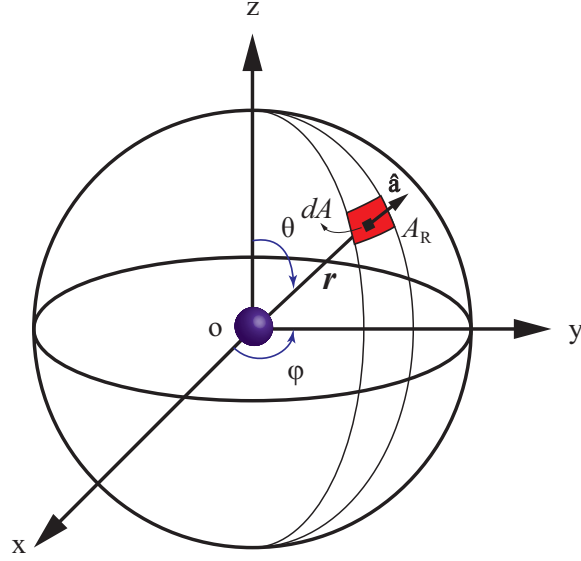
Figure 2-1: Radiation from an isotropic antenna

IO), its material, geometry, location and orientation with respect to the propagation direction, the propagating wave would be subject to different kinds of propagation mechanisms. If the surfaces are smooth the propagating wave will undergo *reflection*. It will be undergo *diffraction* if the surfaces have edges and will undergo *scattering* if the surfaces are rough relative to the wavelength of the propagating wave.

2.2.1 Propagation in Free Space

In absence of any scattering objects the radio waves radiated from an isotropic antenna propagates spherically forming a spherical wavefront with uniform power density at every radial distance from the antenna, such that the integral of the power density over any of these closed spheres equal to the total power radiated. Therefore, the power received by the receiving antenna is equal to the integral of the power density on the spherical wavefront, at radius equal to the LOS distance between the antennas, over the effective area of the antenna surface. An isotropic transmitting antenna located at the origin and a receiving antenna located at $\boldsymbol{r}$, with an aperture area of A_{R} is shown in Fig. 2-1.

$$P_{\mathrm{R}}(r) = \iint_{A_{\mathrm{R}}} \hat{\boldsymbol{r}} \left[\frac{P_{\mathrm{rad}}}{4\pi r^2} \right] \cdot \hat{\boldsymbol{a}} \, dA \qquad (2.1)$$

16

where $P_{\mathrm{rad}} = e_0 P_{\mathrm{in}}$ is the total power radiated by the isotropic transmit antenna, P_{in} is the input power at the feed of the isotropic antenna, $e_0 = e_r e_c e_d$ is the total efficiency of the antenna (where e_r: matching efficiency of the antenna feed, e_c: conduction efficiency and e_d: dielectric efficiency) and $\left(\hat{\boldsymbol{r}} \frac{e_0 P_{\mathrm{rad}}}{4\pi r^2}\right)$ is the power density. Here $\hat{\boldsymbol{a}}$ is the unit normal vector of the receive antenna aperture surface and $\hat{\boldsymbol{r}}$ is radial unit vectors indicating the direction of the radiation power density.

There is a general misconception that the free space propagation loss or what is commonly know as the free space path loss $(P_{\mathrm{rad}} - P_{\mathrm{R}})$ is dependent on the wavelength or the frequency of the propagating wave. However, from (2.1) it is clear that free space path loss doesn't depend on the wavelength. This misunderstanding arises when we define the gain and the type of the antenna at the receiver. Note that in equation (2.1) we only considered the area of the aperture of the antenna, A_{R}. The integral of $(\hat{\mathbf{r}} \cdot \hat{\mathbf{n}} dA)$ in (2.1) gives the effective area of the receiving antenna, $A_{\mathrm{R}}^{\mathrm{eff}}$. For a defined gain $G_{\mathrm{R}}(\theta, \varphi)$ the effective area is given as [55]

$$A_{\mathrm{R}}^{\mathrm{eff}} = \frac{1}{4\pi/\lambda^2} \, G_{\mathrm{R}}. \tag{2.2}$$

Here $\boldsymbol{G}_{\mathrm{R}}(\theta, \varphi) = e_0 \, \boldsymbol{D}_{\mathrm{R}}(\theta, \varphi)$, where $\boldsymbol{D}_{\mathrm{R}}(\theta, \varphi)$ is the directivity of the antenna. It is important to note that, from equation (2.1) we see that for two waves with different wavelengths for the same effective area the free space path loss will be the same, however from equation (2.2) the gain of the antenna will be different for different wavelengths even for the same effective area. In practice it is more convenient to express the equations in terms of the antenna gain rather than the effective area. Therefore for antennas with the same gain the free space path loss will be higher for higher frequencies (or smaller wavelengths). More commonly equation (2.1) is written as

$$P_{\mathrm{R}} = P_{\mathrm{in}} \, \boldsymbol{G}_{\mathrm{T}}(\theta, \varphi) \left(\frac{\lambda}{4\pi \, r}\right)^2 \boldsymbol{G}_{\mathrm{R}}(\theta, \varphi) \tag{2.3}$$

which is indeed the well know *Friss' law* and the term $\left(\frac{\lambda}{4\pi \, r}\right)^n$ is the generalized path loss factor and n the path loss exponent (PLE). For free space the path loss exponent, $n = 2$, as seen above and this loss factor accounts for the losses due to spherical spreading of the energy radiated by the transmit antenna. This exponent

can be used as a rough guide to the nature of the environment; the PLE value is higher for environments with more number of scatterers and equal to 2 when there are no scatterers (free space). The Friss' law is only applicable to far field cases which is determined based on the $Fraunhofer\ distance, d_f$, given as

$$d_f = 2D^2/\lambda \tag{2.4}$$

where D is the largest dimension of the antenna.

If we use large-array antennas on both the transmitter and the receiver side and assume that the array elements are identical, then the power relationship above can be expressed as [56]

$$\begin{aligned} P_{\mathrm{R}} &= P_{\mathrm{in}}\, A_{\mathrm{T}}^{\mathrm{eff}}\, \frac{4\pi}{\lambda^2} \left(\frac{\lambda}{4\pi\, r} \right)^2 \frac{4\pi}{\lambda^2}\, A_{\mathrm{R}}^{\mathrm{eff}} \\ &= P_{\mathrm{in}}\, A_{\mathrm{T}}^{\mathrm{eff}}\, \frac{1}{\lambda^2}\frac{1}{r^2}\, A_{\mathrm{R}}^{\mathrm{eff}}. \end{aligned} \tag{2.5}$$

This shows that if we use array antenna on both the receiver and the transmitter side, ideally with the increase in the frequency the receiver power and hence the free space path loss can be reduced. This is one of the attractions of the millimeter wave band, although there are a lot of practical challenges when deploying very large antenna arrays [57]

In general the free space propagation equation discussed above is applicable for most of the microwave and sub-microwave bands, however in the millimeter wave band attenuation of the propagating electromagnetic wave due to atmospheric absorption, in particular by Oxygen and rain, peaking at 60 GHz (in the millimeter wave band), is quite significant over long distances. This was one of the reasons the millimeter wave band was considered to be not suitable for long distance communication [11]. The specific attenuation due to atmospheric absorption and the total path loss (sum of the free space path loss, atmospheric absorption oxygen and attenuation by light rain) is given in Fig. 2-2 and Fig. 2-3. Although the total path loss is considerably higher, almost 15 dB higher at $200\,\mathrm{m}$ compared to the path loss for $11\,\mathrm{GHz}$, for short distances (less than few hundred meters) the majority of the total path loss is due to the FSPL. The atmospheric and rain attenuation is almost negligible (< 2
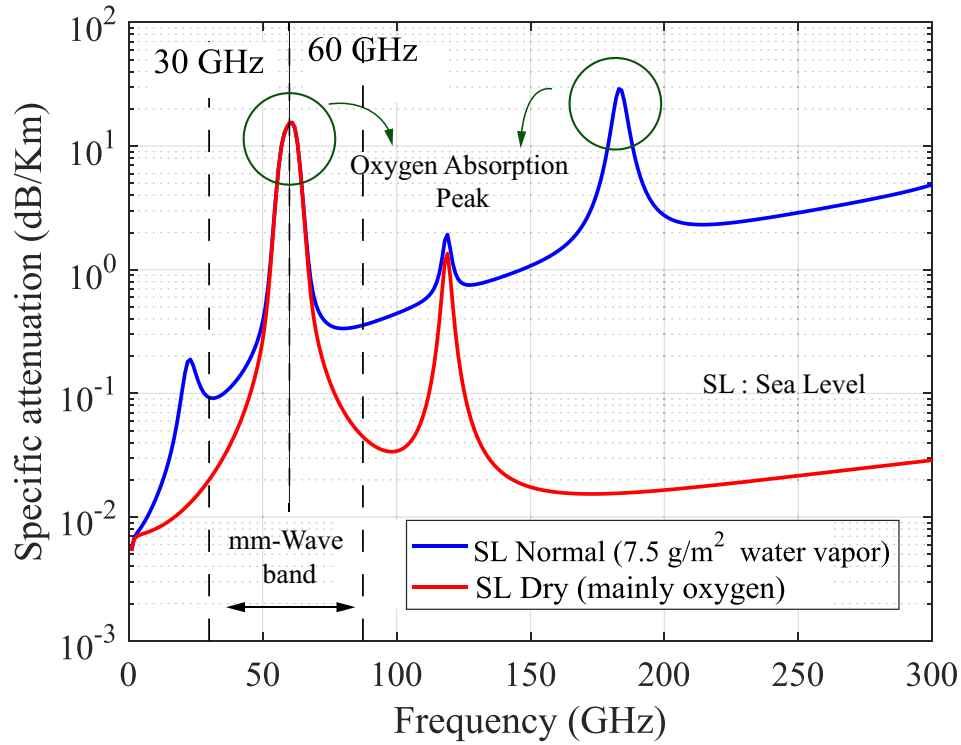
Figure 2-2: Specific attenuation due to Atmospheric absorption (based on ITU-R P.838-3 and ITU-R P.676-5 Recommendations)

dB) when compared to the FSPL. The higher FSPL can be compensated by using higher gain directive antennas or antenna arrays. Therefore over a distance of few hundred meters, such as in a pico cell, the losses due to atmospheric attenuation can be neglected and are not detrimental to deploying the millimeter wave band in outdoor environment.

2.2.2 Reflection and Transmission

In general when we refer to reflection, it usually means the *specular reflection*. It happens when waves are incident on to a surfaces that are smooth and electrically large (large compared to the wavelength of the incident wave). The incident and the reflected waves strictly follow the *Snell's law* which can also be derived from the *Fermet's principle*. Depending on the angle of incidence and the material, one of the consequence of these laws is the transmission in the medium on which the waves

19
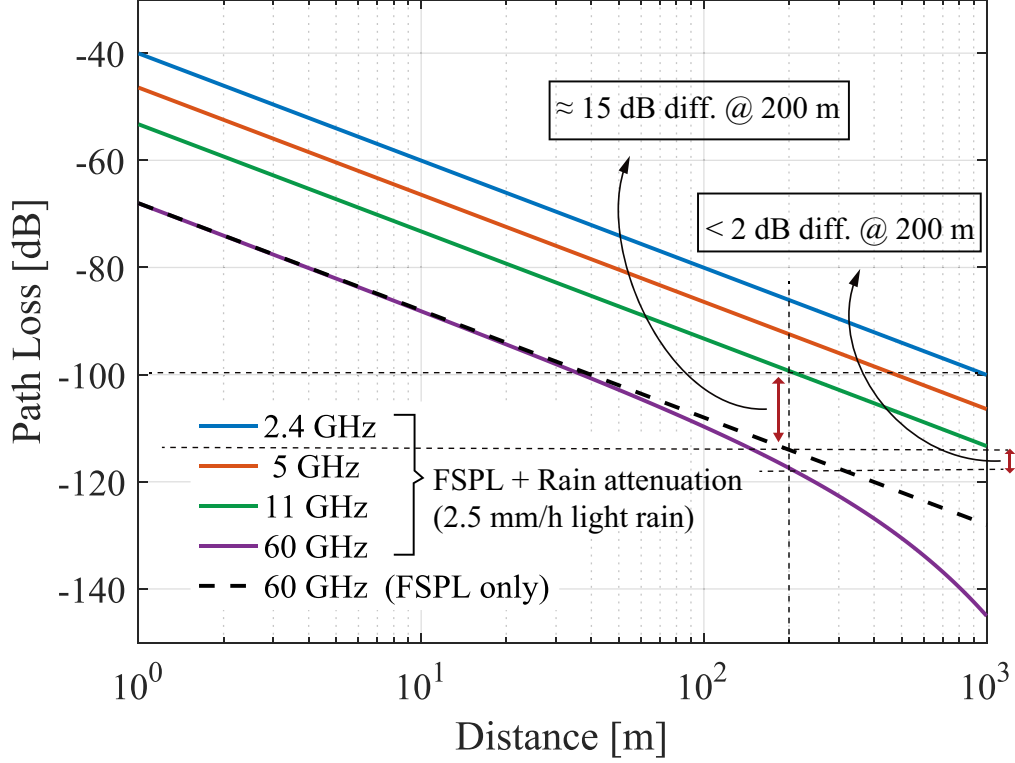
Figure 2-3: Total path loss (FSPL + Atmospheric absorption + Rain attenuation ; based on ITU-R P.838-3 and ITU-R P.676-5 Recommendations)

are incident on. Transmission or penetration through dielectric mediums such as the building walls are mainly responsible for the outdoor - indoor or indoor - outdoor, communication. The coefficients that characterize these two mechanisms are dependent on the material, the incident angle and polarization of the incident wave, and is known as the Fresnel coefficients. The case of two linear polarizations, parallel polarization (the electric field is parallel with respect to the propagation plane) and perpendicular polarization (the electric field is perpendicular with respect to the propagation plane), are shown in Figure 2-4 (Left) and in Figure 2-4 (Right) respectively. The well known Fresnel coefficients for the perpendicular polarization is given as [58]

$$R_\perp = \frac{\eta_2 \cos(\theta_i) - \eta_1 \cos(\theta_t)}{\eta_2 \cos(\theta_i) + \eta_1 \cos(\theta_t)}; \ \ T_\perp = \frac{2\eta_2 \cos(\theta_i)}{\eta_2 \cos(\theta_i) + \eta_1 \cos(\theta_t)} \tag{2.6}$$

20
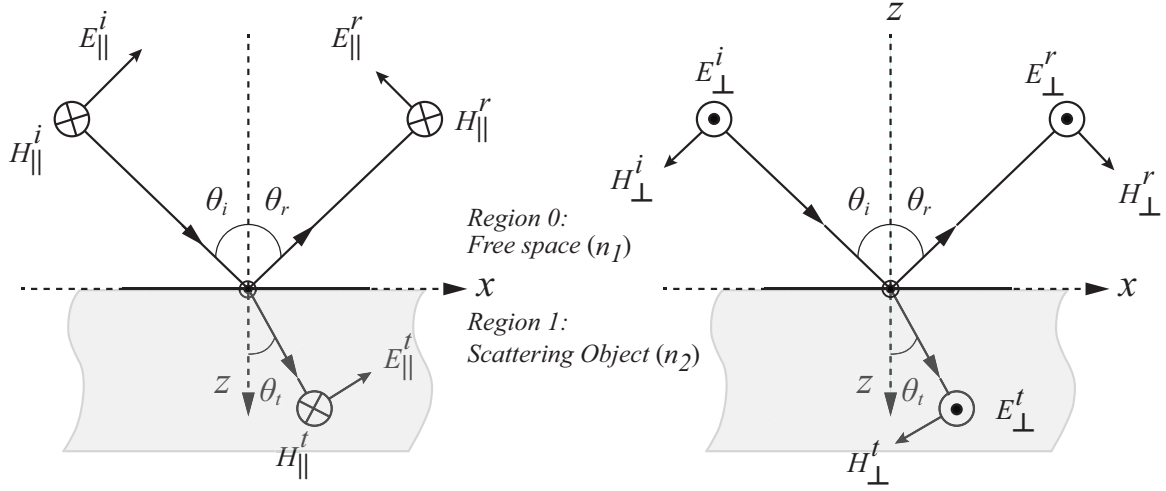
Figure 2-4: Reflection and Transmission of Parallely polarized incident wave (Left) and Perpendicularly polarized incident wave (Right)

where $R_\perp$ is the reflection coefficient, $T_\perp$ is the transmission coefficient, and η_1, η_2 are the complex refractive index of the materials. Similarly for the parallel polarization the Fresnel coefficients are given by [58]

$$R_\parallel = \frac{-\eta_1 \cos(\theta_i) + \eta_2 \cos(\theta_t)}{\eta_1 \cos(\theta_i) + \eta_2 \cos(\theta_t)}; \quad T_\parallel = \frac{2\eta_2 \cos(\theta_i)}{\eta_2 \cos(\theta_t) + \eta_1 \cos(\theta_i)} \tag{2.7}$$

For multi-layered materials the reflection coefficient is given by the equivalent coefficients at the interface between the free space and the first layer. There are many measurement campaigns carried out to determine the value of the dielectric properties and attenuation due to typical building materials [13][12][59][60]. A survey of these parameters appears in [4] and is shown in Table 2.1. The large variation in the parameters even for the same material is due to different samples used and the different composition. However it is clear that the attenuation by these common materials are high, making it difficult for Outdoor to Indoor propagation and existence of transmitted components under N-LOS conditions.

In order to discuss the dependence of the the reflection coefficients on polarization and the incident angles, we consider the case of only non-ferromagnetic materials

Table 2.1: Relative permitivity and attenuation due to common building materials near 60 GHz [4]

Material	$|\epsilon_r|$	Attenuation [dB/cm]
Brick	2.6 - 4.4	1.5 - 14.7
Concrete	3.1 - 6.5	3.7 - 17
Plasterboard	2.3 - 2.8	0.09 - 2.4
Glass	6.2 - 8.9	2.8 - 18.8
Plywood/wood	1.6 - 2.8	0.8 - 12
Vinyl floor	6.5 - 7.8	5.5 - 6.9

$(\mu_1 \approx \mu_2)$. The reflection coefficients for parallel and perpendicular polarizations can then be simplified to

$$R_\parallel = \frac{-\cos\theta_i + \sqrt{\frac{\epsilon_1}{\epsilon_2}}\sqrt{1 - \left(\frac{\epsilon_1}{\epsilon_2}\right)\sin^2\theta_i}}{\cos\theta_i + \sqrt{\frac{\epsilon_1}{\epsilon_2}}\sqrt{1 - \left(\frac{\epsilon_1}{\epsilon_2}\right)\sin^2\theta_i}} \tag{2.8}$$

$$R_\perp = \frac{\cos\theta_i - \sqrt{\frac{\epsilon_2}{\epsilon_1}}\sqrt{1 - \left(\frac{\epsilon_1}{\epsilon_2}\right)\sin^2\theta_i}}{\cos\theta_i + \sqrt{\frac{\epsilon_2}{\epsilon_1}}\sqrt{1 - \left(\frac{\epsilon_1}{\epsilon_2}\right)\sin^2\theta_i}} \tag{2.9}$$

where ϵ_1 and ϵ_2 are the permittivity of the materials. Figure 2-5 shows the variation of the reflection coefficients, for incident waves with parallel and perpendicular polarization, against the incident angle. For any given ratio of the material permittivity it is clear from the figure that the $R_\perp$ is almost always greater than $R_\parallel$. Also clear from the figure is that only in case of parallel polarization does the reflection coefficient become zero; $R_\parallel = 0$. This angle is known as the *Brewster angle*. This dependence of the reflection coefficient, which are also used to calculate the scattered field components (for instance by using physical optics (PO)) besides the specular reflection component, on the polarization can be used to interpret the difference in the strength of the propagation paths or the clusters under different polarization but for the same scattering object.
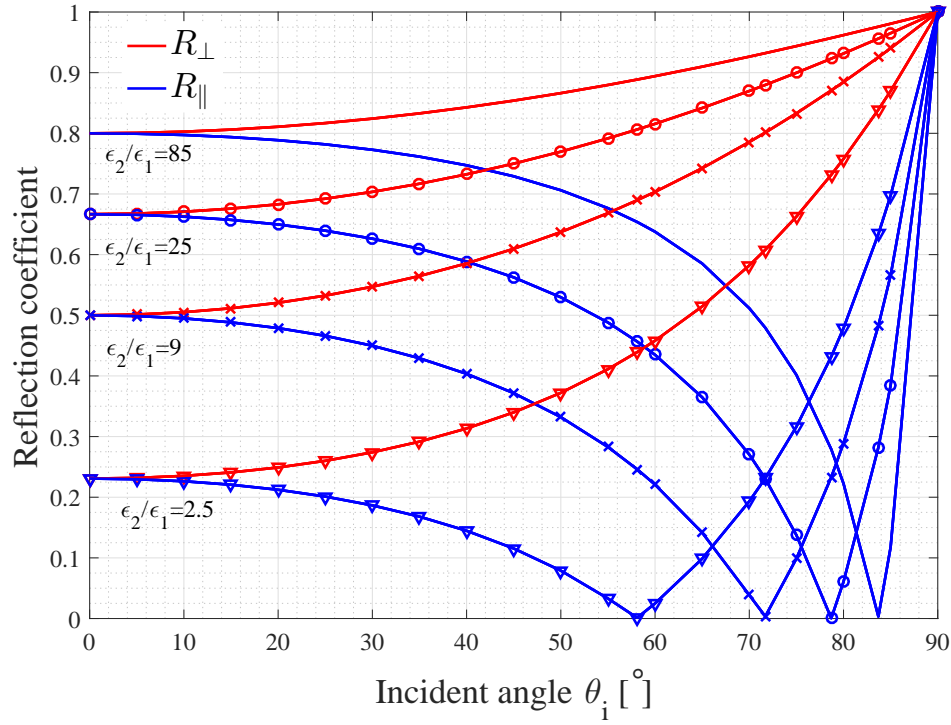
Figure 2-5: Reflection coefficients for parallel and perpendicular polarizations as a function of incident angle

2.2.3 Diffraction

When the surfaces on which the waves are incident are, smooth, electrically large and infinitely extended then the reflected and the transmitted fields can be found by using the above equations which is derived based on the geometrical optics (GO) approximations. However when the objects are not electrically large and is of finite size with surface discontinuities such as edges, vertices and corners, the field received at the receiver suffers from effects due to these discontinuities which is generally known as diffraction and is characterized by the diffraction coefficient. Diffraction is described under the Geometrical theory of diffraction (GTD) and the Physical theory of diffraction (PTD), mainly to explain what can not be predicted by the geometrical optics or the physical optics approximations, and is generalized under the uniform theory of diffraction (UTD) [58]. Diffraction of the visible light when passing through a slit, which is a common high school physics experiment, is an example in the visible

23
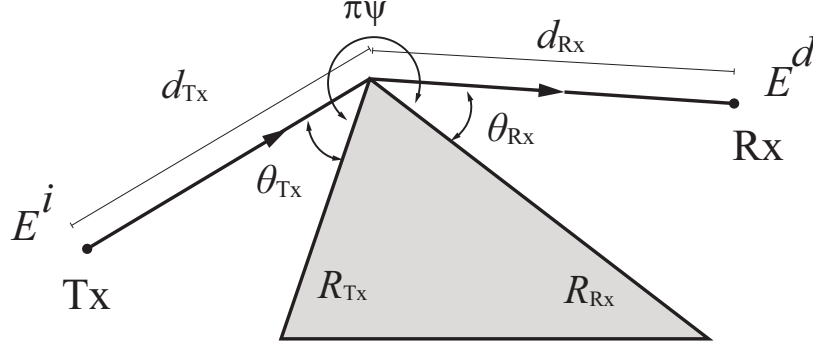
Figure 2-6: Diffraction from a wedge

electromagnetic spectrum. Diffraction is very a important propagation mechanism and in particular under non-line of sight conditions at microwave frequencies. A commonly found geometry of scattering surfaces that lead to diffraction in urban environment is the wedge structure represented in Figure 2-6. For this given geometry the diffracted field, E^d received at the observation point, Rx, due to an incident field E^i is given as [61]

$$E^d = E^i\, D(\theta_{\text{Tx}}, \theta_{\text{Rx}})\, A(d_{\text{Tx}}, d_{\text{Rx}}) \exp\left(-jk_0 d_{\text{Rx}}\right). \tag{2.10}$$

Here, $D(\theta_{\text{Tx}}, \theta_{\text{Rx}})$ is the diffraction coefficient. $A(d_{\text{Tx}}, d_{\text{Rx}})$ is the geometry factor and is given as

$$A(d_{\text{Tx}}, d_{\text{Rx}}) = \sqrt{\frac{d_{\text{Tx}}}{d_{\text{Rx}}(d_{\text{Rx}} + d_{\text{Tx}})}} \tag{2.11}$$

2.2.4 Scattering

In reality when a wave is incident on an object there are also scattered components other than just the specular reflected component irrespective of the material. The

24
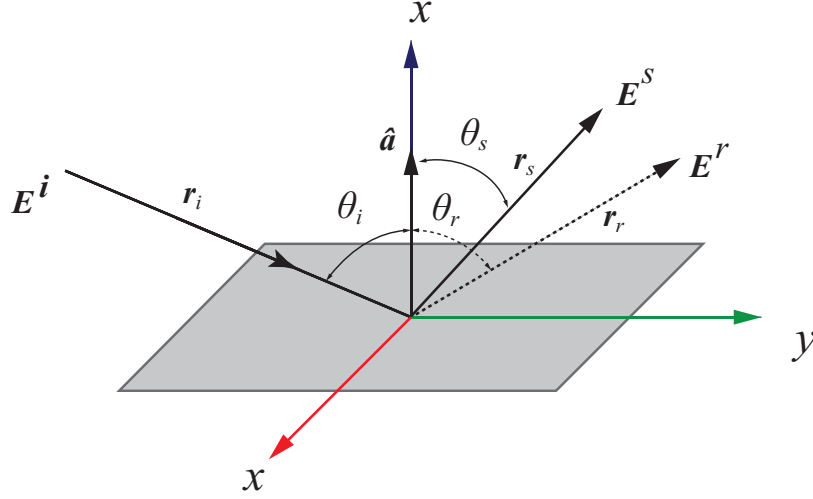
Figure 2-7: Scattering from a plane surface, E^s :non-specular component, E^r : specular reflection component.

specular reflected component is a good approximation in case of electrically large and smooth objects. This is the basis of geometrical optics (GO) and geometrical theory of diffraction (GTD), which forms the basis of ray tracing (RT). If the scattering object is at distances further than the far field distance from the source, the incident wave can be approximated as a plane wave. The scattered electric field at $\boldsymbol{r}_s$ can then be written as

$$\boldsymbol{E}^s(\boldsymbol{r}_s) = -\frac{j\omega\mu}{4\pi r_s} \exp^{-jkr_0} \iiint_S \left[\boldsymbol{J}_E - (\boldsymbol{J}_E \cdot \hat{\boldsymbol{r}}_0)\hat{\boldsymbol{r}}_0 + \frac{1}{Z_1}\boldsymbol{J}_M \times \hat{\boldsymbol{r}}_0 \right] ds' \qquad (2.12)$$

where $\boldsymbol{E}^s(\boldsymbol{r_s})$ is the scattered field at the observation point $\boldsymbol{r_s}$. $\boldsymbol{J}_E$ and $\boldsymbol{J}_M$ respectively are the electric and magnetic surface current densities on the scattering object. This is illustrated in Figure 2-7.

In practice, especially for higher frequencies, the roughness of the surface becomes important as the roughness dimensions become comparable to the wavelength of the incident wave. The most common way to handle this is by introducing the concept of effective reflection coefficient where the reflection coefficient is modified according to probability density function of the surface height and the correlation length, this

is generally known as the Perturbation theory. The special case when the spatial correlation is ignored; assuming that the points on the varying surface heights does not cast a shadow onto the other points, we get the *Kirchhoff theory*. For Gaussian distribution of the surface height, the modified reflection coefficient , R_{rough}, is written as [61]

$$R_{\text{rough}} = R_{\text{smooth}} \exp\left[-2(k_0 \sigma_{\text{h}} \sin \theta_{\text{i}})^2\right] \tag{2.13}$$

where, σ_{h} is the standard deviation of the surface height. Here R_{smooth} represents the reflection coefficient calculated for a smooth surface from 2.8 and 2.9.

2.3 The double directional channel

The double directional channel concept introduced in [62], which assumes the channel to be fully resolvable into multipath components (implicit plane wave assumption), can be used to completely describe the wide-band millimeter wave channel. The double directional channel impulse response, represented as the sum of contributions of the different multipath components (MPCs) is written as

$$h(t, \tau, \boldsymbol{\Omega}_{\text{R}}, \boldsymbol{\Omega}_{\text{T}}) = \sum_{r=1}^{R(t)} h_r(t, \tau, \boldsymbol{\Omega}_{\text{R}}, \boldsymbol{\Omega}_{\text{T}}) \tag{2.14}$$

where the rth MPC contribution is given as

$$h_r(t, \tau, \boldsymbol{\Omega}_{\text{R}}, \boldsymbol{\Omega}_{\text{T}}) = \gamma_r \exp\left(j\phi_r\right)\delta(\tau - \tau_r)\delta(\boldsymbol{\Omega}_{\text{R}} - \boldsymbol{\Omega}_{\text{R},r})\delta(\boldsymbol{\Omega}_{\text{T}} - \boldsymbol{\Omega}_{\text{T},r}) \tag{2.15}$$

where, $R(t)$ is the total number of MPCs at a time instance t, $\boldsymbol{\Omega}_{\text{R}} = [\vartheta_{\text{R}} \ \varphi_{\text{R}}]$ and $\boldsymbol{\Omega}_{\text{T}} = [\vartheta_{\text{T}} \ \varphi_{\text{T}}]$ are the angle of arrival (AoA) and angle of departure (AoD) of the MPCs respectively. ϕ_r, γ_r and τ_r are the phase, amplitude and delay of the rth path. The time dependence in 2.14 captures the effect of movement of the environment or the transmitter and receiver. This dynamic nature of the channel can be characterized by Doppler spectrum and its effect manifests as the Doppler spread. For a wide-band millimeter wave channel at 60 GHz, which is the focus of this study, the Doppler frequency due to the movements would be relatively small and therefore its effects would also be small. Thus the effect of the Doppler spread is not considered in this

study. Also the sounding system developed in this study is not capable of measuring the dynamic channel.

2.4 Channel characterization based on condensed parameters

For the static double directional channels, measured during the measurement campaigns in this study, condensed parameters such as the first-order moment (mean delay) and second-order central moments (rms delay spread) of the Delay power spectrum, and the central moment of the Angular power spectrum (angular spread) can be relatively easily obtained giving some insight into the channel. Condensed parameters are preferred to multivariate functions such as the correlation function because of the ease in dealing with a single variable function [61]. For a double directional channel impulse response in Equation (2.14), the Double Directional Delay Power Spectrum (DDDPS) can easily be shown to be,

$$DDDPS(\mathbf{\Omega}_{\mathrm{R}}, \mathbf{\Omega}_{\mathrm{T}}, \tau) = |h(\tau, \mathbf{\Omega}_{\mathrm{R}}, \mathbf{\Omega}_{\mathrm{T}})|^2 \qquad (2.16)$$

For an isotropic antenna at the MS, the Angular Delay Power Spectrum as seen from the BS is then

$$\mathrm{ADPS}(\mathbf{\Omega}_{\mathrm{T}}, \tau) = \iint DDDPS(\mathbf{\Omega}_{\mathrm{R}}, \mathbf{\Omega}_{\mathrm{T}}, \tau) \, d\vartheta_{\mathrm{R}} d\varphi_{\mathrm{R}}. \qquad (2.17)$$

Similarly, for an isotropic antenna at the BS, the Angular Delay Power Spectrum as seen from the MS is

$$\mathrm{ADPS}(\mathbf{\Omega}_{\mathrm{R}}, \tau) = \iint DDDPS(\mathbf{\Omega}_{\mathrm{R}}, \mathbf{\Omega}_{\mathrm{T}}, \tau) \, d\vartheta_{\mathrm{T}} d\varphi_{\mathrm{T}} \qquad (2.18)$$

2.4.1 Delay domain dispersion parameters

Using the ADPS from Equation (2.17) or (2.18) , and integrating it over the angular domain we can get the Delay Power Spectrum (DPS), also commonly known as the

Power Delay Profile (PDP), as shown below

$$DPS(\tau) = \int ADPS(\mathbf{\Omega}_\mathrm{T}, \tau) \, d\mathbf{\Omega}_\mathrm{T} \tag{2.19}$$

The channel parameters that can be obtained from the DPS are the, path gain, mean delay, rms delay spread and the maximum excess delay. Knowing the DPS, the path gain can be found as the zeroth-moment of the DPS, which is the time integrated power given as

$$P_m = \int_{-\infty}^{\infty} DPS(\tau) \, d\tau \tag{2.20}$$

The *mean delay*, which is defined as the normalized first-order moment of the DPS is given as

$$\tau_\mathrm{m} = \frac{\int_{-\infty}^{\infty} DPS(\tau)\tau d\tau}{P_m} \tag{2.21}$$

The other parameter is the *rms delay spread* which is defined as the normalized second-order central moment of DPS and is given by

$$\tau_\mathrm{rms} = \sqrt{\frac{\int_{-\infty}^{\infty} DPS(\tau)\tau^2 d\tau}{P_m} - \tau_\mathrm{m}^2} \tag{2.22}$$

The rms delay spread parameter gives the measure of delay spreading in the channel and is an important system design parameter that determines the inter-symbol interference in case of a single carrier schemes or equivalently the frequency selectivity in multiple carrier systems [63][61].

Excess delay, which is the difference of delays of the MPCs compared to the first arrival path (the shortest path) can also be easily determined. Maximum excess delay together with the rms delay spread and mean delay spread gives a more complete statistical description of the delay domain spreading.

2.4.2   Angular domain dispersion parameters

Similar to the delay domain, the angular power spectrum (APS) as seen from the MS side or the BS side can be determined from the respective sides ADPS as below

$$APS(\Omega_\mathrm{T}) = \int ADPS(\Omega_\mathrm{T}, \tau) \, d\tau \tag{2.23}$$

$$APS(\Omega_{\mathrm{R}}) = \int ADPS(\Omega_{\mathrm{R}}, \tau) \, d\tau \qquad (2.24)$$

The dispersion in the angular domain, known as the angular spread, can then be obtained from the APS. However, unlike the delay domain, in the angular domain the azimuthal angle is periodic. To avoid ambiguity due to this periodicity, the angular spread is defined as in [64], and for azimuthal spread it is written as

$$S_\varphi = \sqrt{\frac{\int |\exp(j\varphi) - \mu_\varphi|^2 APS(\varphi) \, d\varphi}{\int APS(\varphi) \, d\varphi}} \qquad (2.25)$$

where the mean μ_φ is defined as,

$$\mu_\varphi = \frac{\int \exp(j\varphi) APS(\varphi) \, d\varphi}{\int APS(\varphi) \, d\varphi} \qquad (2.26)$$

Here, $APS(\varphi) = \int APS(\varphi, \vartheta) \, d\vartheta$, is the marginal APS in the azimuth plane.

The angular spread gives us a measure of how the multipaths are dispersed in the angular domain, and therefore determines how effective spatial diversity and multiplexing schemes can be [63]. Angular spread values are also essential in designing effective antenna or in antenna array design.

2.5 Millimeter wave in Heterogeneous network

Understanding that the millimeter wave propagation is limited due the high attenuation by common building materials and the large scale free space path loss, the coverage range of a millimeter wave cell would be severely restricted (less than few 100 meters) compared to traditional lower frequency cells. Therefore if a network consists of only millimeter wave cells, it would mean that to achieve reasonable coverage a large number of cells would be required. The control overhead for handling cell discovery, user movement, radio resources allocation etc. in the network would become restrictively high. The preferred solution for the network operators is densification of the network by integrating millimeter wave small cells (phantom cells) [65] into the conventional cellular network, thereby giving rise to a heterogeneous network (HetNet). One of the proposed approach to this integration is by control plane and user
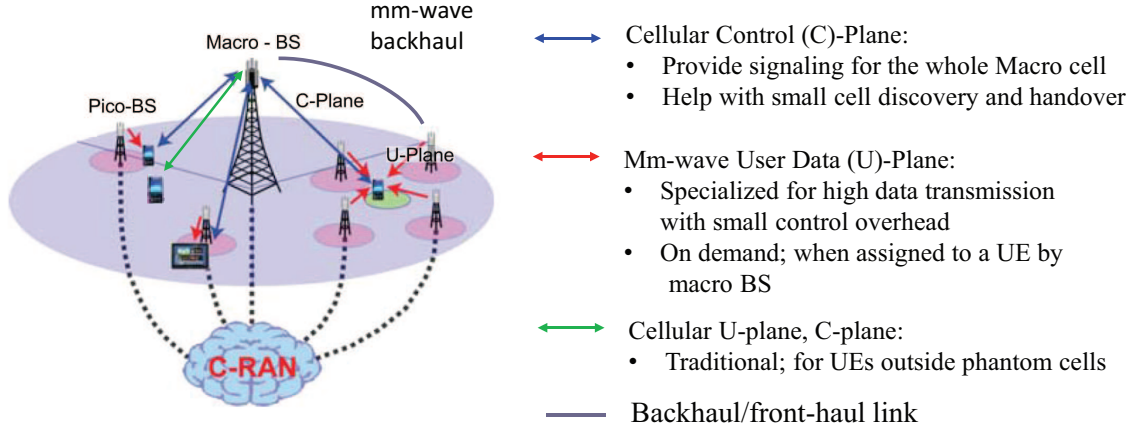
Figure 2-8: A Hetregeneous network with C/U plane splitting and cloud radio access network (C-RAN) [1]

plane (C/U plane) splitting [14]. In this approach the traditional macro base station will provide control signaling for the whole area and the millimeter wave cells will specialize in providing data resources with light control overhead. A heterogeneous network with C/U plane splitting and a centralized-RAN (C-RAN)[66] is illustrated in Figure 2-8.

2.5.1   Usage scenarios

Under the heterogeneous network configuration, the millimeter wave could support backhaul/fronthaul as well as the small pico-cell access link. The probable usage scenarios are considered in [54][67] for both the backhaul/fronthaul and access scenarios. In the backhaul/fronthaul scenario the the Tx and Rx location are fixed therefore not much is expected in terms of channel variation. However the access link is more challenging and the access link scenarios considered are:

1. Open area

2. Street canyon(ultra-high rate hot spots)

3. Hotel Lobby (Indoor high rate hot spots)

In this study we focus on street level ultra high-rate hot spots, where the area is fully covered by traditional macro cells and is supplemented by non overlapping

millimeter wave pico cells and the indoor high rate hot spots.

3 Millimeter Wave Channel Sounding

3.1 Introduction

To understand and characterize the wireless propagation channel, the the properties of the channel needs to measured. This process of measuring the channel response, either the frequency domain transfer function or the the delay domain impulse response, is known as channel sounding. The measurement system used is called a channel sounder.

The first part of this chapter describes the signal design and the hardware implementation of the sounding system developed for this study. The system is capable of full polarimetric double directional channel measurement.

The second part describes the synthesis of the polarimetric double directional channel impulse response from the directionally resolved measurements carried out using the system. The polarization specific condensed channel parameters can then be determined as discussed in the previous chapter. The millimeter wave propagation channel at 60 GHz is seen to be highly directional in nature, therefore a clustering and cluster based channel parametrization is discussed. A method used to identify the physical scattering object and the propagation mechanism corresponding to the clusters is introduced. Using these, the clusters that arises due to different propagation mechanisms under different polarization can be characterized and discussed.

3.2 Channel sounding system

A fully software defined radio based millimeter wave channel sounding system was developed for this study.

Millimeter wave channel sounding in both delay domain[68][37][69][69] and frequency domain[47][70][71] are reported in literature. This list is by no means exhaustive, and is meant to represent the various delay domain and frequency domain techniques used for channel sounding. Vector Network Analyzer (VNA) based systems are also very popular [72].

In our case we already had the baseband circuitry developed previously [73] [74] for a 11 GHz, 24×24 MIMO channel sounding system. Using the same platform and the baseband circuitry the system was modified for directional channel sounding at 60 GHz band. This channel sounder is a frequency domain system.

3.2.1 Channel Sounding Theory

For the baseband sounding signal, the system employs a complex unmodulated Newman phase multi-tone (NPM) given as

$$s(t) = \frac{1}{\sqrt{N}} \sum_{k=-N/2}^{N/2-1} \exp(\mathrm{j}2k\pi\Delta_F t + \mathrm{j}\phi_k) \tag{3.1}$$

where $\phi_k = \pi\frac{k^2}{N}$ is the Newman phase for peak-to-average power ration (PAPR) reduction. N is the number of sub-carriers over the considered bandwidth (400 MHz) spaced Δ_F from each other. The 11 GHz MIMO channel sounder [73][74] on which this sounder is based used Time division multiplexing (TDM), Frequency division multiplexing and Spatial multiplexing to achieve the 24×24 MIMO configuration. Frequency division multiplexing (FDM) and Spatial Multiplexing implementation for the current system is limited by the high phase noise introduced by the commercial RF front-end used. Therefore, only the TDM based multiplexing is retained. This implementation of the TDM based transmission frame effectively converts the system into a $N_\mathrm{T} \times N_\mathrm{R}$ MIMO with each TDM slot allocated to one of the N_T transmitters.
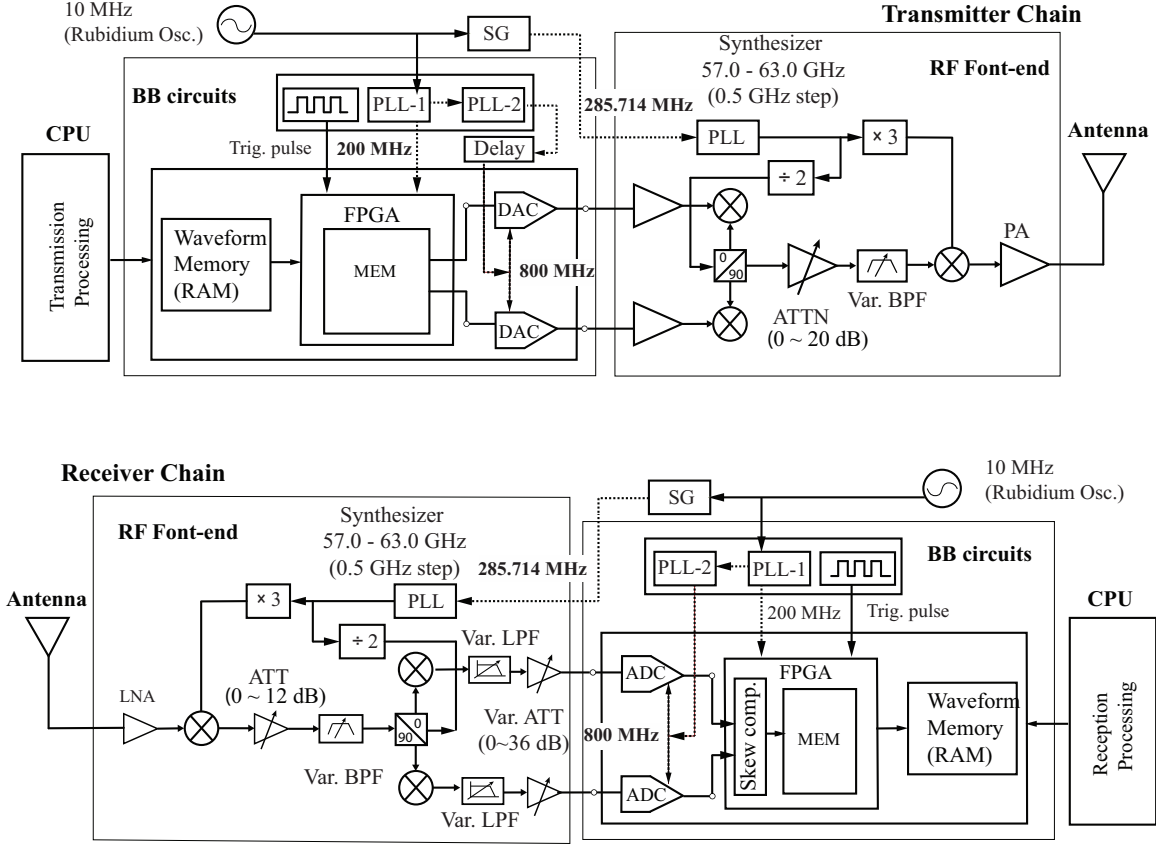
Figure 3-1: Schematic diagram of the channel sounding system (showing one Transmitter and one Receiver chain)

In each TDM slot an extra period of the signal $s(t)$ is transmitted to act as the cyclic prefix (CP) for aiding decoding at the receiver. Each TDM slot therefore has two periods of the multi-tone signal. If $\bar{s}(t)$ represent the transmitted signal in one TDM slot, then for the uth TDM slot the sounding signal is given as

$$x^{(u)}(t) = \bar{s}(t)g(t - (u - T)) \tag{3.2}$$

for $u = 1, ..., N_{\text{T}}$, T is the duration of $\bar{s}(t)$ and

$$g(t) = \begin{cases} 1, & \leq t < T \\ 0, & \text{otherwise} \end{cases}$$

If this signal is sampled in time at a sampling frequency $f_s = WR_{ov}$, where R_{ov} is the ratio of sampling frequency to the bandwidth referred to as the over-sampling

35

ratio, the discrete time samples can be be expressed as

$$s[n] = \frac{1}{\sqrt{N}} \sum_{k'=0}^{N_f-1} \bar{\Psi}_{k'} \exp\left(j\frac{2\pi}{N_f}k'n\right),$$ (3.3)

with $N_f = R_{ov}N$ and $\bar{\Psi}_{k'}$ is the interpolated NPM sequence in frequency domain given by

$$\bar{\Psi}_{k'} = \begin{cases} \sqrt{R_{ov}} \, \exp(j\phi_{k'}) & 0 \leq k' < N/2 \\ \sqrt{R_{ov}} \, \exp(j\phi_{N-N_f+k'}) & N_f \leq k' < N_f \\ 0 & \text{otherwise} \end{cases}$$

here multiplication by the factor $\sqrt{R_{ov}}$ is required in order to maintain the power of the sampled sequence same as that of the original signal. In the baseband unit this time sample can be calculated by taking N_f-point inverse fast Fourier transform (IFFT) of the time signal. The symbol duration of one TDM symbol then becomes $N_{sym}T_s = (N_{CP} + N_f)/f_s$. On the receiver baseband side the received signal vector in the uth TDM slot is given by

$$\boldsymbol{y}^{(u)}[i] = \sum_{\tau=0}^{N_{CP}-1} \boldsymbol{h}_{(u}[\tau]x^{(u)}[i-\tau] + \boldsymbol{z}^{(u)}[i],$$ (3.4)

for $i = 0, ..., N_{\text{sym}} - 1$, and $\boldsymbol{h}_u[\tau] \in \mathbb{C}^{N_R \times 1}$ is the uth column vector of the channel impulse response matrix $\boldsymbol{h}$. $\boldsymbol{z}^{(u)}[i]$ is the column vector of a complex AWGN process with power P_z. After removing the CP, (3.4) is converted to the frequency domain by DFT. Only extracting the lower half of the oversampled signal spectrum we get

$$\boldsymbol{Y}^{(u)}[k] = \boldsymbol{H}_{(u)}[k] \, \boldsymbol{X}^{(u)}[k] + \boldsymbol{Z}^{(u)}[k]$$ (3.5)

for $k = 0, ..., N-1$. Equation (3.5), indicates the SIMO channel during the, u^{th} TDM slot. If we now consider only the vth receiver, during the uth TDM slot the rceived signal over the SISO channel can be written as

$$Y^{(v,u)}[k] = H_{(v,u)}[k] \, X^{(v,u)}[k] + Z^{(v,u)}[k]$$ (3.6)

If we now assume that the channel is flat over the entire TDM symbol duration, then

we can suppress the TDM index and the MIMO channel matrix can be written as

$$\hat{\boldsymbol{H}}[k] = \boldsymbol{H}[k] + \boldsymbol{Z}[k]\boldsymbol{X}[k]^{-1} \tag{3.7}$$

Where $\boldsymbol{X}[k]^{-1} = \mathrm{diag}\,(\Psi_k \cdots \Psi_k) \in \mathbb{C}^{N_T \times N_T}$. The estimation accuracy, measured in terms of the normalized mean square error (NMSE) is therefore dependent on the received SNR indicated by the last term in (3.7), and is given as

$$NMSE = \frac{\sum_k |\hat{\boldsymbol{H}}[k] - \boldsymbol{H}[k]|^2}{\sum_k |\boldsymbol{H}[k]|^2} \tag{3.8}$$

3.2.2 Hardware Implementation

The system system block diagram showing a single transmitter and receiver chain is shown in fig.3-1. The base bands of transmitter and receiver units were implemented on the generic software defined radio (SDR) platform [75]. The platform consists of the Texas Instruments, DAC5682, four channel DACs with 16 bit resolution and the ADS5400 four channel ADCs with 12 bit resolution respectively; each operating at 800 MS/s. The baseband processing is achieved using the Xilinx Virtex-5 VLX110T FPGA. A 10 MHz reference clock output from a high performance Rubidium oscillator [76], with up to 10^{-11} in frequency accuracy, is used. The timing of the transmitter and receiver sounding frames are synchronized using a trigger pulse which itself is synchronized at the start of the measurement, during the calibration step. For indoor measurements a common reference clock is used for both the transmitter and the receiver. In case of measurement over longer distances (outdoor) separate clock is needed, synchronization then depends on the stability of the oscillators. A careful discussion on synchronization and its impact on channel sounding appears in [77], chapter 4 of [74].

In the RF front end the commercially available V60TXWG1 and V60RWG1 millimeter wave transmitter and receiver units from VubIQ inc. are used [78]. These units have a SiGe BiCMOS radio chip with integrated waveguide module supporting the WR15 flange interface allowing for direct connection to pyramid horn antennas. The radio employs heterodyne architecture taking in a reference clock at 285.714 MHz and
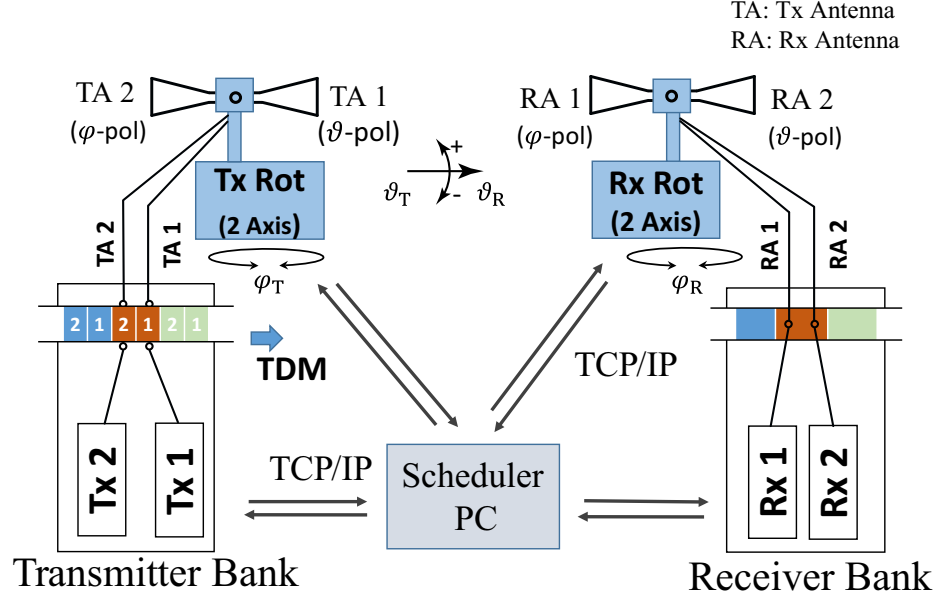
Figure 3-2: Block diagram of the implemented system. *Copyright* ©2017 IEICE [2]

capable of RF outputs ranging from 56 GHz - 63 GHz in 0.5 GHz steps. The system also supports user defined baseband with > 1 GHz modulated bandwidth at 60 GHz. An example plot, from the developed system, of the Baseband signal, the impulse response and the transfer function measured during the back-to-back calibration using a 60 dB wave guide is shown in Figure 3-4.

For measurement the developed system is set up in a 2×2 TDM based MIMO configuration as shown in Figure 3-2. In the current system the MIMO implementation is used primarily to speed up the polarimetric directional measurement of the SISO channel using high gain narrow-beam antenna connected to each of the two transmitters and the two receivers. On the receiver and the transmitter side the transmitting and receiving antennas are mounted on identical two axis rotators. The rotators have an angular resolution of 0.1^0 and are capable of $10°$ per second angular velocity in both the axis. Although the rotators can pan and tilt to cover the entire sphere, when pyramid horn antennas are mounted, due to their size the tilt range is limited between $-70°$ to $160°$.

For directional channel measurement a scheduling code written in MATLAB® is run in a scheduler PC. The scheduler PC is connected to the transmitter bank, the
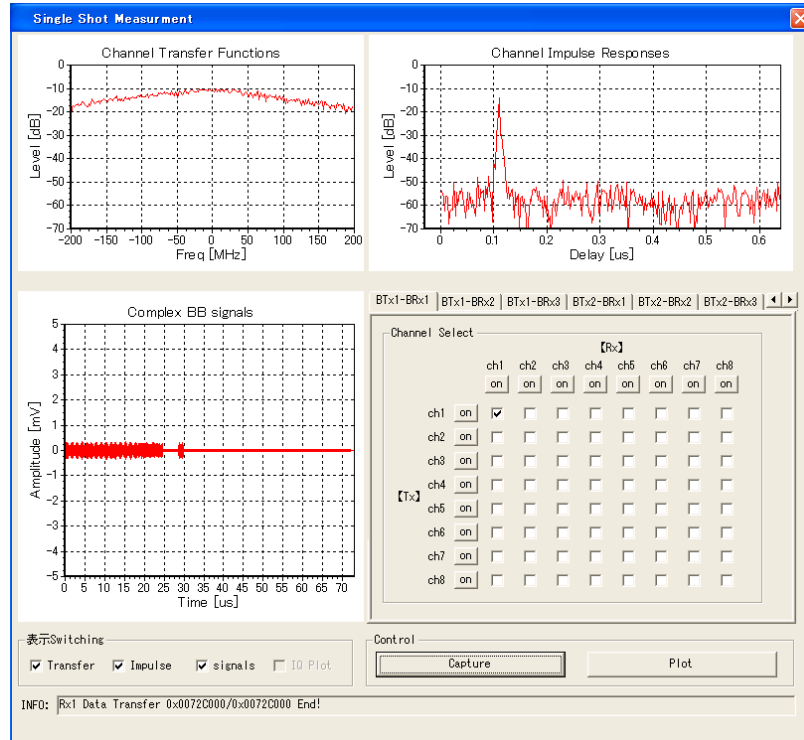
Figure 3-3: The plot of the CIR and Channel TF during back-to-back calibration
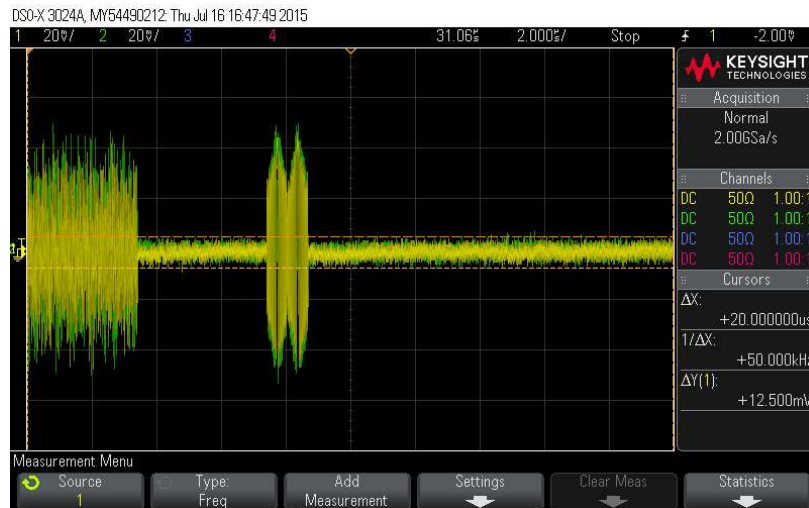
Figure 3-4: Base-band signal measured using an oscilloscope
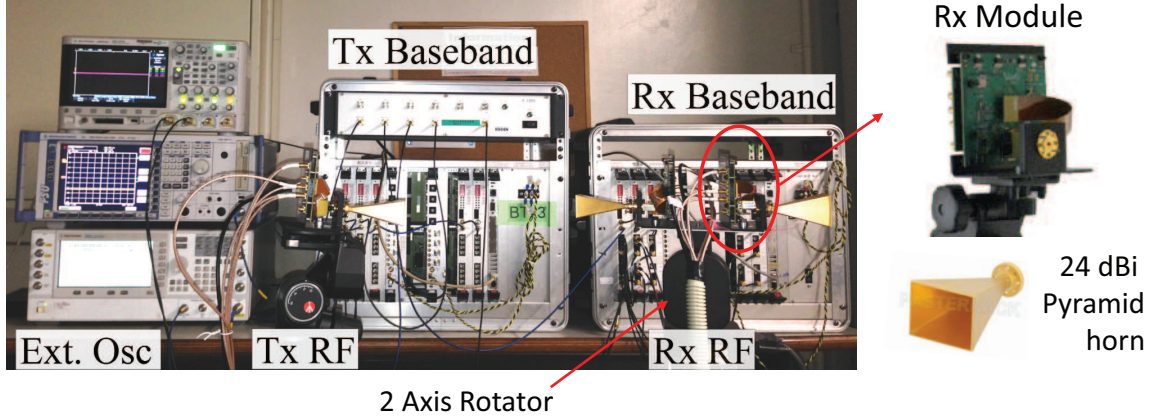
Figure 3-5: The actual sounding system

receiver bank, and the Tx and Rx antenna controllers through the TCP/IP interface. Depending on convenience we can use either wired or wireless connections. The actual system with the pyramid horn antennas is shown in Figure 3-5.

To measure the channel between any Base station (BS) and Mobile station (MS) positions, first the angular steps by which to rotate the Tx and the Rx antennas are determined. Then, for each Tx antenna location the Rx antenna is rotated over the entire steps. At each Rx antenna steps the channel is measured and stored at the receiver. This is repeated for all the Tx angular steps. If channel measurement is to be carried out over longer distances, then to compensate for the large free space path loss, directional antennas have to be used on both the BS and the MS side. This is one of the bottle necks of the millimeter wave channel sounding system and therefore the measurement time for each position is in the order of hours.

3.2.3 Signal design and system specification

The channel estimation error, measured using the NMSE, is highly influenced by the phase noise of the system and is mainly due to the phase noise of the PLL of the local oscillators. The phase noise effect can be separated into the common phase error (CPE) and the inter-carrier interference (ICI). The degradation in channel estimation accuracy due to ICI can be minimized by increasing the tone spacing. However the tone spacing and the symbol duration are inversely related and therefore the tone

spacing can not be made very large. Unlike in real data transmission, phase noise mitigation techniques are difficult to be applied to channel sounding because of the difficulty to separate the phase variation due to the phase noise of the system and the phase variation due to propagation. The phase noise of the developed system is shown in figure 3-6. The temporal variation of the simulated phase noise in the figure is generated by shaping the Gaussian noise with the spectrum shape modeled by approximated phase noise in the figure.

To evaluate the NMSE performance for different tone spacing, or the number of tones, a Rayleigh fading channel with, 20 paths, exponential power decay and $0.5\mu s$ delay spread is used. The NMSE performance plotted against the SNR is shown in figure3-7. At lower SNR the NMSE gain is dominated by the processing gain due to the increase in the number of tones. However with the increase in SNR the influence of the phase noise becomes increasingly dominant. For $N = 256$ tones, the low SNR and the high SNR performances are reasonably good compared to other number of tones, therefore 256 number of tones with tone spacing of 1.563MHz is chosen.

The digital signal pre-distortion schemes developed in [79][80] to counter degradation due to IQ imbalance (IQI) was retained from the 11 GHz channel sounder. With the IQI compensation, Image rejection ration (IRR) of upto -43dB is achieved. With this a NMSE$\approx 4 \times 10^-3$ at 30 dB SNR which corresponds to an EVM of approximately 6.3% is achieved. More discussion can be found in [3] and [77].

The specification of the designed system in shown in Table 3.1. The system bandwidth of 400 MHz equates to delay resolution of 2.5 ns. Including the processing gain from the FFT the actual dynamic range of the system was determined to be 64 dB.

3.3   Synthesis of the double directional channel

3.3.1   Measured double directional impulse response

Using the inverse discrete Fourier transform (IDFT) on the TF given by Eq. (3.7) we can get the impulse response (IR). For the sth snapshot of the channel between the
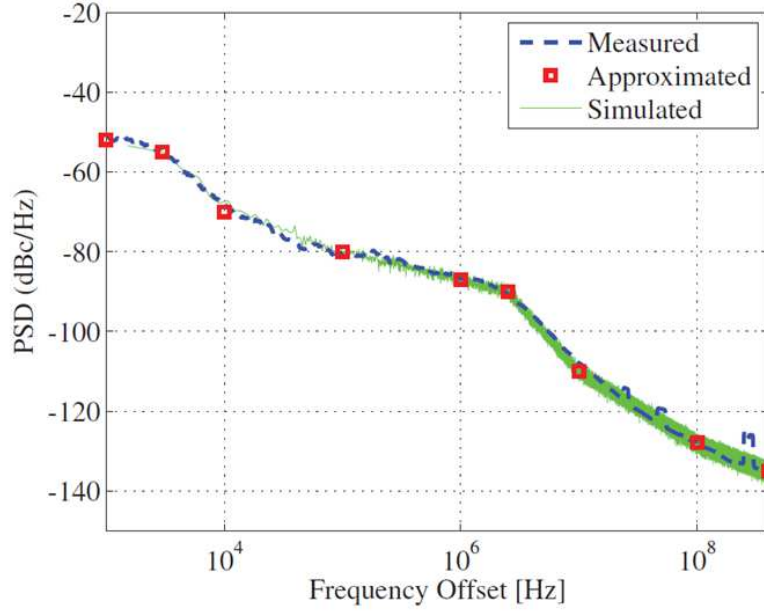
Figure 3-6: Phase noise of the developed system [3]
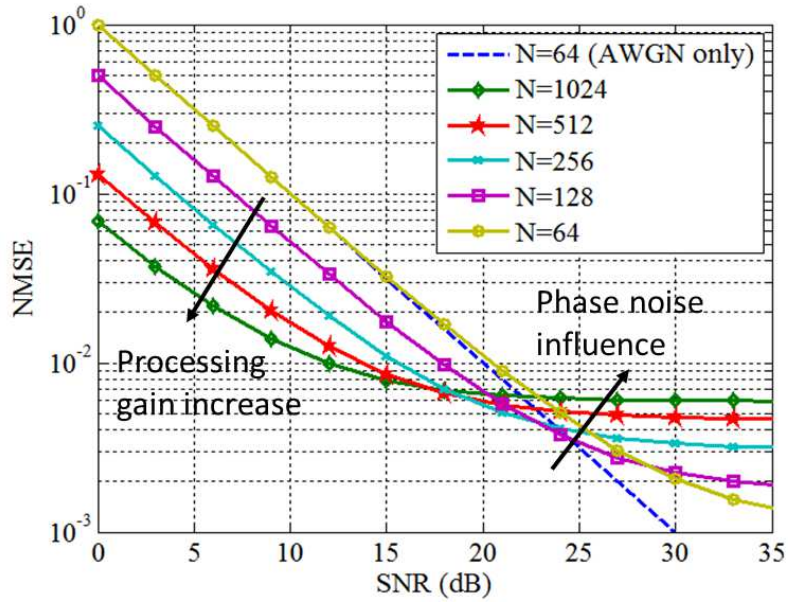
Figure 3-7: Channel estimation accuracy for different number of tones with phase noise[3]

Table 3.1: Designed System Specifications

Carrier frequency (f_c)	$57.0 \sim 60.0$ GHz (0.5 GHz step)
Signal bandwidth	400 MHz
Sampling frequency (f_s)	800 MHz
Number of tones (N)	256
Tone spacing (Δ_F)	1.563 MHz
TDM symbol length (N_{sym})	1024
TDM symbol duration (T)	1.28 μS
Maximum delay	160 nS
Delay resolution	2.5 nS
Maximum Dynamic range	64 dB

u^{th} transmit antenna and the vth receive antenna the measured IR is

$$\widetilde{h}_{v,u}^{(s)}[n] = \frac{1}{N} \sum_{k=0}^{N-1} \xi W[k] H_{v,u}^{(s)}[k] \, \exp\left(\mathrm{j}\frac{2\pi}{N} kn \right) \tag{3.9}$$

where k and n are the discrete frequency and delay indices respectively. Here a window function W is used in order to suppress the side-lobe effect in estimating the IR. The multiplication factor $\xi = N/\sum_{k=0}^{N-1} W[k] \cdot H_{(v,u)}^{(s)}[k]$ is required in order for the power of the time domain IR and the frequency domain TF to be maintained the same after applying the window function [81]. In this work a N-point symmetric Hann (Hanning) window is employed. The measured angle resolved impulse response, inclusive of the antenna response, for the pq polarization combination is then given as

$$\widetilde{h}_{qp}(n, \vartheta_{\mathrm{R},l}, \varphi_{\mathrm{R},m}, \vartheta_{\mathrm{T},a}, \varphi_{\mathrm{T},b}) = \widetilde{h}_{v,u}^{(s)}[n] \tag{3.10}$$

where $(\vartheta_{\mathrm{T},a}, \varphi_{\mathrm{T},b})$ and $(\vartheta_{\mathrm{R},l}, \varphi_{\mathrm{R},m})$ denotes the angle of departure (AoD) and the angle of arrival (AoA) respectively. Here the transmit antenna and receive antenna indices are replaced by the polarization of these antennas $p, q \in \{\vartheta-\mathrm{pol}, \varphi-\mathrm{pol}\}$ since each of the two Tx and Rx antennas have unique polarization. An example of the measured channel impulse response (including the antenna gains) for the base station (BS) and moible station (MS) located in and outdoor pico-cell environment is shown in Figure 3-8, and for the Rx and Tx antenna angles of $(\vartheta_{\mathrm{R}} = 0°, \varphi_{\mathrm{R}} = 330°, \vartheta_{\mathrm{T}} = 0°, \varphi_{\mathrm{T}} = 132°)$.
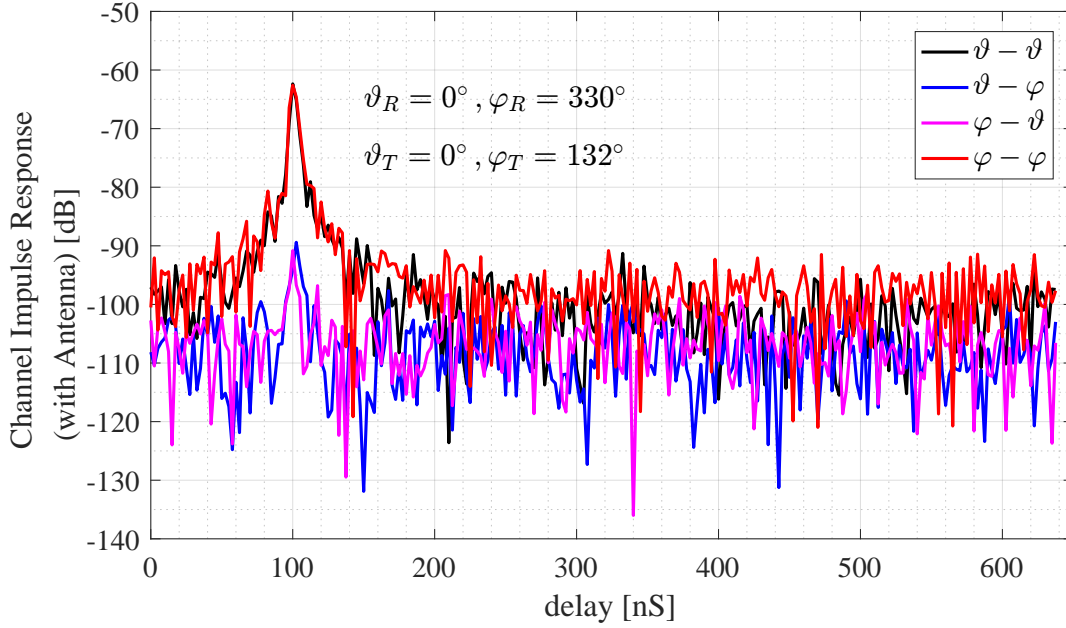
Figure 3-8: The measured channel impulse response (including the antenna gain) at MS_1 for the defined Tx and Rx antenna angles

3.3.2 Deconvolution of antenna response with CLEAN algorithm

The measured response in Equation (3.10), and the example shown in Figure 3-8, is the convolution of the true channel response with the response of the Rx and the Tx antennas respectively. This double directional convolution can be represented as

$$
\widetilde{h}_{qp}(n, \vartheta_{\mathrm{R}}, \varphi_{\mathrm{R}}, \vartheta_{\mathrm{T}}, \varphi_{\mathrm{T}}) = \sum_{b,a,l,m} \Big\{ \alpha_{\mathrm{R},q}(\vartheta_{\mathrm{R}} - l \cdot \Delta\vartheta_{\mathrm{R}}, \varphi_{\mathrm{R}} - m \cdot \Delta\varphi_{\mathrm{R}})
$$

$$
\cdot \, \Gamma_{\mathrm{e}}(n, l \cdot \Delta\vartheta_{\mathrm{R}}, m \cdot \Delta\varphi_{\mathrm{R}}, a \cdot \Delta\vartheta_{\mathrm{R}}, b \cdot \Delta\varphi_{\mathrm{R}})
$$

$$
\cdot \, \alpha_{\mathrm{T},p}(\vartheta_{\mathrm{T}} - a \cdot \Delta\vartheta_{\mathrm{T}}, \varphi_{\mathrm{T}} - b \cdot \Delta\varphi_{\mathrm{T}}) \Big\} + N_{\mathrm{R}} \quad (3.11)
$$

where $(\Delta\vartheta_{\mathrm{T}}, \Delta\varphi_{\mathrm{T}})$ represents the Tx elevation and azimuth angle scanning steps, and $(\Delta\vartheta_{\mathrm{R}}, \Delta\varphi_{\mathrm{R}})$ are the Rx elevation and azimuth angle scanning steps. $\alpha_{\mathrm{R},q}(\cdot)$ and $\alpha_{\mathrm{T},p}(\cdot)$ are the polarimetric complex response of the Rx and Tx antennas respectively. N_{R} is the receiver noise and Γ_{e} is the true channel impulse response. In the frequency domain, this is illustrated in Figure 3-9. We assume the antennas responses to be
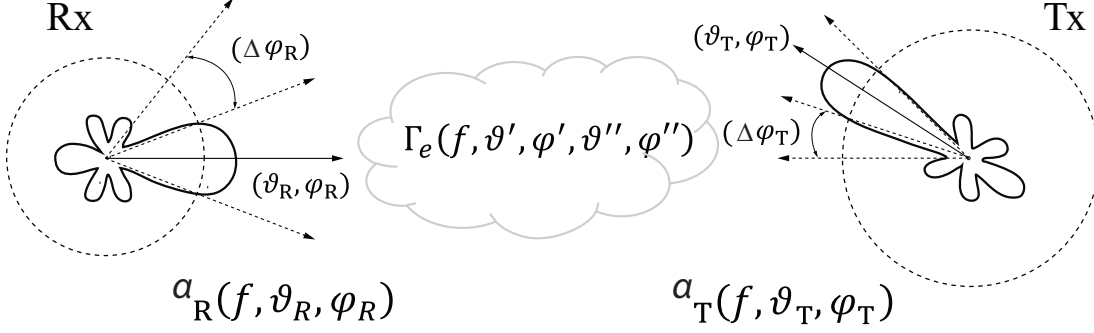
Figure 3-9: Illustration of the convolution in double directional channel

frequency flat over the bandwidth of the transmitted signal. In order to order obtain Γ_e, we need to deconvolve the Rx antenna response and the Tx antenna response, $\alpha_{R,q}(\cdot)$ and $\alpha_{T,p}(\cdot)$ from the Eq. (3.11). We only have the measured Tx and Rx antenna response covering the main lobe and the first side lobes. However for these standard gain horn antennas, the measured data matched well with the response simulated using CST®, 3-D Electromagnetic simulation software[82]; for the physical dimensions and material parameters specified by the manufacturer. In this study the simulated full 3D antenna responses were used.

To perform this multidimensional spatial deconvolution we implemented a slightly modified version of the very well known Hogbom's CLEAN algorithm [83]. The flow chart of the algorithm is shown in Fig. 3-10. For convenience we use the same terminology as in the original literature. To deconvolve the Rx antenna response for a qp polarization combination and for the Tx antenna position $\vartheta_T = \vartheta_{T,a}, \varphi_T = \varphi_{T,b}$, we first initialize the dirty map $D(n, \vartheta, \varphi)$, with the measured channel impulse response $h_{qp}(n, \vartheta_R, \varphi_R, \vartheta_{T,a}, \varphi_{T,b})$. The residual map is initialized to this same measured impulse response. The dirty beam, $B(\vartheta, \varphi)$, is initialized to the Rx antenna beam pattern, a_R, and the clean map matrix $C(n, \vartheta, \varphi)$ is set to zero. Just like in the original algorithm, we first search for the maximum peak in the dirty map, if the peak value is less than a certain threshold, γ, the algorithm is stopped (we set the threshold to be 5 dB above the noise floor). Otherwise the main lobe of the dirty beam is rotated to this peak location $(n_k, \vartheta_i, \varphi_j)$ and a fraction (also called loop gain,β) of the peak value is convolved with the rotated dirty beam, the result of this convolu-

START

$D(n,\vartheta,\varphi)$: Dirty map (Measurement)
$R(n,\vartheta,\varphi)$: Residual map
$C(n,\vartheta,\varphi)$: Cleaned map
$B(n,\vartheta,\varphi)$: Dirty beam (Antenna)
n_c: delay counter set
γ: Threshold

$D(n,\vartheta,\varphi)$
$= h_{qp}\big(n,\vartheta_{\mathrm{R}},\varphi_{\mathrm{R}},\vartheta_{\mathrm{T,a}},\varphi_{\mathrm{T},b}\big)$;
$R(n,\vartheta,\varphi) = D;\ C(n,\vartheta,\varphi) = 0;$
$B(\vartheta,\varphi); n_c = \emptyset;$

$\big(n_k,\vartheta_i,\varphi_j\big)$
$= \arg\max\limits_{n,\vartheta,\varphi} R(n,\vartheta,\varphi)\ \forall\ n \notin n_c$
$I_{max} = R(n_k,\vartheta_i,\varphi_j)$

Yes $\qquad I_{max} \leq \gamma \qquad$ Outer Loop

Exit

No

$R(n_k,\vartheta,\varphi) = R(n_k,\vartheta,\varphi) - \beta\,I_{max}\,B(\vartheta - \vartheta_i,\varphi - \varphi_j);$
$C\big(n_k,\vartheta,\varphi_j\big) = \beta\,I_{max}\ ;\ n_c = n_c \cup \{n_k\}$

$\big(\vartheta_i',\varphi_j'\big) = \arg\max\limits_{\vartheta,\varphi} R(n_k,\vartheta,\varphi)$
$I_{max}' = R(n_k,\vartheta_i',\varphi_j')$

Inner Loop

$I_{max}' \leq \gamma$

Yes $\qquad n \notin n_c \qquad$ No

No $\qquad$ Yes $\qquad$ Exit

$R(n_k,\vartheta,\varphi) = R(n_k,\vartheta,\varphi) - \beta I_{max}'\,B\big(\vartheta - \vartheta_i',\varphi - \varphi_j'\big);$
$C(n_k,\vartheta,\varphi) = \beta I_{max}';$
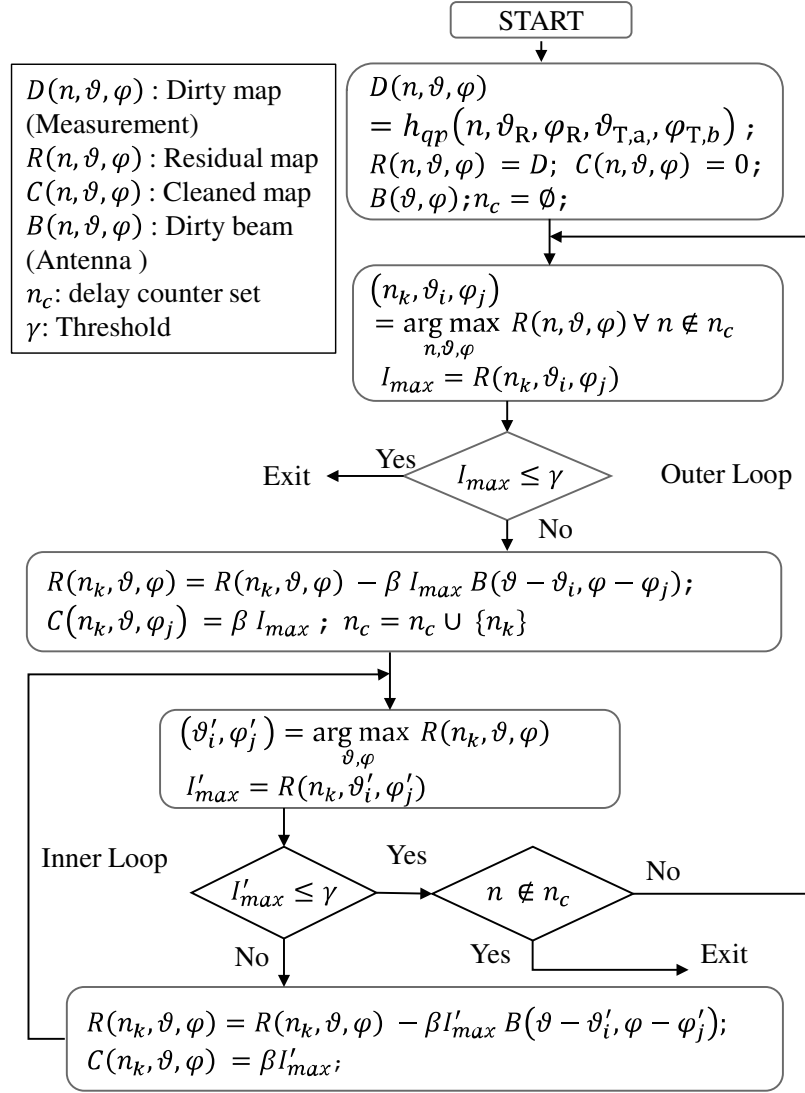
Figure 3-10: Flow chart of the modified CLEAN algorithm implemented. *Copyright* ⓒ2017 IEICE [2]

tion is subtracted from the residual map. A loop gain of $\beta = 0.1$ was used. This fraction of the peak value is then superimposed and stored at the same location as the detected peak(in dirty map) in the clean map. In our algorithm, since we use the delay domain responses each delay time bin is treated as orthogonal, and the CLEAN algorithm is applied over the spatial domain at each sampled delay time bins. It was found that for many delay time bins the maximum peak was already below the threshold, therefore an outer loop with delay time counter set n_c was introduced to

reduce the number of loops. This is done by first searching the global peak and the corresponding delay time location. At this delay time location the algorithm is applied in the inner loop. Once the execution in the inner loop is completed the next highest global peak is searched and the algorithm is repeated. If the detected global peak delay time location corresponds to the one that has already be detected, the algorithm is stopped. The algorithm is repeated for all the Tx antenna positions and for all the other polarization combinations. The clean map after running these steps corresponds to the channel impulse response convolved only with the Tx antenna. The entire step is repeated again on the clean map obtained from the above steps, but this time using the Tx antenna as the dirty beam. The clean map obtained after this then corresponds to the the channel impulse response with both the Tx antenna response and the Rx antenna response deconvolved. The cleaned channel response is denoted as $C_{qp}(n, \vartheta_R, \varphi_R, \vartheta_T, \varphi_T)$ for the pq polarization combination.

3.3.3 Full polarimetric double directional delay power power spectrum

Due the threshold used to avoid dealing with the signals near the noise floor level (for convergence of the algorithm), the cleaned map will contain elements that are equal to zero. Discarding these elements and assuming each delay bin to be composed of only a single path, the cleaned map can be expressed as the summation of the different paths in a more familiar form as

$$C_{pq}(\tau, \mathbf{\Omega}_R, \mathbf{\Omega}_T) = \sum_{r=1}^{R} \gamma_{pq,r} \exp\left(j\phi_r\right)\delta(\tau - \tau_r)\delta(\mathbf{\Omega}_R - \mathbf{\Omega}_{R,r})\delta(\mathbf{\Omega}_T - \mathbf{\Omega}_{T,r}) \quad (3.12)$$

where, R is the total number of rays or paths remaining after cleaning, $\mathbf{\Omega}_R = [\vartheta_R \ \varphi_R]$ and $\mathbf{\Omega}_T = [\vartheta_T \ \varphi_T]$. ϕ_r, $\alpha_{pq,r}$ and n_r are the phase, amplitude and delay of the rth path under pq polarization. Equation (3.12), is the double directional impulse response [61] for the pq polarization. The *polarimetric double directional 3-D impulse response* can

then be written as

$$h(\tau, \mathbf{\Omega}_\mathrm{R}, \mathbf{\Omega}_\mathrm{T}) = \sum_{r=1}^{R} \Gamma_r \exp{(j\phi_r)} \delta(\tau - \tau_r) \delta(\mathbf{\Omega}_\mathrm{R} - \mathbf{\Omega}_{\mathrm{R},r}) \delta(\mathbf{\Omega}_\mathrm{T} - \mathbf{\Omega}_{\mathrm{T},r}) \qquad (3.13)$$

where,

$$\mathbf{\Gamma}_r = \begin{bmatrix} \gamma_{\vartheta\vartheta,r} & \gamma_{\vartheta\vartheta,r} \\ \gamma_{\varphi\vartheta,r} & \gamma_{\varphi\varphi,r} \end{bmatrix} : \text{ is the polarimetric amplitude of the } r^\mathrm{th} \text{ ray.}$$

$\gamma_{\vartheta\vartheta,r}$ and $\gamma_{\varphi\varphi,r}$ are the co polarization components and $\gamma_{\vartheta\varphi,r}$ and $\gamma_{\varphi\vartheta,r}$ are the cross polarization components.

Form the 3-D double directional channel impulse response in Equation (3.13), the Double Directional Delay Power Spectrum (DDDPS) can be synthesized and will be the same same as Equation 3.14. Separating the DDDPS into different polarization combinations, the polarization specific DDDPS can be written as

$$DDDPS_{pq}(\mathbf{\Omega}_\mathrm{R}, \mathbf{\Omega}_\mathrm{T}, \tau) = |h_{pq}(\tau, \mathbf{\Omega}_\mathrm{R}, \mathbf{\Omega}_\mathrm{T})|^2 \qquad (3.14)$$

Once we have obtained the polarization specific $DDDPS_{pq}$, the delay power spectrum DPS_{pq} and the angular power spectrum $ADPS_{pq}$ functions for different polarization combinations can be synthesized. Knowing these functions the condensed parameters that characterize the channel can be determined as discussed in Section 2.4.

3.4   Clustering of multipath components

In order to understand the directional characteristics of the channel we use the KPowerMeans (KPM) algorithm detailed in [84] to cluster the multi-path components (MPCs). The algorithm performs clustering by minimizing the multipath component distance (MCD) [85] between the paths based on their delay, AoA and AoD. The optimal cluster number is found by combining several cluster validation indices (CVI) using average rank aggregation method [86]. The CVIs used are the same as in [87]. We assume that each impulse in the DDDPS as composed of a MPC or of group of MPCs. In order to make the clustering more efficient, only the MPCs with power

within 25 dB below the power of the peak MPC and above 5 dB of the noise floor were selected for clustering; similar to the threshold used in determining the delay dispersions in section 4.3.1. Initially, to determine all the clusters that can be seen for all the polarization conditions, clustering is performed for MPCs selected from the synthesized all polarization combined double directional delay power spectrum, $DDPS_{comb}$ which is given as,

$$DDDPS_{\mathrm{comb}}(\mathbf{\Omega}_{\mathrm{R}}, \mathbf{\Omega}_{\mathrm{T}}, \tau) = \frac{1}{2} \sum_{pq} DDDPS_{pq}(\mathbf{\Omega}_{\mathrm{R}}, \mathbf{\Omega}_{\mathrm{T}}, \tau) \qquad (3.15)$$

where the polarization indices, $p = \{\vartheta, \varphi\}$ and $q = \{\varphi, \vartheta\}$. We have to halve the combined power in Equation (3.15) to account for the power doubled due to transmission from two transmitter chains.

Clustering for individual polarization cases are performed independently and then compared to the clusters obtained from $DDDPS_{\mathrm{comb}}$. Cluster in individual polarization cases with slight deviation (deviation in the position of the cluster centroid, which is defined later) from clusters obtained for $DDDPS_{\mathrm{comb}}$ are assumed to correspond to the nearest $DDDPS_{\mathrm{comb}}$ cluster. In other words, all the clusters observed in individual polarization cases are also observed in $DDDPS_{\mathrm{comb}}$ case. We can make this assumption since clusters centroids are meant to correspond to real scattering objects in the environment and the same scatter would give rise to clusters in all the other polarization combinations.

3.4.1 Multipath component cluster centroid

Once clustering is achieved from the direction($\mathbf{\Omega}_{\mathrm{R}}, \mathbf{\Omega}_{\mathrm{T}}$), delay(n) and power of the MPCs in the clusters, the cluster centroid location can be uniquely defined by the weighted mean, $\mu = (\bar{n} \ \bar{\vartheta}_{\mathrm{R}} \ \bar{\varphi}_{\mathrm{R}} \ \bar{\vartheta}_{\mathrm{T}} \ \bar{\varphi}_{\mathrm{T}})$, which for the lth cluster is given as

$$\bar{\xi}_l = \frac{\sum_{k=1}^{K} \xi_{kl} \, p_{kl}}{\sum_{k=1}^{K} p_{kl}}, \qquad (3.16)$$

where ξ can be any of the $n, \vartheta_{\mathrm{R}}, \varphi_{\mathrm{R}}, \vartheta_{\mathrm{T}}, \varphi_{\mathrm{T}}. p_{kl}$ is the power of the kth MPC of the lth cluster; which corresponds to the DDDPS value of that path. K is the total number of paths in the l^{th}cluster. The total power of the lth cluster (or the cluster gain), P_l,

is given by

$$P_l = \sum_{k=l}^{K} p_{kl} \tag{3.17}$$

3.4.2 Delay and Angular domain dispersions from multipath clusters

Knowing all the individual multipaths within the clusters, we can now determine the delay spread and the angular spreads in terms of these multipaths. In terms of the detected and clustered multipaths the angular spread definition by Fleury in Equation (2.25) can now be written as

$$S_{\mathbf{\Omega}} = \sqrt{\frac{\sum_{l=1}^{L} \sum_{k=1}^{K_l} |\exp(j\mathbf{\Omega}) - \mu_{\mathbf{\Omega}}|^2 \, p_{kl}}{\sum_{l=1}^{L} \sum_{k=1}^{K_l} p_{kl}}} \tag{3.18}$$

where,

$$\mu_{\mathbf{\Omega}} = \frac{\sum_{l=1}^{L} \sum_{k=1}^{K_l} \exp(j\mathbf{\Omega}) \, p_{kl}}{\sum_{l=1}^{L} \sum_{k=1}^{K_l} p_{kl}} \tag{3.19}$$

Similaly, the rms delay spread in terms of the clustered multipath components can be written as

$$\tau_{\mathrm{rms}} = \sqrt{\frac{\sum_{l=1}^{L} \sum_{k=1}^{K_l} |\tau_{kl} - \tau_m|^2 \, p_{kl}}{\sum_{l=1}^{L} \sum_{k=1}^{K_l} p_{kl}}} \tag{3.20}$$

where,

$$\tau_m = \frac{\sum_{l=1}^{L} \sum_{k=1}^{K_l} \tau_{kl} \, p_{kl}}{\sum_{l=1}^{L} \sum_{k=1}^{K_l} p_{kl}} \tag{3.21}$$

Equation 3.18 and 3.20 are equivalent to Equation 2.25 and 2.22 respectively. The polarization specific, angular spread and delay spread for the different MS locations can be obtained by considering only the paths found in the $DDDPS_{pq}$.

3.4.3 Intra cluster delay and angular domain dispersion

Analyzing the overall delay and the angular spread at a particular receiver position it is seen that the spread values are very dependent on the number of clusters that are detected. The multipaths are very sparse in both the delay and the angular domain. What this means is even if the calculated delay and angular spread values are large it necessarily mean that the environment is rich in multipath since by the definition few multipath clusters far apart in the delay and the angular domain and result in similarly wide spread values. Therefore from one position to another position of the MS location to better understand the characteristics of the individual clusters we determine the root mean square (rms) delay spread and rms angular spreads, in both elevation and azimuth, from the MPCs in each cluster. A better way to understand the delay and angular dispersion would be to analyze the dispersions in individual clusters. This is particularly relevant when using high gain narrow beamwidth antennas or beamforming with arrays, where due to the narrow beamwidth only one or at most a couple of clusters might only be seen.

Similar to how we determined the overall delay and the angular spread values at a particular MS location, in the previous section, we can apply the same definition of the delay dispersion and angular dispersion but this time limiting the angular and delay range to that of only a single cluster. Therefore the cluster the angular spread and the delay spread of the lth cluster about its centroid is can be estimated similar to [88] as

$$\sigma_{\xi_l} = \sqrt{\frac{\sum_{k=1}^{K}(\xi_{kl} - \bar{\xi}_l)^2 P_k}{\sum_{k=1}^{K} P_{kl}}}, \tag{3.22}$$

where, ξ can be any of the $n(\text{delay}), \vartheta_{\text{R}}, \varphi_{\text{R}}, \vartheta_{\text{T}}, \varphi_{\text{T}}$.

4 Millimeter Wave Propagation in Outdoor Environment

In order to study the characteristics of millimeter wave propagation in outdoor environment, in this study we mainly focus on the street level access link of future heterogeneous network usage scenario. Such a scenario corresponds to an ultra-high-rate hot spot urban pico-cell environment, where the BS is mounted on street furniture like street lamp posts and the MS is held by a person. Study and characterization of this access links under both the LOS and the O-LOS condition considered is directly relevant to how millimeter would be deployed in future heterogeneous network. Understanding these parameters will help in antenna and system design and also desining algorithms such as beam forming or beam-steering which will be crucial at this frequency bands.

4.1 Measurement campaign in urban pico-cell environment

A measurement campaign was carried out at the Ikarashi campus in Niigata university, Japan. The outline of the environment and the location of the base station (BS) and the mobile stations (MS) are shown in Figure 4-1. The transmitter is placed at the BS location and the receivers are placed at the MS locations. The BS and the MS are at 30m∼32m away from each other. The transmitter antennas are mounted on a tripod at $3\,\mathrm{m}$ height, which is roughly the practical height for mounting on a street furniture such as street lamp post, sign post, traffic light poles etc. The receiver antennas were
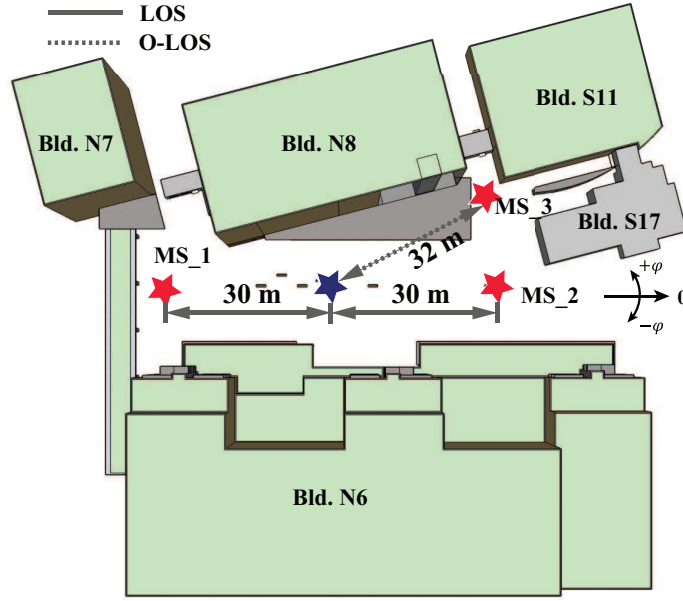
Figure 4-1: Outdoor picocell environment and the BS and MS locations. *Copyright* ©2017 IEICE [2]

mounted on tripods at heights of 1.35 m, which is roughly the waist height of an adult person; this is relevant assuming the person is using a mobile device such as a smart phone, tablet etc. One central BS location and three MS locations, MS_1, MS_2 and MS_3 were chosen. MS_1 and MS_2 represents a line of sight condition (LOS) and MS_3 represents an obstructed line of sight condition (O-LOS), since there is a concrete pillar and glass panel with metallic frame blocking the line of sight between the BS and MS_3. Panorama pictures taken with a 360° camera ,[89], mounted at the exact BS and MS locations are in shown in Figure 4-2. The obstructions in the O-LOS condition between BS and MS_3 can be clearly seen in the panorama picture taken at MS_3; bottom of Figure 4-2.

4.2 Full polarimetric double directional channel sounding

On both the receiver and the transmitter side, one transmitter-receiver chain is connected to a ϑ polarized antennas and the other chain is connected to φ polarized
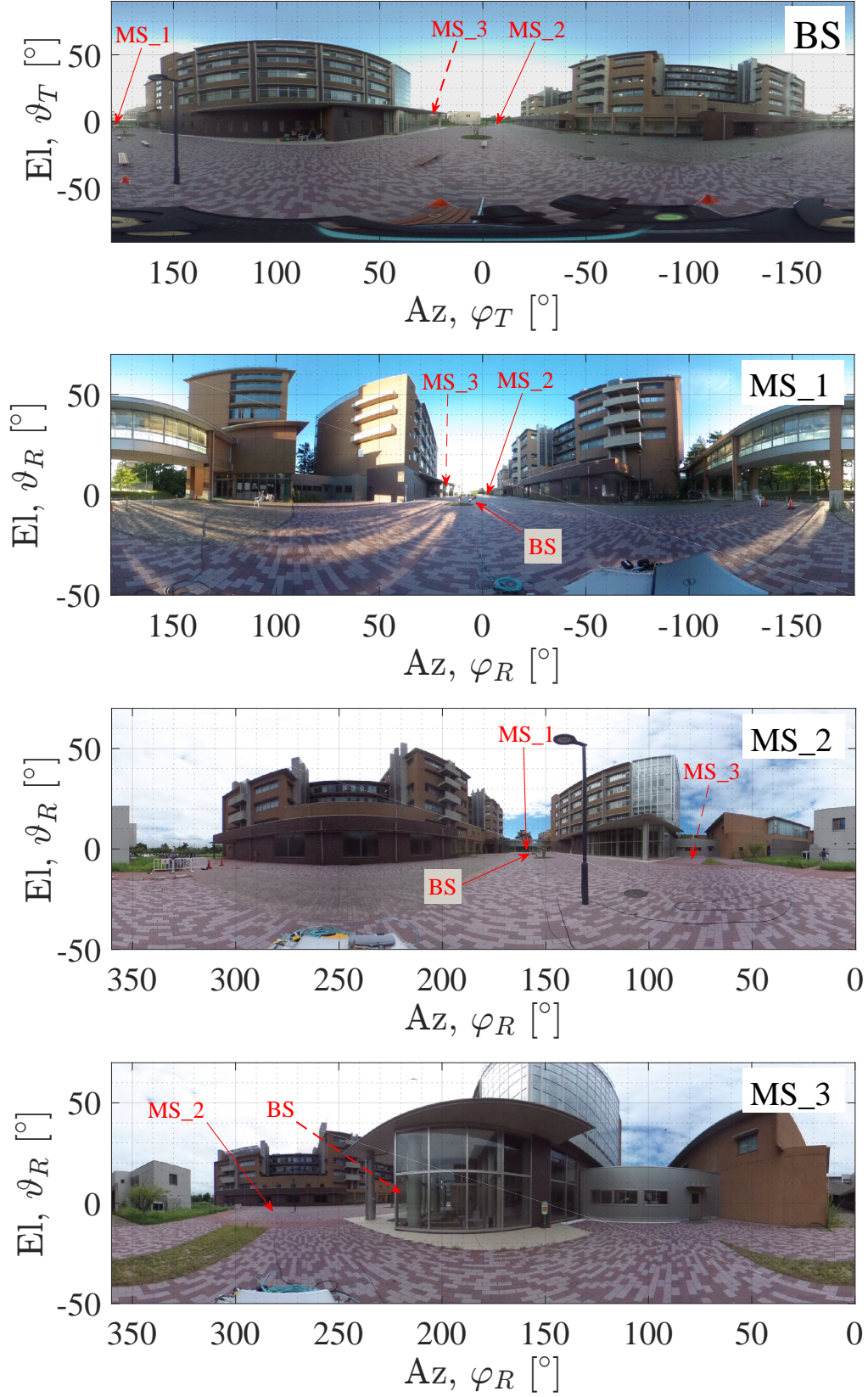
Figure 4-2: Panorama view from BS and MS locations

antennas. This configuration gives us all the four linear polarization combinations, co polarization (co-pol) case with φ-φ and ϑ-ϑ polarizations, and cross polarization (cx-pol) case with φ-ϑ and ϑ-φ polarizations. The sounding parameters and measurement settings are summarized in the Table 4.1. To carry out double directional channel measurement, two 24 dBi, 12° Half power beam-width (HPBW) pyramid horn antennas [90], one in ϑ polarization and one in φ polarization configuration is mounted on the two axis rotator and then connected to the two Tx chains. These antennas have an operating bandwidth from 50 GHz $\tilde{}$ 75 GHz. Similarly on the Rx side, two 15 dBi, 30° HPBW pyramid horn antennas [90], each with either ϑ polarization or φ polarization is mounted on an identical two axis rotator and connected to the two Rx chains. The antennas on the Tx side and the ones on the Rx side are mounted such that they face diametrically opposition to each other. This mounting configuration ensures that one full sweep in the either the azimuth plane, the elevation plane or both the planes, results in a full sweep for both the antennas (and hence both the polarizations). Therefore when we construct the double directional channel from measurement we assume that the environment is static. With this set-up we can not measure the dynamic channel. This is a common limitation of the millimeter wave channel sounding systems using high gain directional antennas.

In this particular measurement measurement campaign, we scan the BS side antennas at an angular steps of 12° (= HPBW) in both the elevation and azimuth plane, and at 30° (=HPBW) angular steps on the MS side, also both in elevation and azimuth planes. On both the BS and the MS side a full 360° scan was done in the azimuth plane. However on the elevation plane we limited the angular range from 24° to −24° (5 steps) on the BS side and from 30° to −30° (3 steps) on the MS side. These limits were required to avoid the measurement time from becoming impractically long. Examining the environment from the panorama pictures in Figure 4-2, we can see that the elevation angles < 30° covers most of the environment, except for those near the top of the buildings. The contributions from these scattering objects at the top of the building could be neglected on the account of the large distances from both the BS and the MS side.

Table 4.1: Sounding Parameters and Measurement Settings for Outdoor Measurement Campaign

Frequency (f_c)	58.5 GHz
Signal bandwidth	400 MHz
Sampling frequency (f_s)	800 MHz
No. of sub-carriers (tones) (N)	256
TDM symbol length (N_{sym})	1024
TDM symbol duration (T)	1.28 μs
Tone spacing (Δ_F)	1.563 MHz
Maximum delay	640 ns
Delay resolution	2.5 ns
Dynamic range	64 dB
Tx Power (P)	10 dBm
Tx antenna height (BS)	3 m
Rx antenna height (MS)	1.35 m
Tx antenna	Pyramid Horn , 24 dBi, 12° HPBW
Rx antenna	Pyramid Horn , 15 dBi, 30° HPBW
Tx - Rx antenna XPD	36 dB (measured; when fully aligned)
$[\vartheta_{\text{T}}, \varphi_{\text{T}}]$	$[-24° \sim 24°, 0° \sim 348°]$
$[\vartheta_{\text{R}}, \varphi_{\text{R}}]$	$[-30° \sim 30°, 0° \sim 330°]$

4.3 Delay domain and Angular domain dispersion due to pico-cell environment

From the polarimetric double directional impulse response measured by the system, during the measurement campaign in and outdoor pico-cell environment, we can construct the various delay and angular power spectrum functions to determine the channel parameters. The determination of these functions and the channel parameters follow Section 3.3. An example plot of the $ADPS(\mathbf{\Omega}_{\text{T}}, \tau)$ at MS_1, with slice planes at $\vartheta = \vartheta_T$, is shown in Figure 4-3. Even from this plot the clustering tendency in delay and angular domain is quite evident.

4.3.1 Polarization specific delay domain dispersion

Using the polarization specific $ADPS_{pq}$ from Equation (2.17), and integrating it over the angular domain we can get the Delay Power Spectrum DPS_{pq}. The DPS_{comb} (for
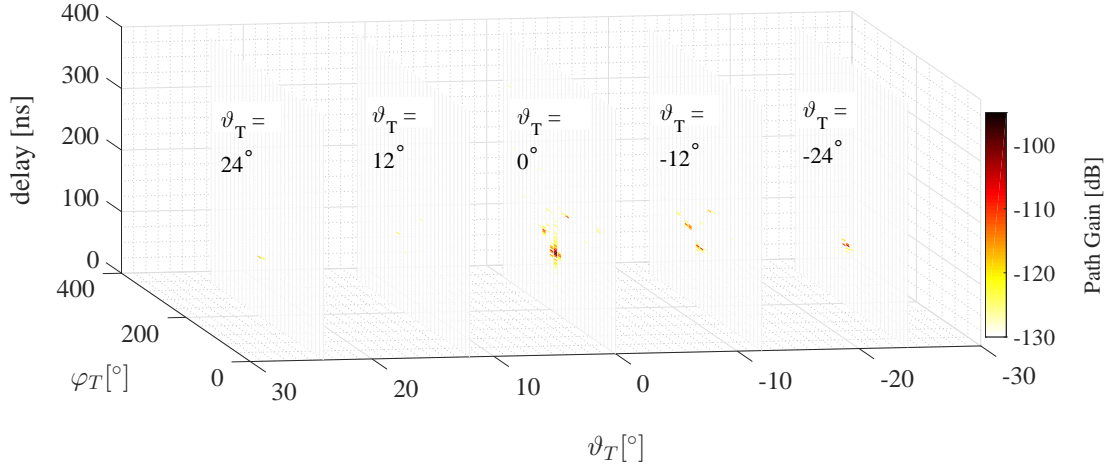
Figure 4-3: $\vartheta - \vartheta$polarization DAPS as seen from the BS for MS_1 (LOS)

all the polarization combinations), derived from the $DDDPS_{\mathrm{comb}}$ defined in 3.15, for the three MS locations and are shown in Figure 4-4, Figure 4-5 and Figure 4-6.

Looking at the DPS plots, in all the three locations we observe that the channel is composed of very sharp peaks at few of the delay location, indicating that the millimeter wave channel is specular in nature in the delay domain. Another important observation is the presence of more than one peaks in almost all the co-pol cases, and in few of the cx-pol cases. This means even if the peaks correspond to only a single path, there are paths other than the direct path (or the direct wave), that can be used for establishing the link. This makes the study of the directional properties important.

The channel parameters that can be obtained from the DPS are the, path gain P_m (2.20), mean delay τ_m(2.21), rms delay spread τ_{rms} 2.22 and the maximum excess delay τ_{excess}.

In practice to avoid detecting artifacts and noisy peaks it is common to use a threshold from the maximum peak of the DPS, and a threshold above the noise floor [52] in determining the peaks to consider for calculating the delay spread parameters. In our case to calculate the rms delay spread only those peaks in the DPS with values, within 25 dB below the maximum peak but 5 dB above the noise floor was
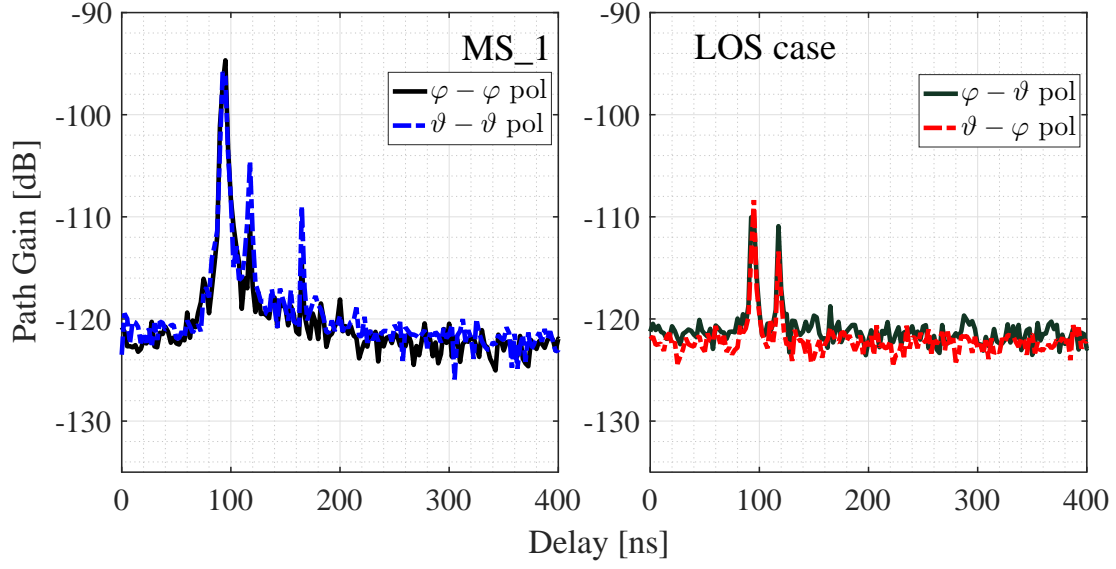
Figure 4-4: Delay power spectrum at MS_1; (left)cx-pol, (right)co-pol
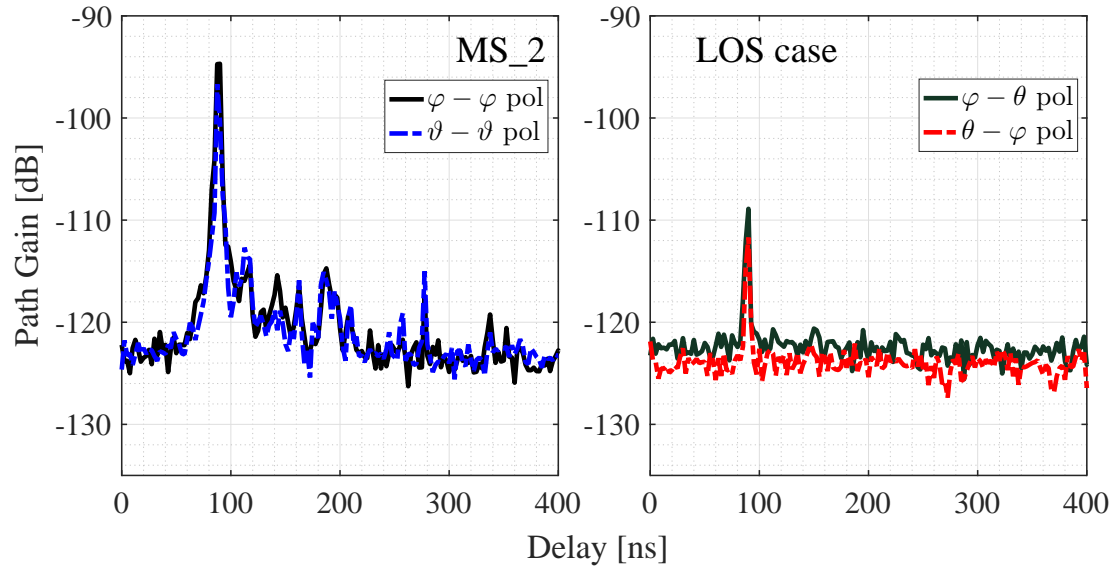
Figure 4-5: Delay power spectrum at MS_2; (left)cx-pol, (right)co-pol
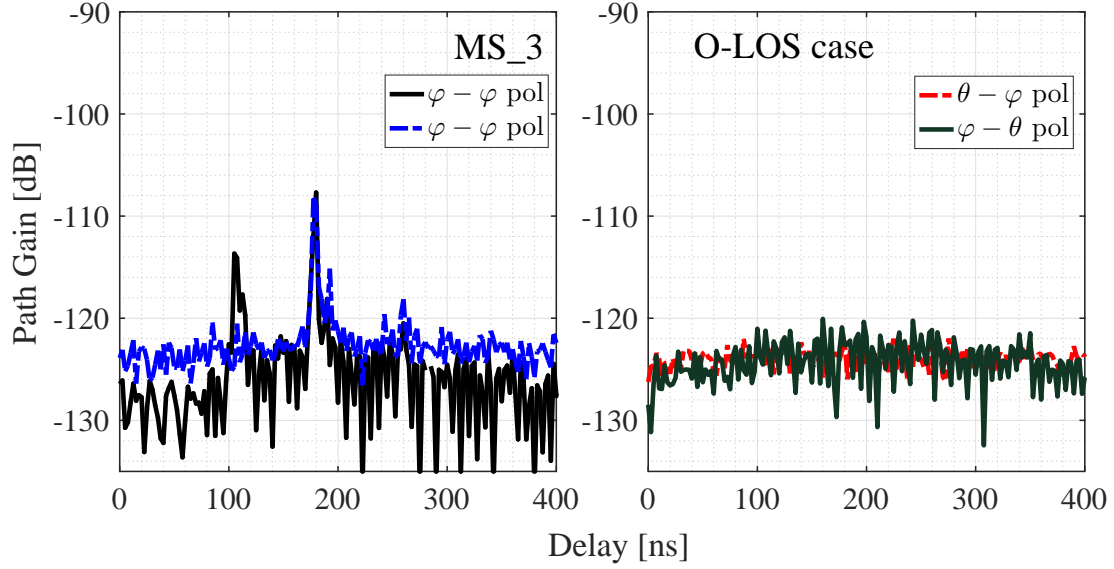
Figure 4-6: Delay power spectrum at MS_3; (left)cx-pol, (right)co-pol

considered. Once the peaks and their delays are determined we also obtain another delay parameter known as the excess delay. Excess delay is the difference of delays of the detected peak from the first detected peak in the delay domain (ie. the shortest path). Table 4.2 shows the overall rms delay spread, and the maximum excess delay parameters calculated for the MS locations under LOS condition. In case of LOS condition, the $\vartheta - \vartheta$ polarization always shows larger rms delay spread ranging from 12.2 ns to 25.4ns. The $\vartheta - \varphi$ polarization shows the least delay spread with values varying from 1.2ns to 9.5ns.

In Table 4.3 the delay spread and the maximum excess delay values for the MS position under O-LOS condition is shown. Unlike the LOS case the $\varphi - \varphi$ polarization shows much larger delay spread. Howerver there were no path detected during the cross polarization cases. It will be clear from later sections that the large spread in the $\varphi - \varphi$ case is due to the presence of the diffracted paths.

Although the number of samples are limited, we can reasonably infer that the delay spread values are much larger in both the LOS and O-LOS case for co-polarization compared to cx-polarization. Considering only the co-pol cases, we can say that the co-pol delay spreads under O-LOS condition is much higher than for LOS conditions,

if the diffracted paths are seen at the receiver. If diffracted paths are not seen at the receiver than the O-LOS delay spread values are relatively lower than the LOS delay spreads.

4.3.2   Polarization specific angular power spectrum

Similar to delay domain, the power spectrum in the angular domain is given by the integrating the ADPS over the delay domain. Depending on the direction, the APS as seen from the BS, defined in (2.23) and the APS as seen from the MS as defined in (2.24). Moreover taking into account the polarization of the propagating waves, the polarization specific Angular Power Spectrum $APS_{pq}(_T)$ and $APS_{pq}(_R)$ can be similarly determined from the respective $ADPS_{pq}$. The marginal APS in the azimuth plane as seen from the BS for the three MS locations and for all polarization combinations are shown in Figure 4-7, Figure 4-8 and Figure 4-9.

From these marginal angular power spectrum in azimuth and elevation we can determine the angular spread as defined in (2.25). The angular spread gives us a measure of how the multipaths are dispersed in the angular domain, and therefore determines how effective spatial diversity and multiplexing schemes can be [63]. Angular spread values are also essential in designing effective antenna, in antenna array design and designing beam-forming, beam-switching, beam-tracking algorithms.

Looking at the azimuth APS in Figures (4-7, 4-8 and 4-9) we can see that due to the limited resolution in the angular domain the patterns have very broad lobes. Therefore, if we perform peak detection analogous to the delay domain, the paths can not fully resolved and the angular spread parameters calculated subsequently would not correspond to the actual spread.

We constructed the APS in Equation (2.23) from the ADPS and the ADPS in turn from the DDDPS. In each step we reduced the parameter dimension and therefore sacrificed the corresponding information. However, since we already have the measured DDDPS we can leverage the extra dimensions and use it to determine the angular spread. For this purpose we first cluster the MPCs.

Table 4.2: Delay spread under LOS condition

| Polarization | | LOS | | | | | |
| | | MS_1 | | | MS_2 | | |
		τ_m [ns]	τ_{rms} [ns]	τ_{excess} [ns]	τ_m [ns]	τ_{rms} [ns]	τ_{excess} [ns]
co pol	$\vartheta - \vartheta$	105.7	12.2	172.5	106.3	25.4	290
	$\varphi - \varphi$	104.7	11.8	172.5	108.4	18.3	207.5
cx pol	$\varphi - \vartheta$	111.4	7.4	125	101.6	1.2	102.5
	$\vartheta - \varphi$	106.7	9.5	125	101.6	1.2	102.5

Table 4.3: Delay spread under O-LOS condition

| Polarization | | O-LOS | | |
| | | MS_3 | | |
		τ_m [ns]	τ_{rms} [ns]	τ_{excess} [ns]
co pol	$\vartheta - \vartheta$	182.3	4.3	195
	$\varphi - \varphi$	165.4	30	182
cx pol	$\varphi - \vartheta$	NA	0	0
	$\vartheta - \varphi$	NA	0	0

4.4 Multipath clusters in outdoor pico-cell environment

The multipath components detected from the $DDDPS_{comb}(\Omega_R, \Omega_R)$ defined in (3.15) are clustered using the KPM algorithm as described in Section 3.4.

The result of clustering for $DDDPS_{comb}$ at all the MS locations, as seen from both the BS and the MS sides are shown in Figure. 4-10,Figure. 4-11 and Figure. 4-12. The location of the centroid is indicated by the stem plot. Different color indicate different cluster and each ($\circ$) marker corresponds to individual multipaths. From these figures it is very clear that the millimeter wave propagation channel at 60 GHz is very directional in nature. Knowing all the individual multipaths arriving at the MS location we can now determine the dispersion in angular domain.
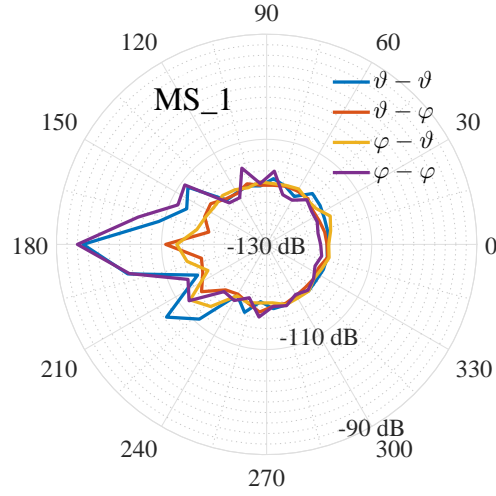
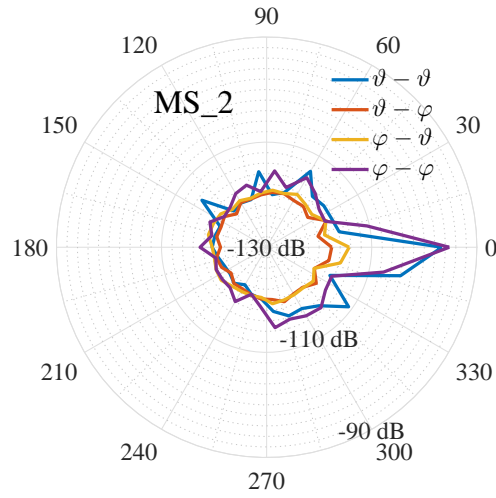Figure 4-7: Azimuth angular power spectrum at MS_1 as seen from the BS

Figure 4-8: Azimuth angular power spectrum at MS_2 as seen from the BS
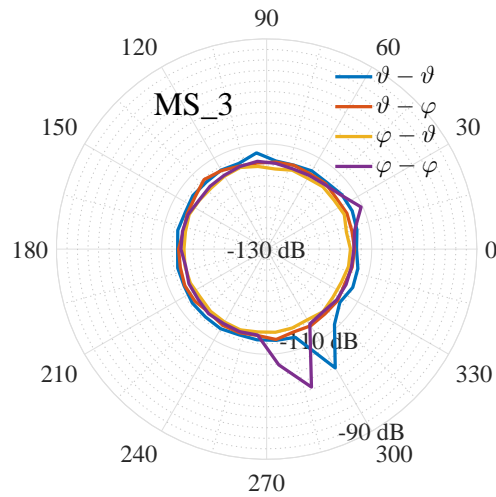
Figure 4-9: Azimuth angular power spectrum at MS_3 as seen from the BS

4.4.1 Polarimetric Angular domain dispersion in pico-cell environment

From the individual multipaths contained in different clusters the over angular spread of the channel, for different polarization combinations, can be determine as discussed in section 3.4.2.

The polarization specific, angular spread values obtained using (3.18),for the different MS locations are given in Table 4.4 and Table 4.5.

Table 4.4: Double directional Angular spread under LOS condition

Polarization		LOS							
		MS_1				MS_2			
		BS side		MS Side		BS side		MS side	
		S_{φ_T}	S_{ϑ_T}	S_{φ_R}	S_{ϑ_R}	S_{φ_T}	S_{ϑ_T}	S_{φ_R}	S_{ϑ_R}
co pol	$\vartheta - \vartheta$	12	3.3	17.6	1.4	15.5	5.6	13.4	3.3
	$\varphi - \varphi$	6	5.9	6.8	2	8.3	3.4	10.8	5.3
cx pol	$\varphi - \vartheta$	18.3	4.2	15	25.9	5.2	5.1	16.2	0
	$\vartheta - \varphi$	17.7	6.5	39	14.8	8.8	8.8	28.9	14.2

Table 4.5: Double directional Angular spread at under O-LOS condition

Polarization		O-LOS			
		MS_3			
		BS side		MS Side	
		S_{φ_T}	S_{ϑ_T}	S_{φ_R}	S_{ϑ_R}
co pol	$\vartheta - \vartheta$	23.8	3.1	11.3	1.6
	$\varphi - \varphi$	36.3	5.9	15.2	2.5
cx pol	$\varphi - \vartheta$	NA	NA	NA	NA
	$\vartheta - \varphi$	NA	NA	NA	NA

4.5 Cluster based characterization of the channel

It has been already illustrated in the previous section how the millimeter wave propagation paths can be clustered together based on their delay or path length, $\boldsymbol{\Omega}_{\mathrm{R}}, \boldsymbol{\Omega}_{\mathrm{R}}$, and power. Knowing that the channel can be decomposed into clusters of the multipaths, we can understand the characteristics of the channel by understanding the
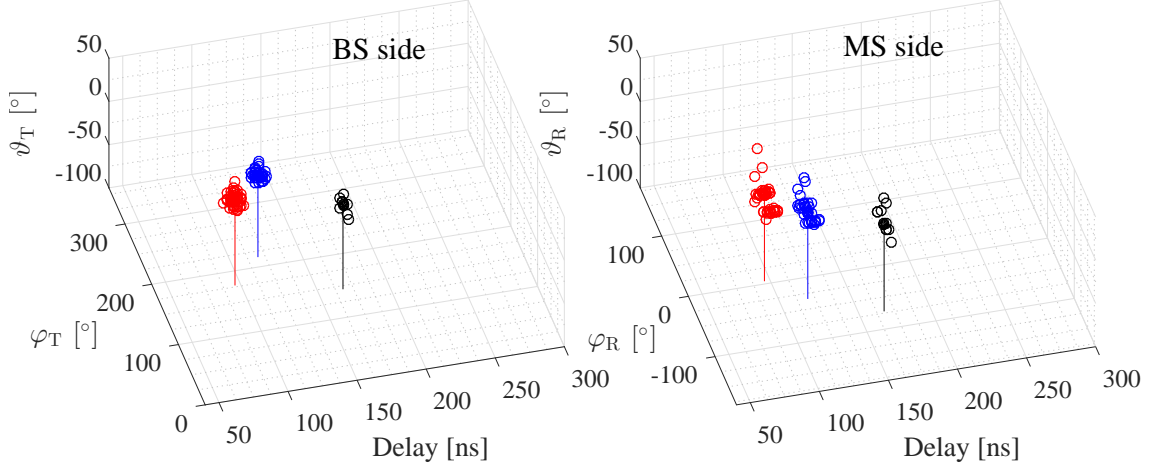
Figure 4-10: Clustered multipath components from $DDDAPS_{\mathrm{comb}}$ at MS_1
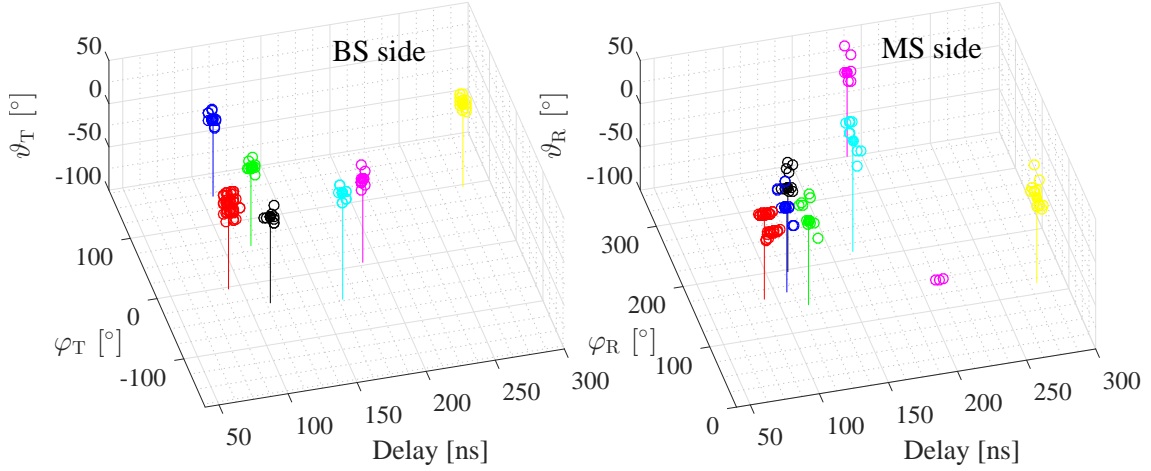
Figure 4-11: Clustered multipath components from $DDDAPS_{\mathrm{comb}}$ at MS_2
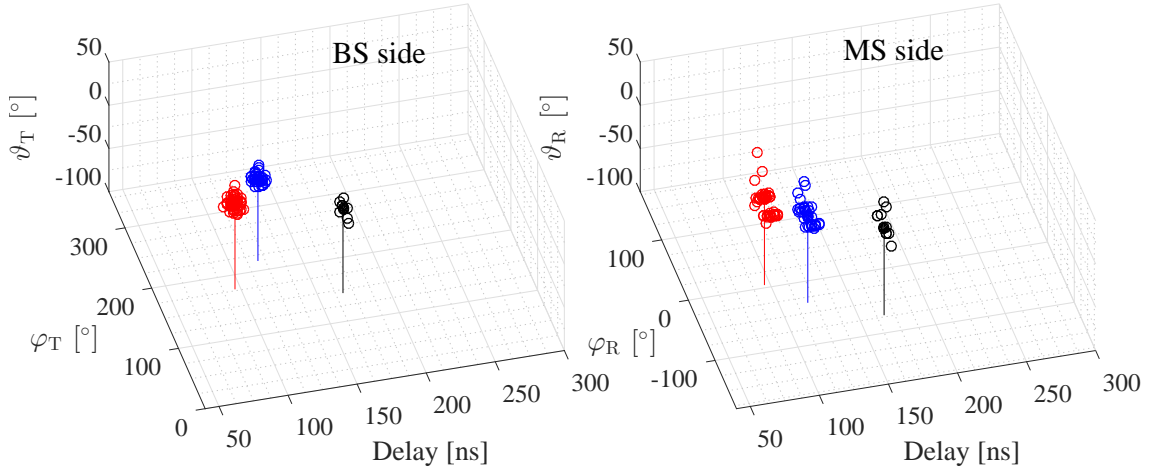
Figure 4-12: Clustered multipath components from $DDDAPS_{\text{comb}}$ at MS_3

properties of the individual clusters. Since by definition, we clump together paths with very similar properties into a cluster, therefore it is trivial to assume that these paths have the same path history (this is a terminology used in ray tracing to describe the different interactions the path has undergone). In another words we can assume that these propagation paths undergo interactions with the same object within the environment or that the interaction of the incident wave with a particular scattering object give rise to multipaths that can be grouped together into a multipath cluster. Therefore by identifying these physical structures that give rise to the clusters we can know more about the channel.

4.6 Identification of physical scattering objects corresponding to clusters

To understand more about the multipath clusters and what contributes to the formation of these clusters, we need to identify the corresponding physical scattering objects.In many literature the scattering objects are also call an interacting object (IO) [61]. A convenient way to identify the scattering object is by superimposing the plot of the $APS(\mathbf{\Omega})$ function on the panorama picture of the environment. Depend-

ing on the cluster spread we can get a rough idea of the scattering object, however in order to pinpoint the scattering object we make use of the the cluster centroid, defined in Equation (3.16).

The $APS(\mathbf{\Omega_T})$ plot superimposed on the panoramic photograph of the environment taken at the BS location for all the different MS locations are shown in Figure 4-13 for co-pol cases and in Figure 4-14 for cx-pol cases.

Although the APS defined in Equation (2.23) is a discrete function, when plotting we used the *shading interp* function in MATLAB® which performs a bi-linear interpolation of the gridded data. Also, for better illustration the values (or colors in the figure) corresponding to the floor of the APS function were removed. The circles (○) in the figure mark the cluster centroid location. It is very clear from the figure that the cluster centroids can help distinctly identify the major scattering objects in the environment corresponding to the cluster. In case of clusters with MPCs that undergo more than one interaction with the environment, such as double reflection, only the first (seen from the BS side) and the last (seen from the MS side) scattering objects can be identified. Therefore, if the clusters are due to paths that undergo more than two interactions the scattering objects in between the first and the last objects can not be determined. Identification of physical scattering object will be useful in more in-depth study of the propagation mechanisms. For the BS and MS locations considered in this measurement campaign the identified scattering objects are listed in Table 4.6. The table also shows the direction of the scattering object with respect to the BS position $(\vartheta_\mathrm{T}, \varphi_\mathrm{T})$and the total length of the path that arises due to interaction with it.

In this typical urban pico-cell environment the main scattering objects were the brick building walls and the concrete pillars. Building features like the projection (outward beyond the plane of the building wall) due to balcony like step landings on each floor and weather sheds (or sun shades) above the windows are also seen to give rise to clusters. Clusters due to scattering from street furniture such as metallic street lamps are also detected. As we will see later, diffraction by the edges of the vertical metallic frames around glass panels give rise to clusters that are significant

67

Table 4.6: Identified scattering objects

Clust No.	Scattering Object	delay [ns]	$\varphi_\mathrm{T}\,[°]$	$\vartheta_\mathrm{T}\,[°]$	Path length [m]
MS_1					
MS_1(1)	LOS + Floor(brick)	103.4	177.3	-3	31.02
MS_1(2)	Wall (brick)	127.2	215.4	-5.9	38.16
MS_1(3)	Wall (brick) - Wall(brick)	175.3	144.4	-2.5	52.59
MS_2					
MS_2(1)	LOS + Floor(brick)	103.5	356.4	-3	31.05
MS_2(2)	Lamp post (Metal)	120.8	144	-11	36.24
MS_2(3)	Wall (brick)	128.6	324.5	-0.5	38.58
MS_2(4)	Wall (brick)	131.6	58	-10.4	39.48
MS_2(5)	Balcony (concrete)	177.6	312	24	53.28
MS_2(6)	Wall (concrete) + tree	202.1	4.1	-2.9	60.63
MS_3					
MS_3(1)	Pillar (concrete) + Glass panel frame (metal)	111.1	24.6	-5.6	33.33
MS_3(2)	Wall (brick)	183.3	300.2	-0.1	54.99
MS_3(3)	Weather shed (concrete)	197.5	300	11.6	59.25
MS_3(3)	wall (concrete) - wall (brick)	264.4	96.1	0.2	79.32

under O-LOS condition (MS_ 3).

4.6.1 Identification of the Major propagation mechanism in each cluster

Using the direction $(\mathbf{\Omega}_\mathrm{R}, \mathbf{\Omega}_\mathrm{T})$ and delay (or equivalently the path length) information of the cluster centroid, it can be traced in the 3-D environment between the BS and the MS; such a technique for tracing the measured paths in the environment is called measurement based ray tracing (MBRT) [91]. For identifying the major propagation mechanisms in the cluster, we compare the MBRT results with the paths from the 3D ray tracing (RT) simulation carried out using the model of the same environment and for the same BS and MS locations. The 3D environment was modeled using the Sketchup®2015, 3-D modeling software[92]. The dimensions of the building and scattering objects such as the lamp post, weather shed, windows, pillars etc. were measured using a commercially available portable laser distance measuring tool that has an accuracy of ±1.5 mm. The outline of the modeled environment is shown in

Fig. 4-1 and the 3-D model is shown in Fig. 4-15.

We used the Raplab ver.5.0, radio wave propagation analysis tool for the 3D RT simulations [93]. From the propagation history of the RT paths that closely matched the trace of the cluster centroids we could determine the major propagation mechanism of the MPCs in the cluster. We verified that for all the cluster centroid that closely matched with the RT paths, the propagation mechanism determined was realistic by carefully examining the the geometry of the identified scattering object. The trace of those clusters centroids that did not match with any RT simulation paths were found to be mainly due to scattering from objects with complex geometry. Such objects include metallic pole (cylinder), and other objects like weather sheds and balcony, with many edges and only small uniform surface areas. For these clusters we assumed the propagation mechanism to be scattering. Such assumption is reasonable since RT simulators can not handle complex geometries such as cylinders, curved surfaces and for those complex scatterers modeled as collection of small plane surfaces the surfaces are not large enough to apply geometrical optic theory which is the basis for RT simulators. Some more comparison of the RT simulation and measurement for the same data set based on only the peaks of the DPS defined in Equation (2.19)) can be found in [94]. An example of the MBRT showing the trace of the cluster centroid for MS_1 and the comparison with ray-tracing results is shown in Fig. 4-16. The different clusters classified according to the major propagation mechanism is seen in Table 4.7 and Table 4.8.

It is interesting to note that under O-LOS condition, the cluster due to diffracted paths from the vertical metallic frame around the glass panel (MS_3 (1)) is only seen for $\varphi - \varphi$ polarization and not for $\vartheta - \vartheta$ polarization, indicating that ϑ polarized incident waves are highly attenuated during the interaction in a manner quite similar to a polarizer.

4.6.2 Scattering intensity and Cross-polar ration (XPR)

From Fig. 4-14 it is clear that for cx-pol cases at most only one other cluster can be seen besides the clusters containing the LOS path. Although detection of multipaths

69

Table 4.7: Major propagation mechanisms in clusters for ϑ-pol transmission

Propagation Mechanism	Cluster	Cluster Gain (dB)		XPR (dB)	Excess Cluster Gain (dB)		Average Excess Gain (dB)	
		$\vartheta - \vartheta$	$\varphi - \vartheta$	ϑ	$\vartheta - \vartheta$	$\varphi - \vartheta$	$\vartheta - \vartheta$	$\varphi - \vartheta$
LOS + Ground	MS_1 (1)	-95.3	-116.8	21.5	2.3	-19.2		
	MS_2 (1)	-96.3	-118.9	22.6	1.3	-21.3		
Reflection (Single)	MS_1 (2)	-105.9	-113.2	7.3	-8.3	-15.6	-11.5	-24.1
	MS_2 (3)	-111	NA	14	-13.4	NA		
	MS_2 (4)	-113.8	NA	11.2	-16.2	NA		
	MS_3 (2)	-106.2	NA	18.8	-8	NA		
Reflection (Double)	MS_1 (3)	-111.4	NA	13.6	-13.8	NA	-19.1	NA
	MS_3 (4)	-118.9	NA	6.1	-20.7	NA		
Diffraction	MS_3 (1)	NA	NA	NA	NA	NA	NA	NA
Scattering	MS_2 (2)	-117.5	NA	7.5	-19.9	NA	-19.8	NA
	MS_2 (5)	-118.9	NA	6.1	-21.3	NA		
	MS_3 (3)	-117	NA	8	-18.8	NA		
	MS_2 (6)	-116.8	NA	8.2	-19.2	NA		

Table 4.8: Major propagation mechanisms in clusters for φ-pol transmission

Propagation Mechanism	Cluster	Cluster Gain (dB)		XPR (dB)	Excess Cluster Gain (dB)		Average Excess Gain (dB)	
		$\varphi - \varphi$	$\vartheta - \varphi$	φ	$\varphi - \varphi$	$\vartheta - \varphi$	$\varphi - \varphi$	$\vartheta - \varphi$
LOS + Ground	MS_1 (1)	-93.8	-117.6	23.8	3.8	-20		
	MS_2 (1)	-95.5	-119.2	23.7	2.1	-21.6		
Reflection (Single)	MS_1 (2)	-113.7	-117.9	4.2	-16.1	-20.3	-17.8	-25.3
	MS_2 (3)	-120.9	NA	4.1	-23.3	NA		
	MS_2 (4)	-120.8	NA	4.2	-23.2	NA		
	MS_3 (2)	-106.9	NA	18.1	-8.7	NA		
Reflection (Double)	MS_1 (3)	-119.7	NA	5.3	-22.1	NA	-23.1	NA
	MS_3 (4)	-122.4	NA	2.6	-24.2	NA		
Diffraction	MS_3 (1)	-114.1	NA	10.9	-15.9	NA	-15.9	NA
Scattering	MS_2 (2)	-124.4	NA	0.5	-26.7	NA	-25.6	NA
	MS_2 (5)	-119.4	NA	5.6	-21.8	NA		
	MS_3 (3)	NA	NA	NA	NA	NA		
	MS_2 (6)	-121.3	NA	3.7	-23.7	NA		

and therefore clusters is dependent on the dynamic range of the system, this results can be generalized since transceivers in the practical BS and MS can not be expected to have higher dynamic range than the sounder. In order to understand more about the clusters themselves we first calculate the scattering intensity of each clusters. We define scattering intensity as the ratio of the cluster gain (or cluster power) and to the path gain (or inverse of path loss) of a path that travels the equal distance in free space. This quantity determines how much of the incident energy is lost due to scattering by the object compared to if the energy lost if the waves were traveling the same electrical distance in the free space. This quantity is a little different from reflection coefficient, in that the comparison is between the received power and the equivalent free space path gain. However this gives us a measure of how much power is lost when compared to traveling in the free space and is easily obtained from the measurement. Similar to excess delay, the excess cluster gain is defined as the ration of the cluster power to the ration of the cluster with the maximum power for the same MSBS combination. These parameters will be useful in designing the antenna.

Another very important parameter of the channel is the cross-polar ration (XPR) defined as

$$\text{XPR(dB)}_q = 10\log_{10}\frac{P_{qq}}{P_{pq}} \tag{4.1}$$

where, P_{qq} is the power of the q polarized electic field component received and P_{pq} is the power of the q polarized electric field component received when a q polarized field is transmitted. Therefore in our case, where we are dealing with two linear polarizations we can have two XPR values, XPR_ϑ and XPR_φ. However in literature it is usual to consider the two to be equal and therefore represent XPR as a single value mainly for convenience.

Table 4.7 shows major propagation mechanism of the cluster, the cluster gain, excess cluster gain and the XPR(dB)_ϑ for the ϑ polarized transmission. Similarly, the major propagation mechanism and other parameters are shown in Table 4.8. The clusters that were not detected are indicated as NA. For the purpose of calculating the XPR, if the cluster is not detected under corresponding cx-pol configuration, the

noise level, $-125\,\text{dB}$ was assumed as the power of the un-detected cluster. Although in reality we don't know the exact level of the cluster gain once it is below the noise floor, for actual systems where the dynamic range would be much lower than the sounding system, the XPR calculated as such should suffice. For these cases the XPR value should be preceded by the ,$\geq$, sign to make it mathematically correct. Similar assumption is made for calculating the average excess gain when the cluster is not detected in the corresponding orthogonal polarization.

Observing the tables, excluding the clusters containing the LOS path, the highest scattering intensity for cluster in $\vartheta - \vartheta$ polarization ranged from -3.6 dB to -18.5 dB. For $\varphi - \varphi$ polarization the scattering intensities of the clusters ranged between -4.3 dB to -25.4 dB. On average under $\vartheta - \vartheta$ polarization the scattering intensities decreased in descending order for clusters of single reflection, double reflection, and clusters due to scattering, with average scattering intensities of -11.4 dB, -17.2 dB,-19.8 dB respectively. The clusters due to diffraction were detected under O-LOS condition for $\varphi - \varphi$ polarization only. For $\varphi - \varphi$ polarization combination the average scattering intensities in descending order were -15 dB,-15.8 dB,-17 dB,and -20.1 dB for clusters due to single reflection, diffraction, double reflection and scattering respectively. Although comparison between the scattering intensity of different clusters are inherently unfair given that scattering intensity is highly dependent of the angle of incidence, the material and geometry of the scattering objects, we can however fairly compare the scattering intensity of the same cluster for the different polarization combinations. Interestingly we find that the scattering intensity is higher for all clusters under $\vartheta - \vartheta$ polarization compared to $\varphi - \varphi$ polarization,except for clusters containing the LOS path and the cluster due to diffraction. On average the scattering intensity of clusters due to single reflection, double reflection and scattering are stronger by 6.1 dB, 5.6 dB and 4.5 dB for $\vartheta - \vartheta$ polarization compared to $\varphi - \varphi$ polarization.

Excess delay and Excess gain of clusters are important parameters in channel modeling. Here excess delay and excess gains are defined as the difference of the cluster delay and the cluster gain (in dB) from the delay and the path gain of the

LOS path (in dB) respectively. Table **??** also show the excess gain and the delay of each clusters. The maximum excess delay of the clusters in O-LOS case is 154 ns and for LOS case is 100 ns. In cx-pol cases the maximum excess delay of the clusters were < 25 ns. Clusters with excess gains ranging from -8 dB to -21.3 dB in $\vartheta - \vartheta$ polarization, and ranging from -8.8 dB to -26.8 dB in $\varphi - \varphi$ polarization are seen. In terms of average excess gain for clusters beside the cluster containing the LOS path, the single reflection clusters and double reflection cluster are dominant for $\vartheta - \vartheta$ polarization. For $\varphi - \varphi$ polarization the single reflection and diffraction clusters are dominant. Some more discussion on the excess cluster gain can be found in our earlier work [95] and in [**?**] based on peaks of the DPS.

4.6.3   Intra Cluster delay and angular dispersion properties

In the previous section we analyzed the overall delay and the angular spread at a particular receiver position. However if we note from Tables 4.2,4.3,4.4 and 4.5 we see that the spread values are very dependent on the number of clusters that are detected. Following the discussion in section

Similar to how we determined the overall delay and the angular spread values at a particular MS location, we can apply the same definition of the delay dispersion and angular dispersion but this time limiting the angular and delay range to that of only a single cluster. Therefore the cluster the angular spread and the delay spread of the lth cluster about its centroid is can be estimated similar to [88] as

$$\sigma_{\xi_l} = \sqrt{\frac{\sum_{k=1}^{K}(\xi_{kl} - \bar{\xi}_l)^2 P_k}{\sum_{k=1}^{K} P_{kl}}}, \tag{4.2}$$

where,ξ can be any of the $n(\text{delay}),\vartheta_{\text{R}}, \varphi_{\text{R}}, \vartheta_{\text{T}}, \varphi_{\text{T}}$.

Although we weight the angles (AoD and AoA) with the power in determining the angular spread in Eq. (4.2), because of the limited spatial domain resolution of the system and also the limitations of the CLEAN algorithm, a single path could result in angular spread values larger than zero. To statically interpret the determined angular values we perform a null hypothesis testing, where the null-hypothesis being that the

spread is not caused by a single path. This is described in [2]. The angular spread values for which we can not reject the null hypothesis with confidence level of 98.0% are indicated in the table by the inequality ($\leq$), since we can not determine if this spread is really due to MPCs or if it is due to a single path (which should actually be 0). Similar to discussion on scattering intensity in the previous section, here also we classify the clusters based on their propagation mechanisms and focus only on the co-pol cases. Table 4.9 shows the delay spread and the angular spread values for $\vartheta - \vartheta$ polarization and $\varphi - \varphi$ polarization respectively.

The rms delay spread of the clusters are very small (< 2.3 ns) and comparable to delay resolution of 2.5 ns of the system, for both the polarization cases.

From Table.4.9 we see that for $\vartheta - \vartheta$ polarization, on the AoD side (at the BS) the clusters ranges from being very specular in nature ($\approx 0°$ spread) to having azimuth spread of up to 5.7° and 6.5° elevation spread. Similarly, for $\varphi - \varphi$ polarization on the AoD side, azimuth spread of up to 7° and elevation spread of up to 8.5° can be seen. On average the clusters in $\vartheta - \vartheta$ polarization is seen to have azimuth spreads of $\leq 3.3°$, and elevation spread of $\leq 3.2°$ elevation spread. For $\varphi - \varphi$ polarization, average azimuth spread and elevation spread of $\leq 4.3°$ and $\leq 3.8°$ respectively are seen. From the average AoD angular spread in the table, for clusters due to single reflection, double reflection and scattering both the average azimuth spread and the elevation spreads are in most cases slightly higher in $\varphi - \varphi$ polarization compared to $\vartheta - \vartheta$ polarization. However, unlike scattering intensity this is not true for individual clusters.

Focusing on the AoA side (at the MS) it is at once clear from the table that in all the clusters, the AoA azimuth spread is a lot higher compared to the AoD azimuth spread for both the polarization combinations. The maximum AoA azimuth spread is 15° in $\vartheta - \vartheta$ polarization and 14.8° in $\varphi - \varphi$ polarization. On average the AoA azimuth spread and AoA elevation spread for $\vartheta - \vartheta$ polarization are $\leq 10.6°$ and $\leq 5.2°$ respectively. For $\varphi - \varphi$ polarization the average AoA side azimuth spread is $\leq 8.6°$ and the elevation spread is $\leq 5.2°$. Although the average AoA elevation spread is much lower compared to the AoA azimuth spread, a maximum elevation

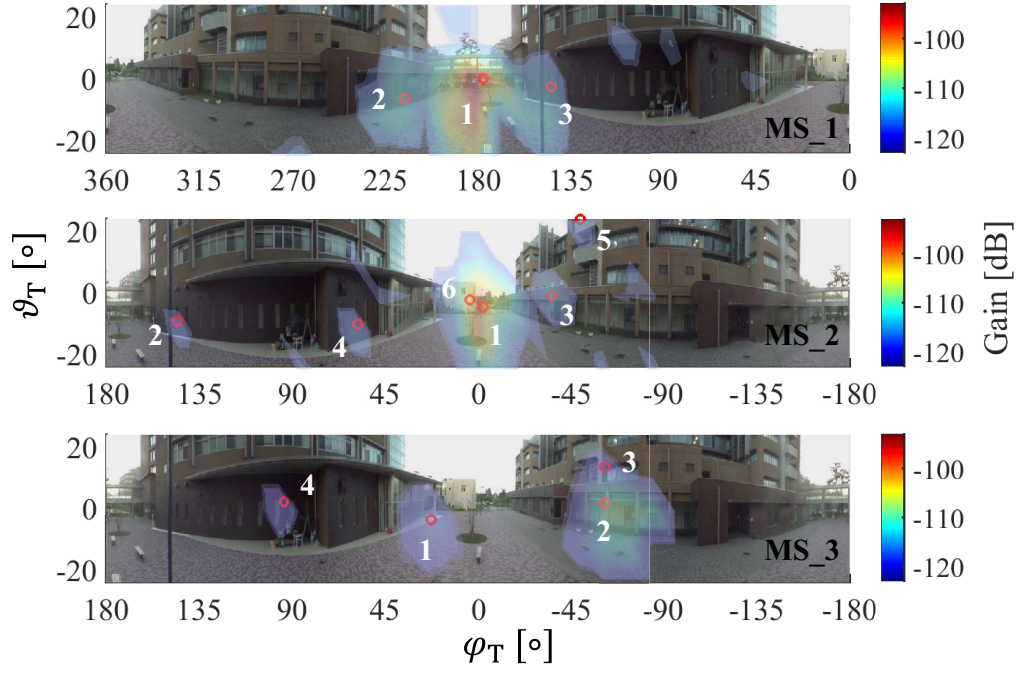Figure 4-13: Angular power spectrum $APS(\Omega_T)$ at different MS locations for co-pol case (○ indicates the location of cluster centroid and the scattering object). *Copyright* © 2017 IEICE [2].
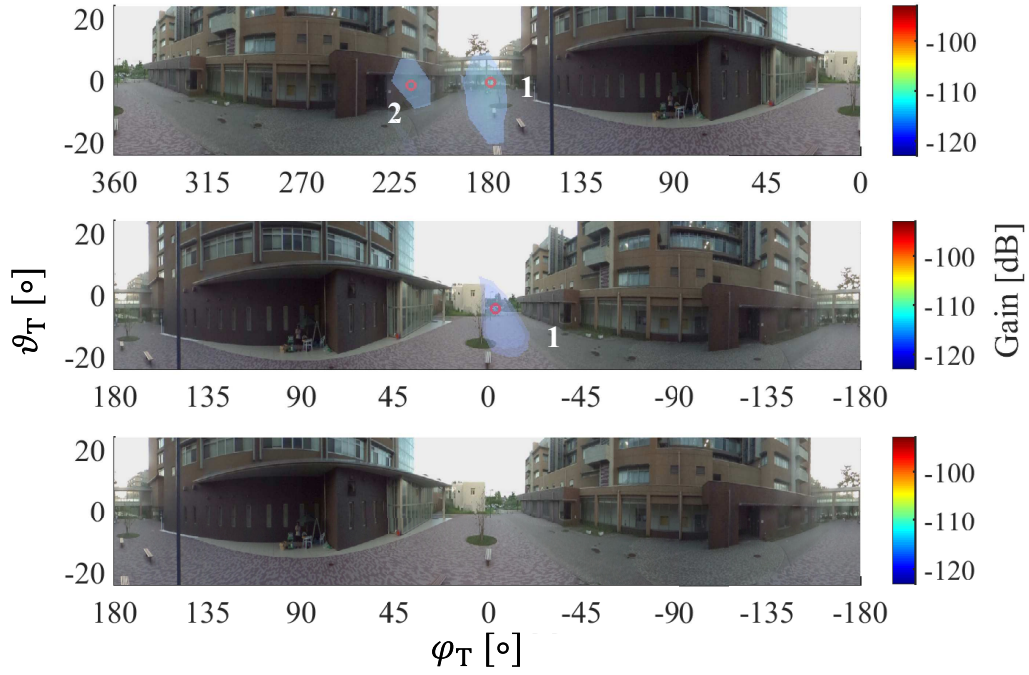
Figure 4-14: Angular power spectrum $APS(\Omega_T)$ at different MS locations for cx-pol case (○ indicates the location of cluster centroid and the scattering object). *Copyright* © 2017 IEICE [2].

Figure 4-15: 3D model of the outdoor environment, modeled using using Sketchup®.
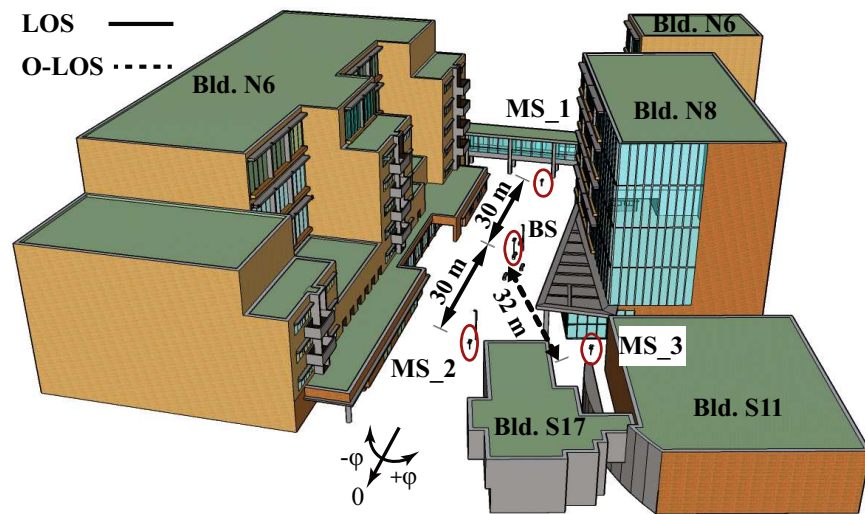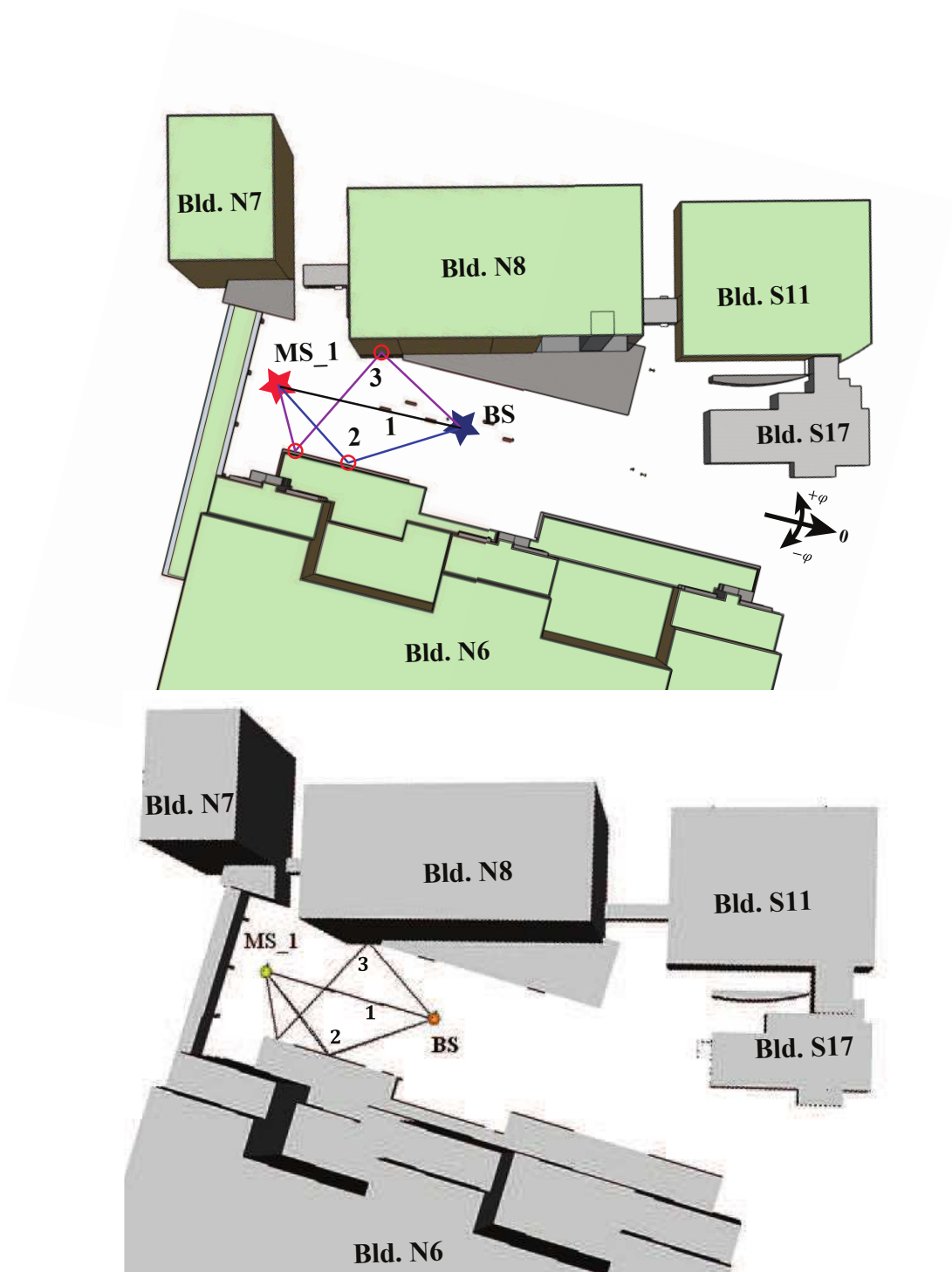*Copyright* © 2017 IEICE [2].

Figure 4-16: (Top) Measurement based ray tracing of cluster centroids between BS and MS_1 (Bottom) 3D ray tracing results showing the strongest paths between BS and MS_1. *Copyright* © 2017 IEICE [2].

Table 4.9: Co-pol case cluster delay spread and angular spread (at 98% confidence level)
(Azimuth spread (σ_φ), Elevation spread (σ_ϑ)

Propagation Mechanism	Cluster	$\vartheta - \vartheta$ Polarization			$\varphi - \varphi$ Polarization		
		AoD angular spread (°)	AoA angular spread (°)	Delay spread (ns)	AoD angular spread (°)	AoA angular spread (°)	Delay spread (ns)
LOS + Ground	MS_1 (1)	[4.2, 2.2]	[≤9.4, ≤1.6]	2	[4.7, 5,9]	[≤4.7, ≤2.1]	2.3
	MS_2 (1)	[4.2, 4.7]	[≤3.6, ≤8.9]	1.8	[3.1, 2.9]	[≤8.2, ≤5.8]	1.7
Reflection (single)	MS_1 (2)	[5.2, 6.5]	[14.9, 6.2]	1.9	[3.6, ≤0.9]	[13.7, ≤7.0]	1.4
	MS_2 (3)	[2.5, 2.5]	[≤6.2, ≤1.6]	1.7	[5.0, 6.0]	[12.6, ≤4.6]	1.7
	MS_2 (4)	[4.4, 4,4]	[11.1, ≤8.1]	1.5	[2.3, ≤0.7]	[≤2.6, 14.0]	1.2
	MS_3 (2)	[2.4, ≤0.1]	[11.2, ≤2.7]	1.7	[5.9, 5.9]	[≤5.9, ≤3.7]	1.8
Reflection (double)	MS_1(3)	[5.4, 5.7]	[13.2, 2.6]	0.6	[4.5, 4.5]	[≤8.2, ≤3.3]	0.9
	MS_3 (4)	[2.0, ≤0.6]	[13.3, ≤2.5]	1.3	[7.0, 2.5]	[≤8.1, ≤2.6]	1.2
Diffraction	MS_3 (1)	NA	NA	NA	[5.8, 6.0]	[14.7, ≤4.6]	1.6
Scattering	MS_2 (2)	[≤0.7, 3.4]	[≤1.8, ≤9.1]	1.2	[≤1.6, ≤1.1]	[≤7.6, ≤3.3]	1.3
	MS_2 (5)	[≤0.8, ≤0.6]	[15.0, ≤4.0]	0.9	[≤1.9, ≤0.6]	[14.8, 17.2]	0.7
	MS_3 (3)	[≤0.7, 2.2]	[12.3, 13.6]	1	NA	NA	NA
	MS_2 (6)	[5.7, 5.2]	[15.0, ≤1.5]	1.9	[6.0, 8.5]	[≤2.8, ≤2.5]	2.1

Table 4.10: Cx-pol case cluster delay spread and angular spread (at 98% confidence level)
(Azimuth spread (σ_φ), Elevation spread (σ_ϑ)

Propagation Mechanism	Cluster	$\vartheta - \varphi$ Polarization			$\varphi - \vartheta$ Polarization		
		AoD angular spread (°)	AoA angular spread (°)	Delay spread (ns)	AoD angular spread (°)	AoA angular spread (°)	Delay spread (ns)
LOS + Ground	$MS_1(1)$	[0.7, 5.4]	[14.9, 11.2]	1.7	[4.7, 3.2]	[9.6, 30.2]	2.1
	$MS_2(1)$	[5.6, 5.3]	[17.8, 13.6]	1.2	[5.2, 5.1]	[16.5, 7.1]	1.7
Reflection (single)	$MS_1(2)$ $MS_2(3)$ $MS_2(4)$ $MS_3(2)$	[0.7, 3.75]	[1.9, 27.9]	1.1	[5.9, 4.5]	[14.9, 27.9]	1.4
Reflection (double)	$MS_1(3)$ $MS_3(4)$						
Diffraction	$MS_3(1)$			NA			
Scattering	$MS_2(2)$ $MS_2(5)$ $MS_3(3)$ $MS_2(6)$						

spread of 13.6° and 17.2° is seen in $\vartheta - \vartheta$ and $\varphi - \varphi$ polarizations respectively. The relatively larger angular spread on the MS side and the relatively smaller spread on the BS side might be desirable in practice. Unlike the case of scattering intensity, the angular spread does not show dependence on polarization. The intra-cluster parameters classified based on the polarization and the propagation mechanisms, are are summarized in Figures 4-17, 4-18, 4-19.

4.7 Summary

In this chapter we conducted a detailed analysis of the delay dispersion and angular dispersion characteristics of the millimeter wave propagation channel in an outdoor pico cell environment for different polarization combinations. Such characterization are useful since there are very limited measurement based analysis of double directional millimeter wave channel. In most of the studies the angular spread analysis is limited to just the azimuth domain and to either the MS or the BS side. The parameters derived are even more useful due to the polarization information. Such parameters are rarely studied and presented in literature due to the extensive effort required for 3-D double directional measurement.

Comparing the delay spread of the different polarized channel it is found that in co polarized case the dispersion is much larger with rms values ranging from 7.4 ns to 25.7 ns. Under cross polarization the dispersion in delay domain is even small to the point of being specular in nature. Of the two co-polarization cases the $\vartheta - \vartheta$ configuration shows larger spread. This is owing to the $-$ clusters being relatively stronger compared to other configurations. The channel is very sparse in terms of the clusters. Meaning there are only few clusters other than the LOS cluster. The effect of this is that the delay and the angular dispersion are very much dependent on if a cluster is visible or not to a receiver; the dispersion would show huge swing depending on the visibility.
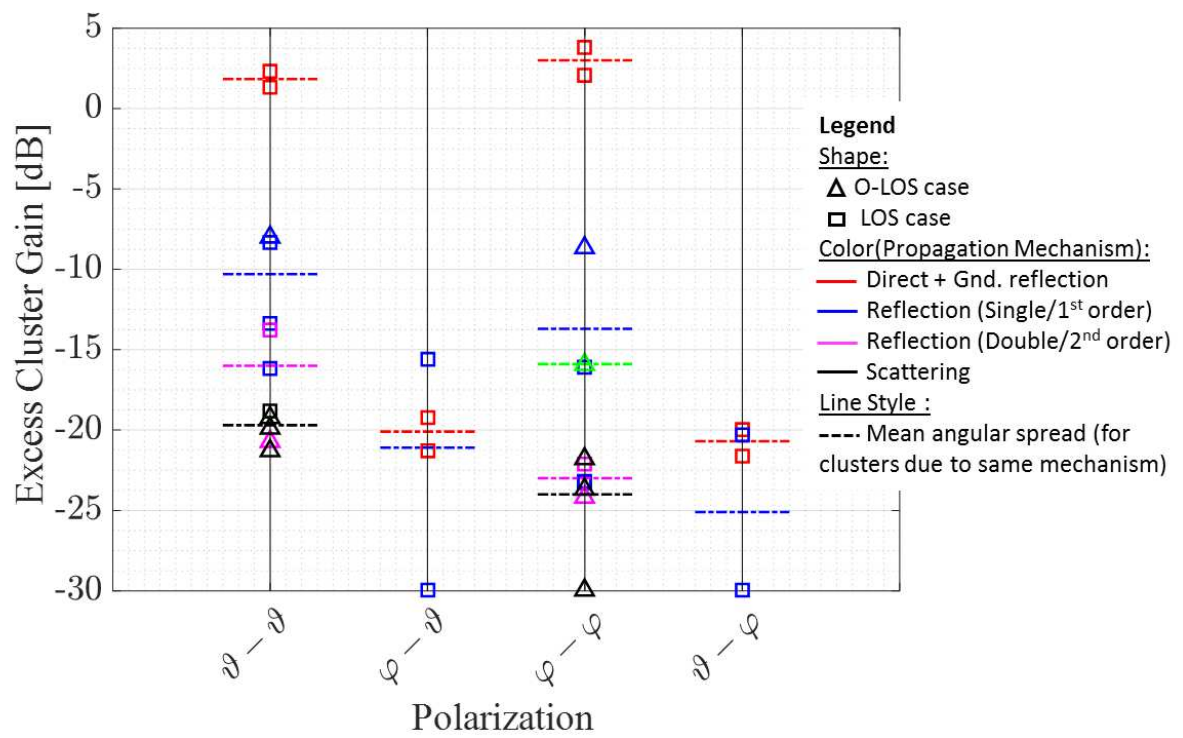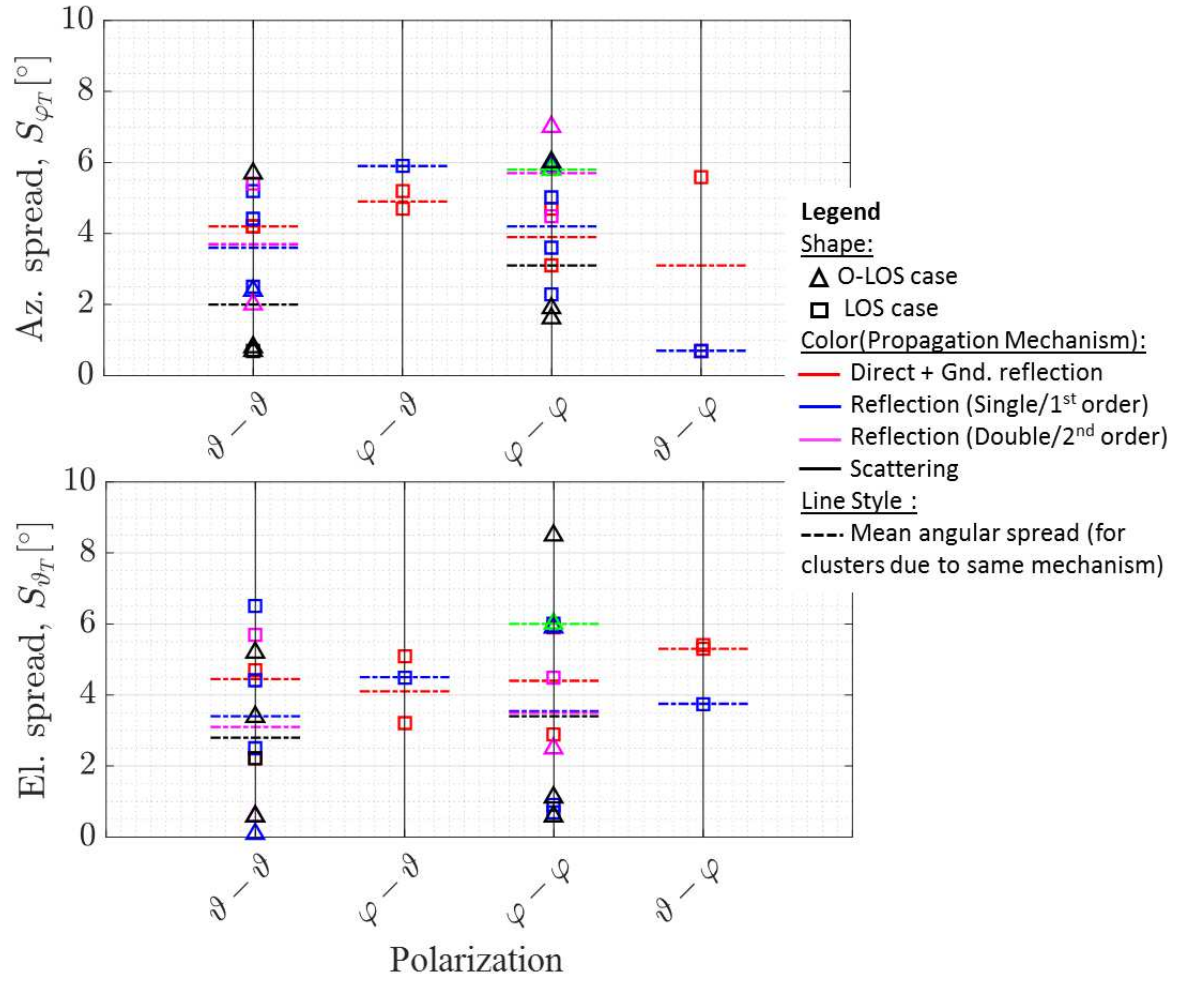
Figure 4-17: Excess gain of clusters
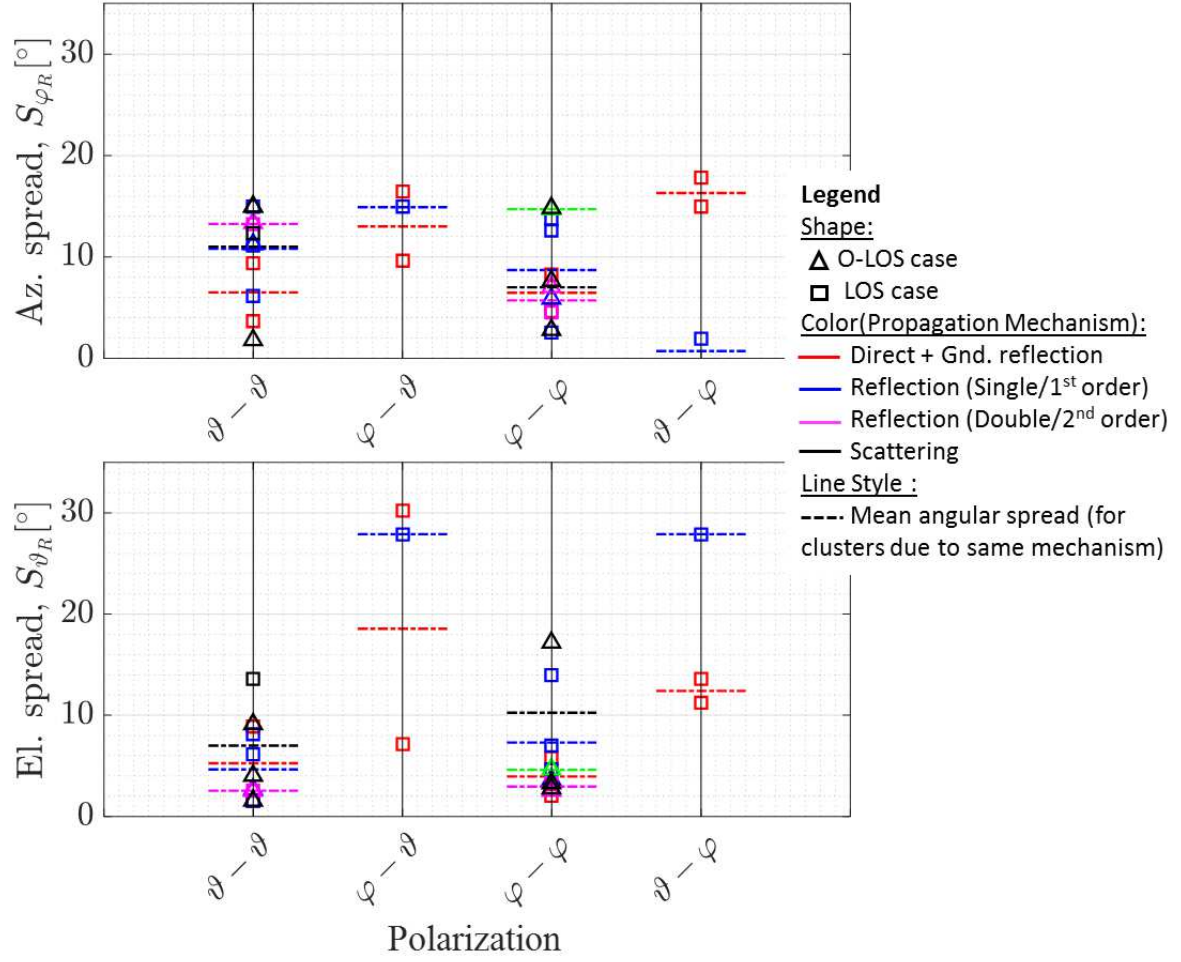
Figure 4-18: Angular spread at the BS side

Figure 4-19: Angular spread at the MS side

5 Millimeter Wave Propagation in Indoor Environment

Another environment for deployment of millimeter wave networks is the indoor environment; such as conference room, shopping malls, meeting rooms etc.[54]. Therefore knowing how the channel behave in such indoor environment will useful for development of the millimeter wave system and deployment. There is huge interest in millimeter indoor environment owing to the IEEE802.15.6, IEEE802.11.ay standards.

5.1 Indoor Measurement Campaign

A measurement campaign was carried out in a typical laboratory environment with room dimension of $5.8 \times 6.6 \times 2.7 \, \text{m}^3$. The transmitter antennas are located at the corner of the room, at BS, and is mounted at $2.5 \, \text{m}$, just below the ceiling height of $2.7 \, \text{m}$. The receivers are located at two positions, MS_1, MS_2 at a height of $1.5 \, \text{m}$. The dimensions and the location of the BS and MS are show in Figure 5-1. The room had prominent (or large) indoor fixtures like wooden tables, metal shelves (or racks), air conditioner etc. The objects within the environment are clearly visible in the panorama picture taken from MS_1 and MS_2 in Figure 5-2. There were also a few non prominent (relatively small) fixtures like test equipment, few cardboard boxes and computers on and under the wooden tables.

5.1.1 System and measurement settings

Two $24 \, \text{dBi}$ $12°$ half power beam width (HPBW) pyramid horn antennas with orthogonal polarization and mounted diametrically opposite to each other are used on the
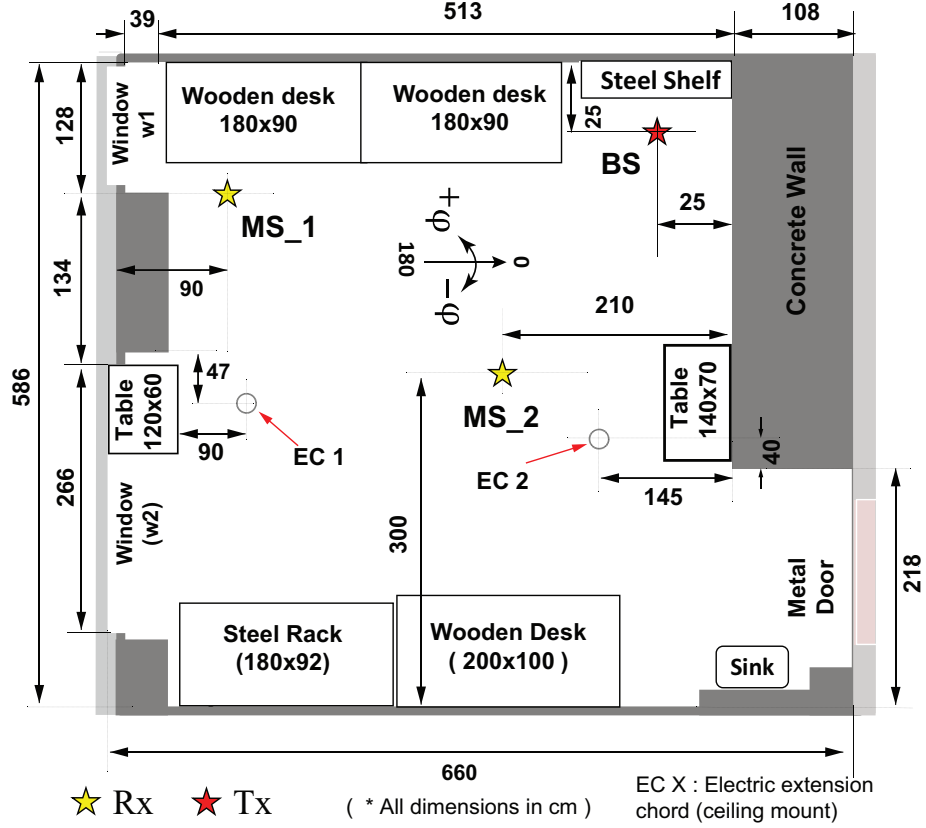
Figure 5-1: Layout of the indoor environment

receiver side. On the transmitter side two 15 dBi, 30° HPBW pyramid horn anten-
nas with orthogonal polarization and mounted diametrically opposite to each other
is used at the transmitter side. The antenna azimuth angles (φ) are defined based
on the coordinate shown on the left of figure. The elevation angle, ϑ, corresponds to
the global vertical axis, meaning the elevation angle is equal to 0, when the antenna
is parallel to the ground. The MS side antennas are scanned in steps of 5° both in
elevation and azimuth plane. A full 360° sweep is carried out in the azimuth plane.
In elevation plane the scanning angle range is from $-35° \sim 35°$. On the Tx side,
since the antennas are very near to the wall, in the azimuth plane the scanning angles
ranged from $270° \sim 360°$ in steps of 15°. In the elevation plane the antenna scanning
angles ranged from $0° \sim -45°$ in steps of 15°. The details of the system parameters
and measurement settings are detailed in Table 5.1. The sounding system, set up for
this measurement is shown in Figure 5-3.

86
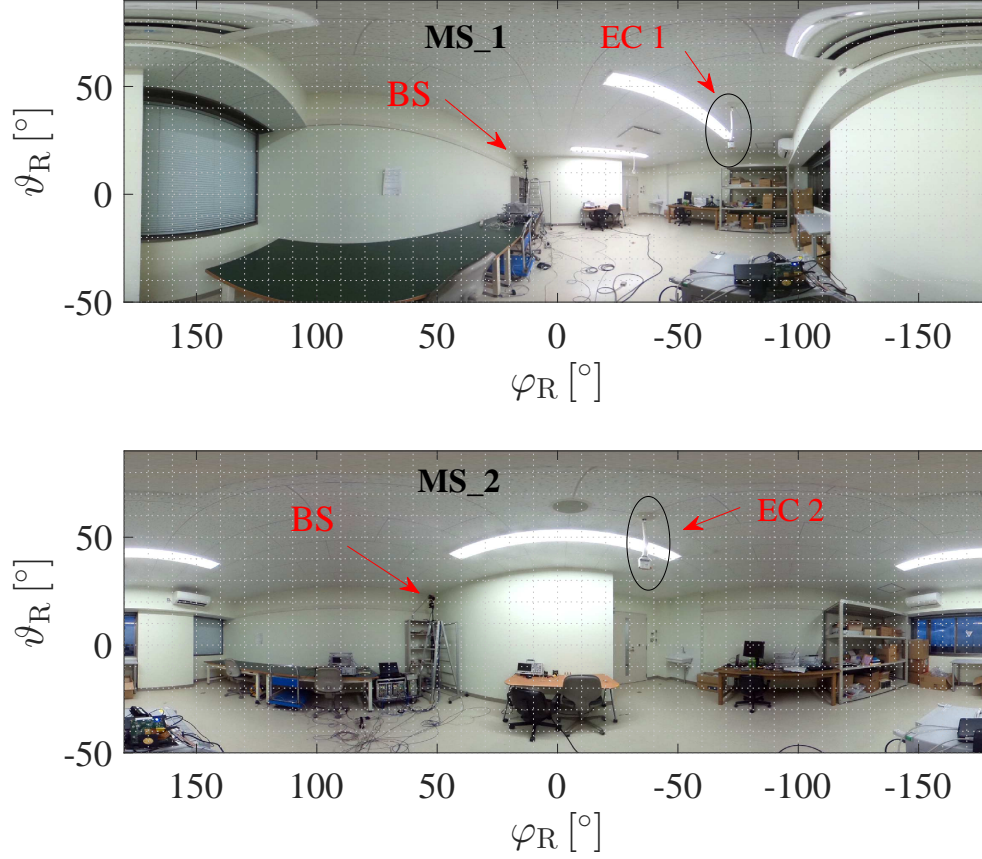
Figure 5-2: Panorama view from the MS locations

5.2 Measurement analysis

Similar to the data processing in the outdoor measurement scenario, from the transfer function (TF) obtained from the channel sounder we use inverse discrete Fourier transform (IDFT) to get the channel impulse response (IR). Using the double directional measured channel impuse response, we deconvolve the antenna responses from both the Rx and the Tx side to obtain a cleaned double directional channel impulse response, using the CLEAN algorithm. From this we again synthesize the $DDDPS(\mathbf{\Omega}_\mathrm{T}, \mathbf{\Omega}_\mathrm{R}, \tau)$. Similar to the outdoor case once we have this we can then proceed to look into the different parameters of the indoor channel.
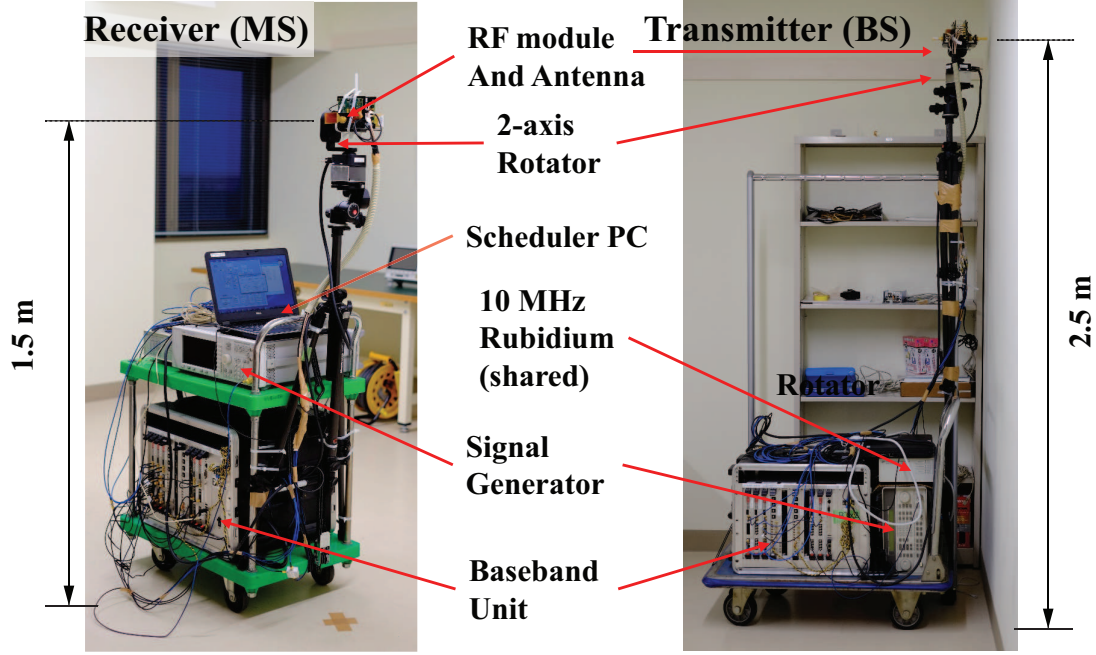
Figure 5-3: The channel sounding system set up in the indoor environment

Table 5.1: Sounding parameters and measurement settings for indoor measurement campaign

Frequency (f_c)	58.5 GHz
Signal bandwidth	400 MHz
Sampling frequency (f_s)	800 MHz
No. of sub-carriers (tones) (N)	256
TDM symbol length (N_{sym})	1024
TDM symbol duration (T)	1.28 μs
Tone spacing (Δ_F)	1.563 MHz
Maximum delay	640 ns
Delay resolution	2.5 ns
Tx Power (P)	0 dBm
Tx antenna height (BS)	2.5 m
Rx antenna height (MS)	1.5 m
Tx antenna	Pyramid Horn , 15 dBi, 30° HPBW
Rx antenna	Pyramid Horn , 24 dBi, 12° HPBW
Tx - Rx antenna XPD	36 dB (measured; when fully aligned)
$[\vartheta_{\mathrm{T}}, \varphi_{\mathrm{T}}]$	$[0° \sim -60°, 270° \sim 360°]$
$[\vartheta_{\mathrm{R}}, \varphi_{\mathrm{R}}]$	$[-35° \sim 35°, \; 0° \sim 348°]$

5.2.1 Delay power spectrum and delay dispersion

The $DPS(\tau)$ for the receiver is at MS_1 and MS_2 are shown in Figure 5-4 and Figure 5-5 respectively. Observing the figures we can see that the DPS is characterized by few peaks, separated in the delay domain. MS_1 is very close to the wall and therefore the second peak is very close to the highest peak, both in terms of the delay and power. MS_2 is located in the middle of the room and therefore the next highest peak arrives after much longer delay compared to at MS_1. The delay dispersion parameters are shown in Table 5.2. The cross polarization configuration shows significantly lower delay spread and excess delay. The indoor delay spread values are also significantly lower than those found in the outdoor environment, Table 4.2 this is mainly owing to the fact that the scattering objects are much closer to the receiver. The maximum excess delay spread value of 37.5 ns for instance corresponds to 11.25 m in terms of electrical distance, this is comparable to the room dimension.

Table 5.2: Rms delay spread in Indoor environment

Polarization		LOS					
		MS_1			MS_2		
		$\tau_m(\text{ns})$	$\tau_{rms}(\text{ns})$	$\tau_{excess}(\text{ns})$	$\tau_m(\text{ns})$	$\tau_{rms}(\text{ns})$	$\tau_{excess}(\text{ns})$
co pol	$\vartheta - \vartheta$	13	4.1	30	15.9	8.6	37.5
	$\varphi - \varphi$	12.9	4.2	37.5	14.8	7.1	37.5
cx pol	$\varphi - \vartheta$	11.9	2.4	5	13.4	5	17.5
	$\vartheta - \varphi$	11.8	2.4	5	14.1	4	17.5

5.2.2 Clusters in indoor environment

Again, like in the case of the outdoor environment we can use the $DDDPS(\mathbf{\Omega}_{\text{R}}, \mathbf{\Omega}_{\text{T}}, \tau)$ and to extract multipath components which are then clustered using the KPower-Means algorithm. The detected clusters for all the MS locations are given in Table 5.3. Using the $APS(\mathbf{\Omega}_{\text{R}})$ plots and the cluster centroid we can then identify the scattering objects corresponding to the detected cluster. For both copol case and cx-pol case the receiver side APS at MS_1 is shown in Figure 5-7 and Figure 5-6.
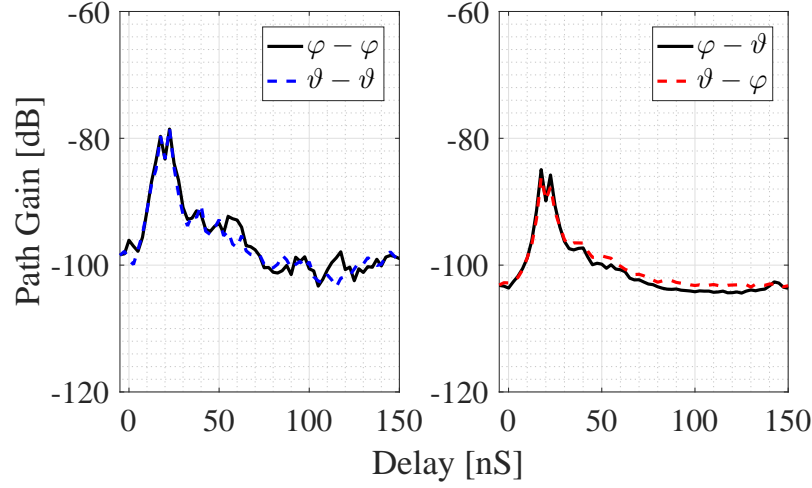
Figure 5-4: DPS at MS_1 view from the MS locations
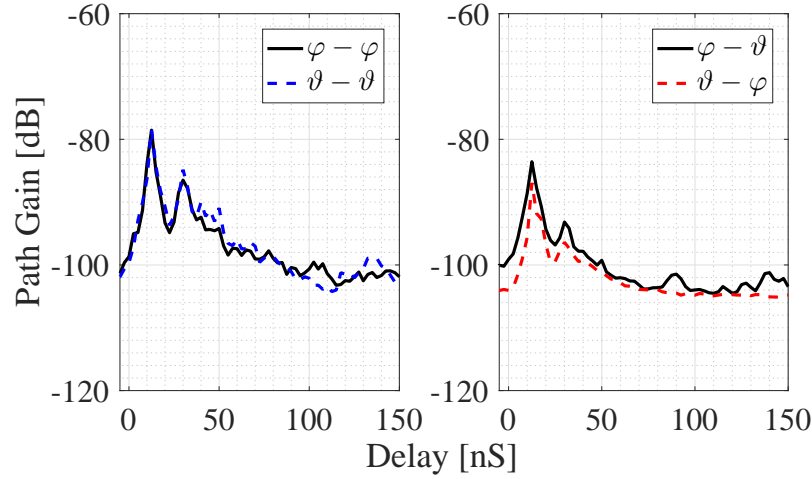
Figure 5-5: DPS at MS_2

In case of MS_1 both $\vartheta - \vartheta$ and $\varphi - \varphi$ cases contained the same detected clusters. However in the cross polarization case, only the cluster corresponding to the LOS and the clusters corresponding to scattering from the window blind (MS_1(2)) were seen. The cluster, MS_1(3) could not be detected.

Similarly, the APS at MS_2 for $\varphi - \varphi$ polarization is shown in Figure 5-9 and for $\vartheta - \vartheta$ polarization is shown in Figure 5-8. Unlike in MS_1, here even under co-polarization case there exist few differences as to the clusters detected. Under $-\vartheta$ polarization the multi-path cluster due to the the ceiling mounted power extension chord (EC2 in Figure 5-2) is too weak to be seen. However under $\varphi - \varphi$ polarization this can

be clearly seen and is comparable in strength to the other clusters. Interestingly this cluster is also visible under $\varphi - \vartheta$ polarization. This indicates that thin vertical structures (in this case, a coiled cable with coil diameter of $30\,\mathrm{mm}$ and cable diameter of $10\,\mathrm{mm}$) can act like a filter and only allow the electric field component that is propagating in transverse direction relative to its geometry.
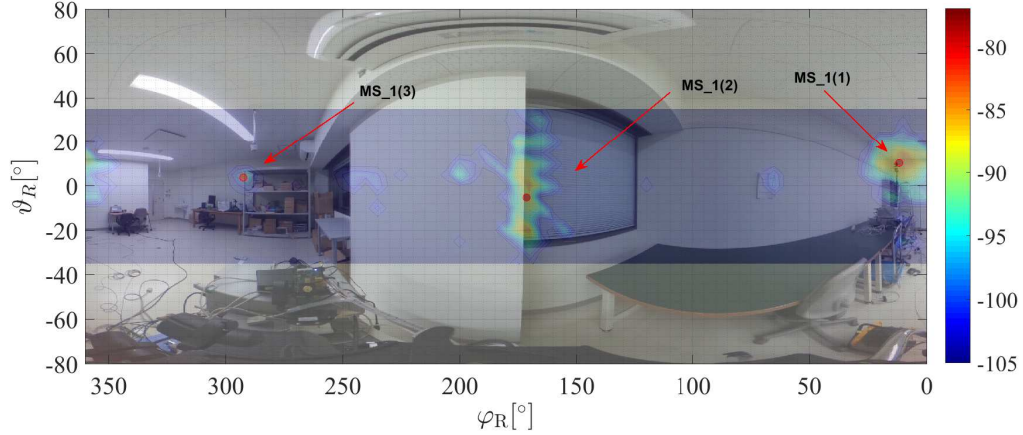
Figure 5-6: The copol $APS(\mathbf{\Omega}_{\mathrm{R}})$ at MS_1
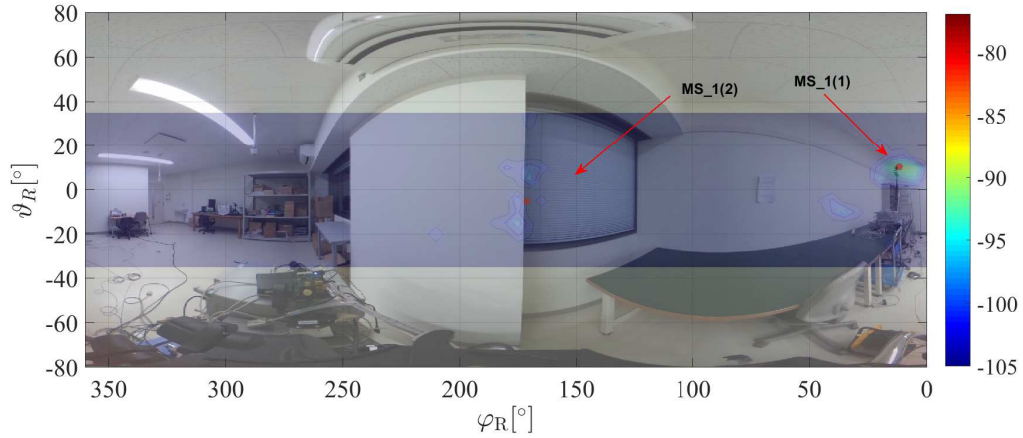
Figure 5-7: The cxpol $APS(\mathbf{\Omega}_{\mathrm{R}})$ at MS_1

The list of all the detected clusters and the corresponding scattering object is shown in Table 5.3. However as already discussed, under cx-pol configuration only the the LOS and at most another cluster was visible. Similar to in the outdoor environment case, from the cluster results we can identify the major propagation mechanisms and determined the XPR and the scattering intensity of the clusters.

Table 5.3: Clusters detected in Indoor environment and the identified scattering object

Clust No.	Scattering Object	delay [ns]	distance [m]	$\varphi_R[°]$	$\vartheta_R[°]$
MS_1					
MS_1(1)	LOS + Wall (concrete)	17.5	5.25	10.8	10.2
MS_1(2)	Wall(concrete) + blinds (metal)	20.03	6.009	171.6	-5.
MS_1(3)	Wall(concrete) + Shelf(Metal)	36.3	10.89	291.2	3.3
MS_2					
MS_2(1)	LOS + Wall (concrete)	12.5	3.75	54	17
MS_2(2)	wall (concrete) -wall(concrete)	50	15	82	5
MS_2(3)	Wall (concrete)	32	9.6	160	6
MS_2(4)	Window (metal + glass)	45	13.5	205	4.5
MS_2(5)	Shelf (Metal)	34	10.2	256	5
MS_2(6)	Wall (concrete)	32	9.6	277	5
MS_2(7)	Extension chord (plastic)	14	4.2	180	25

Table 5.4: Major propagation mechanism of detected clusters, $[\vartheta - \vartheta, \varphi - \varphi]$

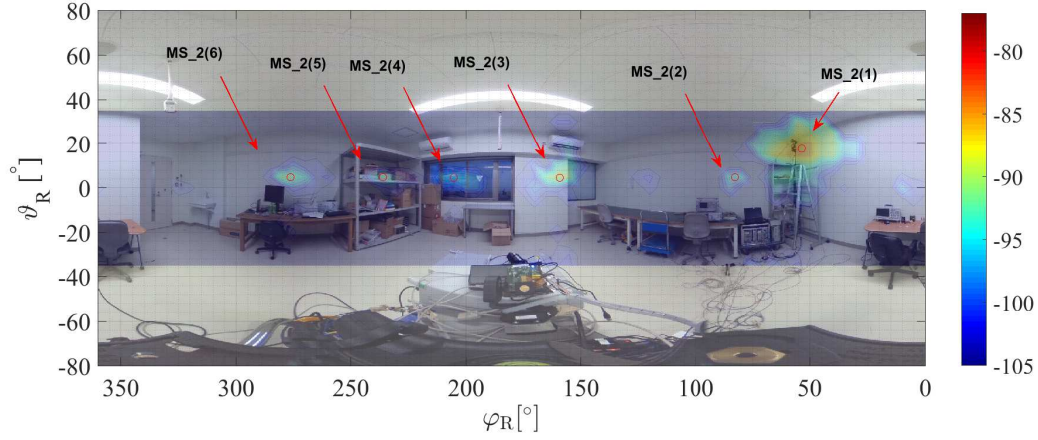| Propagation Mechanism	Cluster	Cluster Gain (dB)	Excess Cluster Gain (dB)	Average Excess Gain (dB)	XPR (dB)
LOS + Wall	$MS_1(1)$	[-82.3, -83.2]	[-1 ,-1.6]		[9.7 , 21.8]
	$MS_2(1)$	[-79.7, -77]	[-0.7, 2]		[9,3, 15]
Reflection (Single)	$MS_2(3)$	[-85.7,-85]	[-6.7 -6]	[-11.3, -7.5]	[19,3, 20]
	$MS_2(6)$	[-95.5, -90.1]	[-16, -11]		[9.5, 14.9]
Reflection (Double)	$MS_2(2)$	[-97.6, -93.8]	[-18, -14]	[-19.1, NA]	[7.4, 11.2]
Diffraction	$MS_1(3)$	[-102.0, -96.9]	[-20, -14.6]	[-20 ,-13.3]	[3, 9]
	$MS_2(5)$	[NA -91.4]	[NA , -12]		[NA, 13.6]
Scattering	$MS_1(2)$	[-80.3, -80]	[-1.04, - 1.4]	[-8.7 , -6.6]	[14, 11]
	$MS_2(4)$	[-93.5, -91]	[-14.5, -12]		[11.5, 14]
	$MS_2(7)$	[-89.8, NA]	[-10.8, NA]		[0.2, NA]

Figure 5-8: The $\vartheta - \vartheta$ polarization $APS(\mathbf{\Omega}_R)$ at MS_2
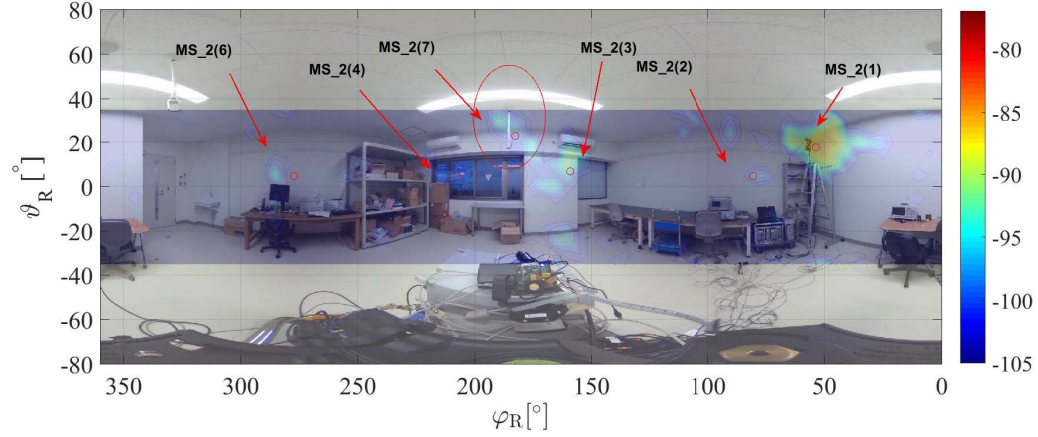
Figure 5-9: The $\varphi - \varphi$ polarization $APS(\mathbf{\Omega}_R)$ at MS_2

5.2.3 Major propagation mechanisms

The major propagation mechanism and the cluster gain for all the detected clusters are shown in Table 5.4. Unlike in outdoor environment where the first and the second reflection clusters were dominant, here the clusters due to scattering are comparable to the first order reflection. This can be expected due to the vicinity of the receivers to the scattering object. The diffracted components are on the other hand only comparable to second order specular reflections. In this measurement campaign only the LOS indoor case was considered. We have already seen from the outdoor case presented in the previous chapter that the diffracted components and clusters contributing to it become significant in the O-LOS or the N-LOS case. It must be noted that in case of

the scattering from the window blinds, we assumed the mechanism to be scattering even though ray tracing results showed reflected paths from that general direction when the window was modeled with metal or as a solid block and not glass.

The lower XPR seen in the LOS condition is due to the Conner reflection and back scattering from the wall in the vicinity of the transmitting antenna. This also explains the large spread seen in the $APS(\mathbf{\Omega}_R)$ plot corresponding to the LOS path. The overall angular spread for the LOS indoor positions are shown in Table5.5. The angular spread values are slightly larger than what was seen in the outdoor environment. Especially on the BS side when the MS is located centrally MS_2, the BS side spread is much larger. This also points to the corner reflections contributing to the spread even though the antennas are not aligned. Although we set the antennas to be at distances more than the far field distance, still being position near the vicinity affects the spread values.

5.2.4 Polarization specific angular dispersion in Indoor environment

Table 5.5: Double directional Angular spread under LOS condition in indoor environment

Polarization			LOS						
		MS_1				MS_2			
		BS side		MS Side		BS side		MS side	
		S_{φ_T}	S_{ϑ_T}	S_{φ_R}	S_{ϑ_R}	S_{φ_T}	S_{ϑ_T}	S_{φ_R}	S_{ϑ_R}
co pol	$\vartheta - \vartheta$	7.2	7.3	7.4	6.3	15.2	11.7	8	5.4
	$\varphi - \varphi$	7.4	8.2	5.1	4	16.4	12.9	6	5.1
cx pol	$\varphi - \vartheta$	10.5	11.2	15	11.7	5.4	8.41	3.8	7.9
	$\vartheta - \varphi$	7.3	9.5	3.3	11.3	13.5	12.9	4.5	3

5.3 Summary

From our high resolution, double directional channel measurement in indoor environment, we found that although there are very prominent specular like scattering

clusters due to first order reflections, there are also other equally prominent clusters due to scattering.

In terms of the delay spread, the spread values are much smaller than those found in the outdoor measurement. The maximum excess delay is comparable to the indoor room dimensions. Scattering by commonly found objects like the electrical extension chords or wires are not negligible and shows polarization filtering tendencies.

The antenna location near walls and scattering objects impact the angular spread values, with BS side spread values much on average larger than the MS side spread. The angular spread is relatively larger than the spread values seen in outdoor environment. This is to be expected due to more number of clusters being visible.

6 Summary and Conclusion

6.1 Summary

Millimeter wave is seen as one of the enablers of the next generation of wireless and cellular networks, thus attracting a lot of attention in the recent years. In this thesis the millimeter wave propagation in outdoor and indoor urban pico-cell environment were studied in the context of deployment in a heterogeneous wireless network.

To that end, a millimeter wave channel sounding system capable of full polarimetric 3-D double directional measurement is developed based on a prior 11GHz MIMO platform. Using this system in a 2×2 TDM based MIMO configuration, measurement campaign designed based on the probable usage scenarios in the future heterogeneous network were carried out.

A detailed analysis of the measured channel, focusing mainly on the direction and delay dispersion properties is presented. In order to understand more about the nature of the channel a multipath cluster based approach is adopted. Arguing that the multipaths within a cluster arise from interaction with a single object, the scattering object is pinpointed by utilizing the information from the synthesized APS, the cluster centroid and the panoramic image of the environment. Knowing the exact location of the scattering object a ray tracing assisted method is used to determine the major propagation mechanism that give rise to the clusters. The overall channel dispersion in both the delay and the angular domain is found to be highly dependent on the visibility of the of the clusters, thus instead of just the overall dispersion of the channel the intra-cluster dispersion characteristics for different propagation mechanisms under different polarization conditions are also detailed.

In terms of the propagation mechanism the specular reflections is dominant in the outdoor environment, however, in indoor environment where the scattering objects are much closer to the receiving antenna the multipath clusters due to scattering are comparable to the specular reflections. Diffraction is dominant in N-LOS or O-LOS conditions. Common household objects like thin electrical extension chords are seen to cause very high attenuation to parallel polarizations, acting like polarizer, therefore even small objects like this are not insignificant at millimeter wave frequencies. The scattering intensities of the objects in the environment are seen to be sensitive to polarization, with $-\vartheta$ polarization showing the highest gain, however the angular dispersion, both at the BS and the MS side does not show dependence on the polarization. The large number of dispersion parameters discussed in this study for different polarization and different LOS conditions should provide very useful inputs in designing the system, antenna and also algorithms such as beam-forming or beam-tracking.

6.2   Future Direction

Given the very long durations and specialized equipment required to perform these measurements, it is very essential to develop techniques for prediction that are reasonably accurate, fast and one that can take into account scattering from small surfaces. There are few approaches in recent years using point cloud data in conjunction with some scattering model. However another approach that is quite commonly used and well known among antenna and propagation community is the physical optics approximation. This together with the point cloud data is an interesting proposition for propagation prediction at higher frequencies. Such prediction study would help explain and make the results in this work more general.

Bibliography

[1] K. Sakaguchi and S. Sampei, "Potential of Multi-band Heterogeneous Cellular Networks and their Performance Boosting Technologies," in *Int. Work. Cloud Coop. Hetrogeneous Networks*, 2013.

[2] K. Wangchuk, K. Umeki, T. Iwata, P. Hanpinitsak, M. Kim, K. Saito, and J. Takada, "Double Directional Millimeter Wave Propagation Channel Measurement and Polarimetric Cluster Properties in Outdoor Urban Pico-cell Environment," *IEICE Trans. Commun.*, 2017.

[3] M. Kim, K. Wangchuk, S. Sasaki, K. Fukawa, and J. Takada, "Development of Low Cost Mm-Wave Radio Channel Sounder and Phase Noise Calibration Scheme," in *COST Action IC1004(EU), TD(15)12036*, 2015.

[4] J. Järveläinen, "Measurement-Based Millimeter-Wave Radio Channel Simulations and Modeling," Doctoral Dissertation, Aalto University, 2016.

[5] Ericsson, "Ericsson Mobility Report," Tech. Rep. [Online]. Available: https://www.ericsson.com/res/docs/2016/ericsson-mobility-report-2016.pdf

[6] Ericsson AB, "5G systems enabling industry and society transformation," Tech. Rep., 2015. [Online]. Available: https://www.ericsson.com/assets/local/publications/white-papers/wp-5g-systems.pdf

[7] J. Wells, "Faster Than Fiber: The Future of Multi-Gb/s Wireless," *IEEE Microw. Mag.*, no. May, pp. 104–112, 2009.

[8] T. S. Rappaport, R. Mayzus, Y. Azar, K. Wang, G. N. Wong, J. K. Schulz, M. Samimi, and F. Gutierrez, "Millimeter Wave Mobile Communications for 5G Cellular: It Will Work!" *IEEE Access*, vol. 1, pp. 335–349, 2013.

[9] S. Seidel and H. Arnold, "Propagation measurements at 28 GHz to investigate the performance of local multipoint distribution service (LMDS)," *Proc. GLOBECOM '95*, vol. 1, pp. 754–757, 1995.

[10] T. Pratt, C. W. Bostian, and J. E. J. E. Allnutt, *Satellite communications.* Wiley, 2003.

[11] T. S. Rappaport, J. N. Murdock, and F. Gutierrez, "State of the art in 60-GHz integrated circuits and systems for wireless communications," *Proc. IEEE*, vol. 99, no. 8, pp. 1390–1436, 2011.

[12] B. Langen, G. Lober, and W. Herzig, "Reflection and transmission behaviour of building materials at 60 GHz," *5th IEEE Int. Symp. Pers. Indoor Mob. Radio Commun. Wirel. Networks - Catch. Mob. Futur.*, pp. 505–509, 1994.

[13] C. R. Anderson, S. Member, and T. S. Rappaport, "In-Building Wideband Partition Loss Measurements," *IEEE Trans. Wirel. Commun.*, vol. 3, no. 3, pp. 922–928, 2004.

[14] R. J. Weiler, M. Peter, W. Keusgen, E. Calvanese-strinati, A. D. Domenico, I. Filippini, A. Capone, I. Siaud, A. Maltsev, T. Haustein, and K. Sakaguchi, "Enabling 5G Backhaul and Access with millimeter-waves," in *Eur. Conf. Networks Commun.*, 2014.

[15] Samsung Electronics, "February 2015 Dawn of the 5G Era Internet of Things 5G Service Vision," 2015.

[16] A. Sulyman, A. Nassar, M. Samimi, G. Maccartney, T. Rappaport, and A. Alsanie, "Radio propagation path loss models for 5G cellular networks in the 28 GHZ and 38 GHZ millimeter-wave bands," *IEEE Commun. Mag.*, vol. 52, no. 9, pp. 78–86, 2014.

[17] T. S. Rappaport, G. MacCartney, M. Samimi, and S. Sun, "Wideband Millimeter-Wave Propagation Measurements and Channel Models for Future Wireless Communication System Design," *IEEE Trans. Commun.*, vol. PP, no. 99, pp. 1–1, 2015. [Online]. Available: http://ieeexplore.ieee.org/lpdocs/epic03/wrapper.htm?arnumber=7109864

[18] A. I. Sulyman, A. Alwarafy, G. R. MacCartney, T. S. Rappaport, and A. Alsanie, "Directional Radio Propagation Path Loss Models for Millimeter-Wave Wireless Networks in the 28-, 60-, and 73-GHz Bands," *IEEE Trans. Wirel. Commun.*, vol. 15, no. 10, pp. 6939–6947, 2016.

[19] Y. Azar, G. N. Wong, K. Wang, R. Mayzus, J. K. Schulz, H. Zhao, F. Gutierrez, D. Hwang, and T. S. Rappaport, "28 GHz propagation measurements for outdoor cellular communications using steerable beam antennas in New York city," *IEEE Int. Conf. Commun.*, pp. 5143–5147, 2013.

[20] S. Hur, S. Baek, B. Kim, Y. Chang, A. Molisch, T. Rappaport, K. Haneda, and J. Park, "Proposal on Millimeter-Wave Channel Modeling for 5G Cellular System," *IEEE J. Sel. Top. Signal Process.*, vol. 10, no. 3, pp. 1–1, 2016. [Online]. Available: http://ieeexplore.ieee.org/lpdocs/epic03/wrapper.htm?arnumber=7400962

[21] G. R. Maccartney, M. K. Samimi, and T. S. Rappaport, "Exploiting directionality for millimeter-wave wireless system improvement," *IEEE Int. Conf. Commun.*, vol. 2015-Septe, pp. 2416–2422, 2015.

[22] G. R. Maccartney, J. Zhang, S. Nie, and T. S. Rappaport, "Path loss models for 5G millimeter wave propagation channels in urban microcells," *GLOBECOM - IEEE Glob. Telecommun. Conf.*, pp. 3948–3953, 2013.

[23] S. Hur, Y.-j. Cho, T. Kim, J. Park, A. F. Molisch, K. Haneda, and M. Peter, "Wideband Spatial Channel Model in an Urban Cellular Environments At 28 GHz," pp. 1–5.

[24] H. C. Nguyen, I. Rodriguez, T. B. Sorensen, L. L. Sanchez, I. Kovacs, and P. Mogensen, "An empirical study of urban macro propagation at 10, 18 and 28 GHz," *IEEE Veh. Technol. Conf.*, vol. 2016-July, pp. 1–5, 2016.

[25] V. Nurmela, A. Karttunen, A. Roivainen, L. Raschkowski, T. Imai, J. Jarvelainen, J. Medbo, J. Vihriala, J. Meinila, K. Haneda, V. Hovinen, J. Ylitalo, N. Omaki, K. Kusume, P. Kyosti, T. Jamsa, A. Hekkala, R. J. Weiler, and M. Peter, "METIS channel models," in *Tech. Rep. ICT-317669-METIS/D1.4, METIS*, 2015.

[26] T. S. Rappaport, E. Ben-Dor, J. N. Murdock, and Y. Qiao, "38 GHz and 60 GHz angle-dependent propagation for cellular & peer-to-peer wireless communications," *IEEE Int. Conf. Commun.*, pp. 4568–4573, 2012.

[27] T. S. Rappaport, F. Gutierrez, E. Ben-Dor, J. N. Murdock, Y. Qiao, and J. I. Tamir, "Broadband Millimeter-Wave Propagation Measurements and Models Using Adaptive-Beam Antennas for Outdoor Urban Cellular Communications," *IEEE Trans. Antennas Propag.*, vol. 61, no. 4, pp. 1850–1859, apr 2013. [Online]. Available: http://ieeexplore.ieee.org/lpdocs/epic03/wrapper.htm?arnumber=6387266

[28] T. S. Rappaport, E. Ben-Dor, J. N. Murdock, and Y. Qiao, "38 GHz and 60 GHz angle-dependent propagation for cellular & peer-to-peer wireless communications," in *2012 IEEE Int. Conf. Commun.* IEEE, jun 2012, pp. 4568–4573. [Online]. Available: http://ieeexplore.ieee.org/lpdocs/epic03/wrapper.htm?arnumber=6363891

[29] Y.-H. Y. Kim, K.-S. Yang, and S.-H. Kim, "Scattering characteristics of surface roughness in frequency and incident angle dependent at millimeter-wave," *1999 Asia Pacific Microw. Conf. APMC'99. Microwaves Enter 21st Century. Conf. Proc. (Cat. No.99TH8473)*, vol. 3, pp. 789–792, 1999.

[30] G. R. Maccartney and T. S. Rappaport, "73 GHz millimeter wave propagation measurements for outdoor urban mobile and backhaul communications in New York City," *2014 IEEE Int. Conf. Commun. ICC 2014*, no. June, pp. 4862–4867, 2014.

[31] V. Semkin, U. Virk, A. Karttunen, K. Haneda, and A. V. Räisänen, "E-band Propagation Channel Measurements in an Urban Street Canyon," *Antennas Propag. (EuCAP), 2015 9th Eur. Conf.*, pp. 1–4, 2015.

[32] M. Kyrö, V. M. Kolmonen, and P. Vainikainen, "Experimental propagation channel characterization of mm-wave radio links in urban scenarios," *IEEE Antennas Wirel. Propag. Lett.*, vol. 11, pp. 865–868, 2012.

[33] G. Lovnes, J. Reis, and R. Raekken, "Channel sounding measurements at 59 GHz in city streets," *5th IEEE Int. Symp. Pers. Indoor Mob. Radio Commun. Wirel. Networks - Catch. Mob. Futur.*, pp. 496–500, 1994.

[34] P. Smulders and L. Correia, "Characterisation of propagation in 60 GHz radio channels," *Electron. Commun. Eng. J.*, vol. 9, no. 2, p. 73, 1997.

[35] H. J. Thomas, R. S. Cole, and G. L. Siqueira, "An Experimental Study of the Propagation of 55 GHz Millimeter Waves in an Urban Mobile Radio Environment," *IEEE Trans. Veh. Technol.*, vol. 43, no. 1, pp. 140–146, 1994.

[36] E. Violette, R. Espeland, R. DeBolt, and F. Schwering, "Millimeter-wave propagation at street level in an urban environment," *IEEE Trans. Geosci. Remote Sens.*, vol. 26, no. 3, pp. 368–380, may 1988. [Online]. Available: http://ieeexplore.ieee.org/lpdocs/epic03/wrapper.htm?arnumber=3038

[37] E. Ben-Dor, T. S. Rappaport, and S. J. Lauffenburger, "Millimeter-Wave 60 GHz Outdoor and Vehicle AOA Propagation Measurements Using a Broadband Channel Sounder," in *2011 IEEE Glob. Telecommun. Conf. - GLOBECOM 2011.* IEEE, dec 2011, pp. 1–6.

[38] W. Keusgen, R. J. Weiler, M. Peter, M. Wisotzki, and B. Goktepe, "Propagation measurements and simulations for millimeter-wave mobile access in a busy urban environment," *Int. Conf. Infrared, Millimeter, Terahertz Waves, IRMMW-THz*, 2014.

[39] B. Goktepe, M. Peter, R. J. Weiler, and W. Keusgen, "The influence of street furniture and tree trunks in urban scenarios on ray tracing simulations in the millimeter wave band," *Eur. Microw. Week 2015 "Freedom Through Microwaves", EuMW 2015 - Conf. Proceedings; 2015 45th Eur. Microw. Conf. Proceedings, EuMC*, pp. 195–198, 2015.

[40] P. Smulders, "Statistical Characterization of 60-GHz Indoor Radio Channels," *IEEE Trans. Antennas Propag.*, vol. 57, no. 10, pp. 2820–2829, 2009.

[41] T. Zwick, T. Beukema, and Haewoon Nam, "Wideband channel sounder with measurements and model for the 60 GHz indoor radio channel," *IEEE Trans. Veh. Technol.*, vol. 54, no. 4, pp. 1266–1277, jul 2005.

[42] P. F. M. Smulders and A. G. Wagemans, "Frequency-domain measurement of the millimeter wave indoor radio channel," *IEEE Trans. Instrum. Meas.*, vol. 44, no. 6, pp. 1017–1022, 1995.

[43] P. Smulders, "BroadbandWireless LANs: A Feasibility Study," Ph.D. dissertation, Eindhoven: Technische Universiteit Eindhoven, 1995.

[44] Q. H. Spencer, B. D. Jeffs, M. A. Jensen, and L. L. Swindlehurst, "Modeling the statistical time and angle of arrival characteristics of an indoor multipath channel," *IEEE J. Sel. Areas Commun.*, vol. 18, no. 3, pp. 347–360, 2000.

[45] K. Sato, H. Sawada, Y. Shoji, and S. Kato, "Channel Model for Millimeter Wave WPAN," in *2007 IEEE 18th Int. Symp. Pers. Indoor Mob. Radio Commun.* IEEE, 2007, pp. 1–5.

[46] A. Maltsev, R. Maslennikov, A. Sevastyanov, A. Khoryaev, and A. Lomayev, "Experimental investigations of 60 GHz WLAN systems in office environment," *IEEE J. Sel. Areas Commun.*, vol. 27, no. 8, pp. 1488–1499, 2009.

[47] A. Maltsev, E. Perahia, R. Maslennikov, A. Sevastyanov, A. Lomayev, and A. Khoryaev, "Impact of polarization characteristics on 60-GHz indoor radio communication systems," *IEEE Antennas Wirel. Propag. Lett.*, vol. 9, pp. 413–416, 2010.

[48] A. Maltsev, R. Maslennikov, A. Lomayev, A. Sevastyanov, and A. Khoryaev, "Statistical channel model for 60 GHz WLAN systems in conference room environment," *Radioengineering*, vol. 20, no. 2, pp. 409–422, 2011.

[49] K. Haneda, J. Jarvelainen, A. Karttunen, M. Kyro, and J. Putkonen, "Indoor short-range radio propagation measurements at 60 and 70 GHz," *8th Eur. Conf. Antennas Propagation, EuCAP 2014*, no. EuCAP, pp. 634–638, 2014.

[50] J. Poutanen, J. Salmi, K. Haneda, V. M. Kolmonen, and P. Vainikainen, "Angular and shadowing characteristics of dense multipath components in indoor radio channels," *IEEE Trans. Antennas Propag.*, vol. 59, no. 1, pp. 245–253, 2011.

[51] K. Haneda, J. Järveläinen, A. Karttunen, M. Kyrö, and J. Putkonen, "A statistical spatio-temporal radio channel model for large indoor environments at 60 and 70 GHz," *IEEE Trans. Antennas Propag.*, vol. 63, no. 6, pp. 2694–2704, 2015.

[52] A. Karttunen, J. Jarvelainen, A. Khatun, and K. Haneda, "Radio propagation measurements and WINNER II parameterization for a shopping mall at 60 GHz," in *IEEE Veh. Technol. Conf.*, vol. 2015, 2015.

[53] G. R. MacCartney, T. S. Rappaport, S. Sun, and S. Deng, "Indoor office wideband millimeter-wave propagation measurements and channel models at 28 and 73 GHz for Ultra-Dense 5G Wireless Networks," *IEEE Access*, vol. 3, pp. 2388–2424, 2015.

[54] Anne-Marie Ulmer-Moll, "MiWEBA D1.1: Definition of Scenarios and Use Cases," Millimeter-Wave Evolution for Backhaul and Access, Tech. Rep. December, 2014. [Online]. Available: http://www.miweba.eu/data/MiWEBA{_}D1.1{_}v1.0.pdf

[55] W. L. Stutzman and G. A. Thiele, *Antenna theory and design.* Wiley, 2013.

[56] Robert J. Mailloux, *Phased Array Antenna Handbook*, 2nd ed. Artech House, 2004.

[57] Wonbin Hong, Kwang-Hyun Baek, Youngju Lee, Yoongeon Kim, and Seung-Tae Ko, "Study and prototyping of practically large-scale mmWave antenna systems for 5G cellular devices," *IEEE Commun. Mag.*, vol. 52, no. 9, pp. 63–69, sep 2014.

[58] C. A. Balanis, *Advanced engineering electromagnetics.* John Wiley & Sons, 2012.

[59] J. Lu, D. Steinbach, P. Cabrol, P. Pietraski, and R. V. Pragada, "Propagation Characterization of an Office Building in the 60 GHz Band," in *8th Eur. Conf. Antennas Propag. (EuCAP 2014)*, no. EuCAP, 2014, pp. 809–813.

[60] N. Moraitis and P. Constantinou, "Indoor Channel Measurements and Characterization at 60 GHz for Wireless Local Area Network Applications," *IEEE Trans. Antennas Propag.*, vol. 52, no. 12, pp. 3180–3189, dec 2004.

[61] A. F. Molisch, *Wireless communications.* Wiley, 2011.

[62] M. Steinbauer, A. F. Molisch, and E. Bonek, "The double-directional radio channel," *IEEE Antennas Propag. Mag.*, vol. 43, no. 4, pp. 51–63, 2001.

[63] K. Haneda, "Channel Models and Beamforming at Millimeter-Wave Frequency," *IEICE Trans. Commun. Spec. Sect. Recent Prog. Radio Propag.*, no. 5, pp. 755–772, 2015.

[64] B. Fleury, "First- and second-order characterization of direction dispersion and space selectivity in the radio channel," *IEEE Trans. Inf. Theory*, vol. 46, no. 6, pp. 2027–2044, 2000.

[65] NTT Docomo, "5G Radio Access: Requirements, Concept and Technologies," *NTT DOCOMO White Pap.*, no. July, pp. 1–13, 2014. [Online]. Available: https://www.nttdocomo.co.jp/english/binary/pdf/corporate/technology/whitepaper{_}5g/DOCOMO{_}5G{_}White{_}Paper.pdf

[66] China Mobile, "C-RAN: the road towards green RAN," Tech. Rep., 2011. [Online]. Available: http://labs.chinamobile.com/cran/wp-content/uploads/CRAN{_}white{_}paper{_}v2{_}5{_}EN.pdf.

[67] A. Maltsev, "MiWEBA D5.1: Channel Modeling and Characterization," MiWEBA, Tech. Rep. June, 2014.

[68] T. Zwick, T. J. Beukema, and H. Nam, "Wideband channel sounder with measurements and model for the 60 GHz indoor radio channel," *IEEE Trans. Veh. Technol.*, vol. 54, no. 4, pp. 1266–1277, 2005.

[69] X. Yin, C. Ling, and M.-D. Kim, "Experimental Multipath-Cluster Characteristics of 28-GHz Propagation Channel," *IEEE Access*, vol. 3, pp. 3138–3150, 2015. [Online]. Available: http://ieeexplore.ieee.org/document/7378822/

[70] A. Maltsev and A. Pudeyev, "Millimeter-Wave Evolution for Backhaul and Access, WP:5 Propagation, Antennas and Multi-Antenna Techniques," Tech. Rep. June, 2014.

[71] J. Jarvelainen, K. Haneda, M. Kyro, V.-M. Kolmonen, J. Takada, and H. Hagiwara, "60 GHz radio wave propagation prediction in a hospital environment using an accurate room structural model," in *2012 Loughbrgh. Antennas Propag. Conf.*, no. November, 2012, pp. 1–4.

[72] K. Haneda, S. Le, H. Nguyen, and J. Putkonen, "Estimating the Omni-Directional Pathloss From Directional Channel Sounding," in *Eur. Conf. antennas progation*, 2016.

[73] M. Kim, J. Takada, and Y. Konishi, "Novel Scalable MIMO Channel Sounding Technique and Measurement Accuracy Evaluation With Transceiver Impairments," *IEEE Trans. Instrum. Meas.*, vol. 61, no. 12, pp. 3185–3197, dec 2012.

[74] Y. Konishi, Y. Chang, M. Kim, and J. Takada, "Versatile Radio Channel Sounder for Double Directional and Multi-link MIMO Channel Measurements at 11 GHz," *IEICE Trans. Electron.*, vol. E97-C, no. 10, pp. 994–1004, 2014.

[75] "TD-SPP3000, Tokyo Electron Device Ltd." [Online]. Available: http://www.inrevium.jp/pm/image{_}signal/spp3000.html

[76] "Rubidium oscillator, Stanford Research Systems." [Online]. Available: http://www.thinksrs.com/products/FS725.htm

[77] Y. Konishi and J.-i. Takada, "Development of Versatile Channel Sounder for Multi-link MIMO Channel Characterization at 11 GHz," Doctoral Dissertation, Tokyo Institute of Technology, 2012.

[78] "60 GHz Waveguide Development System V60WGD02," pp. 2–5, 2010. [Online]. Available: http://www.admiral-microwaves.co.uk/pdf/vubiq/V60WGD02.pdf

[79] M. Kim, Y. Konishi, J. Takada, and B. Gao, "Automatic IQ Imbalance Compensation Technique for Quadrature Modulator by Single-Tone Testing," *IEICE Trans. Commun.*, vol. E95-B, no. 5, pp. 1864–1868, 2012.

[80] M. Kim, Y. Maruichi, and J.-i. Takada, "Parametric Method of Frequency-Dependent I/Q Imbalance Compensation for Wideband Quadrature Modulator," *IEEE Trans. Microw. Theory Tech.*, vol. 61, no. 1, pp. 270–280, jan 2013.

[81] M. Kim, Y. Konishi, S. Member, and Y. Chang, "Large Scale Parameters and Double-Directional Characterization of Indoor Wideband Radio Multipath Channels at 11 GHz," *IEEE Antennas Propag.*, vol. 62, no. 1, pp. 430–441, 2014.

[82] "CST, 3D Electromagnetic Simulation Software." [Online]. Available: https://www.cst.com/

[83] J. A. Högbom and J. A., "Aperture Synthesis with a Non-Regular Distribution of Interferometer Baselines," *Astron. Astrophys. Suppl. Vol. 15, p.417*, vol. 15, p. 417, 1974.

[84] N. Czink, P. Cera, J. Salo, E. Bonek, J.-p. Nuutinen, and J. Ylitalo, "A Framework for Automatic Clustering of Parametric MIMO Channel Data Including Path Powers," in *IEEE Veh. Technol. Conf.* IEEE, sep 2006, pp. 1–5.

[85] M. Steinbauer, H. Ozcelik, H. Hofstetter, C. F. Mecklenb Auker, and E. Bonek, "How to Quantify Multipath Separation *," no. 3, 2002.

[86] L. Materum, J.-i. Takada, I. Ida, and Y. Oishi, "Mobile Station Spatio-Temporal Multipath Clustering of an Estimated Wideband MIMO Double-Directional Channel of a Small Urban 4.5 GHz Macrocell," *EURASIP J. Wirel. Commun. Netw.*, vol. 2009, no. 1, p. 804021, 2009.

[87] P. Hanpinitsak, M. Kim, and J.-I. Takada, "Clustering of multipath components utilizing geometrical parameters for indoor double-directional propagation channel," *2014 Asia-Pacific Microw. Conf. APMC 2014*, vol. 2, no. 1, pp. 1055–1057, 2014.

[88] N. Czink, X. Yin, H. OZcelik, M. Herdin, E. Bonek, and B. Fleury, "Cluster Characteristics in a MIMO Indoor Propagation Environment," *IEEE Trans. Wirel. Commun.*, vol. 6, no. 4, pp. 1465–1475, apr 2007. [Online]. Available: http://ieeexplore.ieee.org/document/4155686/

[89] "Ricoh Theta S, 360 degree camera." [Online]. Available: https://theta360.com/en/

[90] "Pasternack, 24dBi Pyramid Horn Antenna." [Online]. Available: https://www.pasternack.com/images/ProductPDF/PE9881-24.pdf

[91] J. Poutanen, K. Haneda, J. Salmi, V.-m. Kolmonen, A. Richter, P. Almers, and P. Vainikainen, "Development of measurement-based ray tracer for multi-link double directional propagation parameters," in *EuCAP 2009. 3rd Eur. Conf. Antennas Propagation, 2009.*, 2009, pp. 2622–2626.

[92] "Sketchup 2015, 3D modelling software." [Online]. Available: http://www.sketchup.com/products/sketchup-pro

[93] "RapLab, 3D ray tracing simulator." [Online]. Available: http://network.kke.co.jp/products/raplab/

[94] M. Kim, K. Umeki, T. Iwata, K. Wangchuk, J. Takada, and S. Sasaki, "Identification of Propagation Mechanism of Mm-Wave Outdoor Link," in *Asian Work. Antennas Propagation(AWAP2016)*, 2016.

[95] K. Wangchuk, K. Umeki, T. Iwata, P. Hanpinitsak, and S. Members, "Polarimetric Millimeter Wave Propagation Channel Measurement and Cluster Properties in Outdoor Urban Pico-cell Environment," in *2016 IEEE 27th Int. Symp. Pers. Indoor Mob. Radio Commun.*, 2016.

Publication List

Journal

[1] K. Wangchuk, K. Umeki, T. Iwata, P. Hanpinitsak, M. Kim, K. Saito, and J. Takada, "Double Directional Millimeter Wave Propagation Channel Measurement and Polarimetric Cluster Properties in Outdoor Pico-cell Environment" IEICE Trans. Commun., Vol.E100-B,No.7,Jul. 2017

Invited Lectures

[2] K. Wangchuk, M. Kim, K. Umeki, T. Iwata, K. Saito, J. Takada, "Directional Characteristics of Millimeter Wave Propagation Channel in Outdoor Urban Picocell," IEICE Technical Report, IEICE-AP2015-149, IEICE-RCS2015-238, Nov. 2015

International Conferences

[3] K. Wangchuk, K. Umeki, T. Iwata, P. Hanpinitsak, Minseok Kim, K. Saito, J. Takada, "Double Directional Millimeter Wave Propagation Channel Measurement and Polarimetric Cluster Properties in Outdoor," in 2016 IEEE 27th International Symposium on Personal, Indoor and Mobile Radio Communications (pimrc), Sept. 2016.

[4] M. Kim, **K. Wangchuk**, S. Sasaki, K. Fukawa, and J. Takada, "Development of Low Cost Mm-Wave Radio Channel Sounder and Phase Noise Calibration Scheme,"

in COST Action IC1004(EU), TD(15)12036, Jan. 2015.

[5] K. Wangchuk, K. Saito, J. Takada, "Investigation of Clusters in Indoor Millimeter Wave Propagation," in 2015 The Asian-Oceania Top University League on Engineering (ATOULE) Student Conference, Nov. 2015.

Domestic Conferences and Workshops

[6] K. Wangchuk, M. Kim, and J. Takada, "Millimeter wave channel sounding for future heterogeneous network," Microwave Workshop and Exhibition (MWE2015) Nov. 25 - Dec. 27, 2015.

[7] K. Wangchuk, M. Kim, and J. Takada, "Measurement based Investigation of Clusters in Indoor Millimeter Wave Propagation Channel" IEICE Society Conference, BS-1-6, Sept. 2015.

[8] K. Wangchuk, M. Kim, and J. Takada, "mmWaveDouble Directional Channel Sounder and Directional Characteristics of Indoor Channel" URSI Commission F Japanese Committee meeting, 17 Apr. 2015 .

[9] K. Wangchuk, M. Kim, and J. Takada, "mmWave Channel Sounding for Future Heterogeneous Cellular Networks - System development and preliminary measurement analysis" IEICE Technical Report, SRW2014-52, Mar. 2015.

Awards

[10] Seiichi Tejima Overseas-Student Research Award, Tokyo Institute of Technology, 2016.